Science and Technology Facilities Council

SCARF Annual Report 2020–2021

P Pavelin (editor)

March 2023

Enquiries concerning this report should be addressed to:

RAL Library
STFC Rutherford Appleton Laboratory
Harwell Oxford
Didcot
OX11 0QX

Tel: +44(0)1235 445384
email: libraryral@stfc.ac.uk

Science and Technology Facilities Council reports are available online at:
https://epubs.stfc.ac.uk

Accessibility: a Microsoft Word version of this document (for use with assistive technology) may be available on request.

Neither the Council nor the Laboratory accept any responsibility for loss or damage arising from the use of information contained in any of their reports or in any communication about their tests or investigations.

SCARF Annual Report 2020-2021
Version: 1.0

Date: 15/01/2023

Edited by Phil Pavelin (philip.pavelin@stfc.ac.uk) 01235 445141
Content written by the respective authors

Date	Revision	Changes
05/07/22	0.1	Initial document outline
04/10/22	0.2	Updated stats and graphs
4/1/23	0.3	Proof reading and corrections
6/2/23	0.4	Ready for review
14/2/23	0.5	With corrections from review
23/2/23	1.0	Final version

Abstract

Annual Report on the Usage and Scientific Impact of the SCARF Service

Dissemination

This is a public document

1. SCARF SERVICE

SCARF is a High-Performance Cluster for STFC staff, Facilities (ISIS, DIAMOND, CLF) and their users and collaborators. The SCARF Service was started in 2004 and has been upgraded year-on-year and now represents a significant capital investment in High Performance Computing. Overall SCARF now has approximately 699 nodes providing 16156 CPU cores and 113TB memory, underpinned by 5.5PB of disk space (Details in Appendix A1 and A2).

This report covers the period from 9th December 2019 to 31st December 2021 (henceforth referred to as 2020-2021) and outlines the research that SCARF has enabled.

SCARF Usage by Department

Each time a researcher uses the SCARF service the CPU time used is recorded. Jobs submitted to SCARF used 225 million CPU Hours during 2020-21.
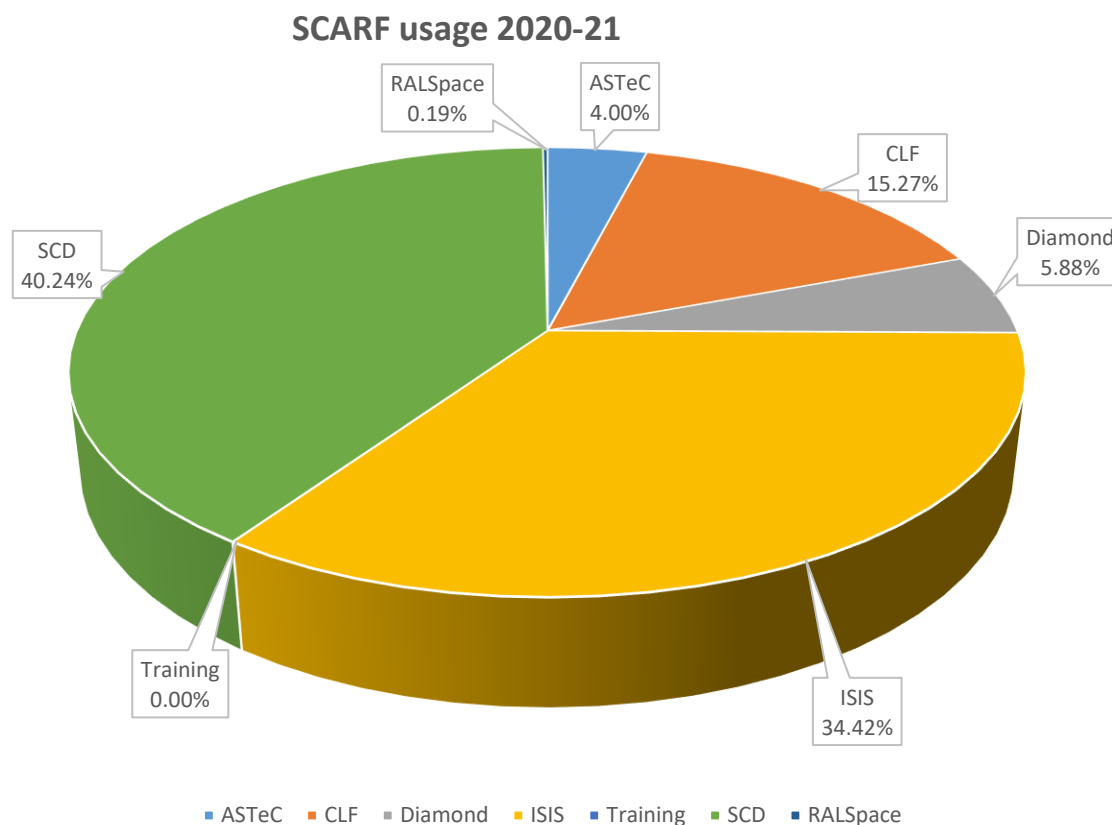
Figure 1: Pie chart showing percentage usage of SCARF, by department

It is clear from the usage chart that ISIS and Scientific Computing are by far the heaviest users of SCARF with CLF, still a significant consumer of resources, next. Diamond, whilst still a relatively small user of SCARF, has maintained a steady level of usage.
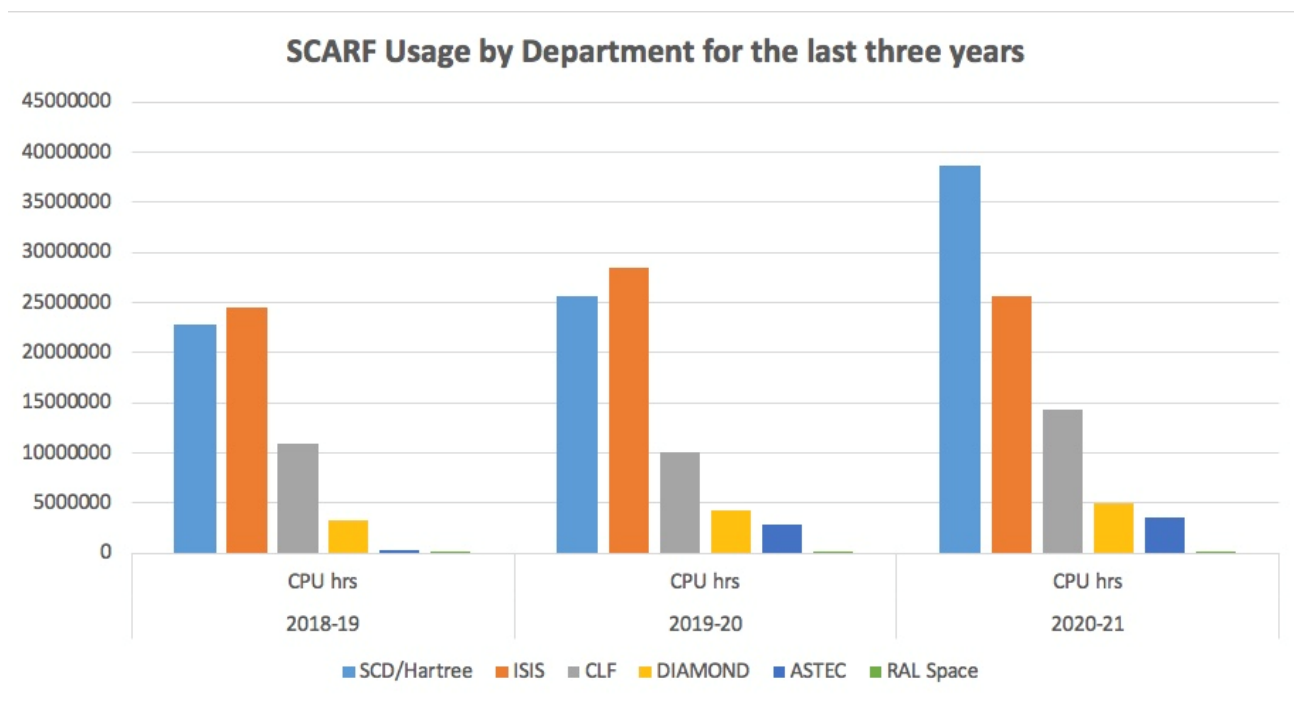
Figure 2: Graph showing SCARF usage by department, for the last three years

The table below shows the number of active users and their CPU usage for the last three years. There is no distinction made between STFC staff or external collaborators. We have included the Training accounts this year and while usage for this purpose is still small, it is an area of growth.

Department	2020-21			2019-20			2018-2019		
	Active Users	CPU hrs	%	Active Users	CPU hrs	%	Active Users	CPU hrs	%
SCD/Hartree	109	38553398	44.3	100	25556814	35.7	100	22709660	36.7
ISIS	70	25597653	29.4	71	28502729	39.8	73	24474255	39.6
CLF	44	14328529	16.5	49	10107710	14.1	53	10979295	17.8
DIAMOND	29	4937385	5.7	29	4262848	6	29	3294523	5.3
ASTEC	3	3623647	4.2	3	2889029	4	3	276944	0.4
RAL Space	1	19.2	0.1	1	214283	0.3	1	69460	0.1
Training	23	106.3	0		0		N/A	22828	0
CCFE	0	0	0	0	0	0	0	0	0
PPD	0	0	0	0	0	0	0	0	0
Totals	279	87040737.5	100	247	71533413	100	259	61826965	100

Figure 3: Table displaying detailed CPU usage from 2020-21 compared to 2019-20 and 2018-19

A significant amount of computational resource has been utilised on SCARF and Section 3 highlights some of the scientific achievements that have been made possible with it.

SCARF Availability

SCARF provided good availability throughout this period. From time to time, there were scheduled maintenance periods, but these were advertised well in advance and kept to a minimum.

There was a power outage on 22nd June 2020 due to a power issue in the server room which was outside of the control of the SCARF team.

SCARF Developments

Major SCARF Developments are listed below:

- Introduction of the SCARF21 hardware, this is 166 compute nodes each with a AMD 7502p 32 core processor, and 6 GPU nodes with dual AMD 7302p 16 core processors and 4 NVIDIA A100 40GB SXM cards
- Completion of migration from RHEL 6 to CentOS 7
- Introduction of the SCARF20 hardware and recompilation of software to work with AMD processors
- Introduction of new PANASAS storage with double the capacity of the existing
- Commissioned a 2PB, Infiniband-connected GPFS fast scratch volume
- New SCARF login nodes introduced. More powerful and connected to the Infiniband fabric.
- New application area, work areas, home areas and scratch areas
- New Samba server

Application Highlights

Application	Details
EPOCH v4.17	EPOCH is a plasma physics simulation code which uses the Particle in Cell (PIC) method.
FLUKA v2021.2	is a fully integrated particle physics MonteCarlo simulation package.
RMCProfile v6.7.7	Reverse Monte Carlo for crystalline and disordered materials
GROMACS v2021.3	GROMACS is a molecular dynamics package mainly designed for simulations of proteins, lipids, and nucleic acids.
VASP v5.4.4	The Vienna Ab initio Simulation Package, better known as VASP, is a package for performing ab initio quantum mechanical calculations using either Vanderbilt pseudopotentials, or the projector augmented wave method, and a plane wave basis set.
NWChem v7.0.2	NWChem is an ab initio computational chemistry software package which includes quantum chemical and molecular dynamics functionality.
QuantumESPRESSO v6.7	Quantum ESPRESSO is a suite for first-principles electronic-structure calculations and materials modelling.
Selected toolchains	FOSS (GCC, OpenMPI, OpenBLAS, ScaLAPACK, FFTW) 2018a, 2018b, 2019a, 2019b, 2020a, 2021a OPMPI (Intel compilers, OpenMPI) 2018b, 2019b, 2021a IOMKL (Intel compilers, OpenMPI, MKL) 2017b, 2018b, 2019b, 2021a GOMPIC (GCC, OpenMPI, CUDA) 2019a, 2019b

Future Developments

- We plan to migrate SCARF to Rocky Linux 9
- Access will be enabled via IRIS-IAM authentication
- A new web portal will be made available
- We are investigating the feasibility of allowing job submission to the SCD Cloud.

Help and Support

For any queries concerning the SCARF service, please email the SCARF Helpdesk
scarf@hpc-support.rl.ac.uk

2. PUBLICATIONS AND PRESENTATIONS

The publications and presentations for research that made use of SCARF are a way of measuring the impact that SCARF itself has.

Publications

A list of publications is given in Section 6.

Presentations

Scientists have presented their work at 20 international conferences (See Section 6). This helps to demonstrate that the science enabled by SCARF is world class.

3. SCIENCE HIGHLIGHTS

Shapespyer parallel workflows – a case study:
self-assembly and structure of surfactants
in aqueous solution

Andrey V. Brukhno[1], Michael Seaton[1], John Purton[1],
Tim Snow[2] and James Doutch[3]

[1]Computational Chemistry Group, SCD, STFC/UKRI, Sci-Tech Daresbury, UK
[2]Diamond Light Source, Harwell
[3]ISIS, STFC/UKRI

Email: Andrey.Brukhno@stfc.ac.uk

Shapespyer is a state-of-the-art Python toolkit supported by a set of batch (Bash) scripts implementing semi-automated high-throughput parallel workflows for preparation and subsequent equilibration of complex multicomponent molecular structures to seed computational studies of condensed soft matter systems. The systems of interest to the project's partners and users include self-assembling surfactant, lipid and lipoprotein aggregates comprising thousands of molecules and, hence, millions of atoms, thereby requiring serious HPC resources and computer time for proper equilibration and tedious post-simulation analyses, e.g. cluster size distribution (polydispersity) and cluster moments of inertia with respect to the internal principal axes.

In this pilot, testbed study we focus on self-assembly of surfactants and, in particular, the phase behaviour and the emerging structures in solutions of three surfactants that are ubiquitous in washing and healthcare consumer products: Sodium-Dodecyl-Sulphate (SDS), Cetyl-Trimethyl-Ammonium-Bromide (CTAB) and Sodium-Lauryl-Ether Sulphate (SLES). The goal is to study the process of micellisation and the emergent structure morphologies as a function of surfactant and salt concentrations, but also to assess the quality of the modern atomistic (CHARMM-36) and coarse-grain (DPD) surfactant models in reproducing the experimental data, such as small angle scattering diffraction patterns and structure factors available from other experiments.

In summary, there is indirect experimental evidence via viscosity measurements, supported by coarse-grain DPD simulations [1, 2], of gradual transformation from spherically symmetrical micelles through elongated worm-like tubes, as the ionic strength of the solution is raised over 1 M (salt concentration). As the salt content is further increased, star-like formations emerge, eventually resulting in a threaded network. Even though this picture seems to be supported by DPD studies, our large-scale simulations of the same surfactant systems carried out with atomistic detail reveal only moderate enlargement and elongation of micelles. However, as the surfactant concentration is raised, the micelles start grouping, resulting in transient larger clusters, which in experiment can be easily confused for large-scale aggregates, see the pictures for illustration.

References:
1. J. Chem. Theory Comput. 2018, 14, 2633-2643
2. Journal of Colloid and Interface Science 557 (2019) 34-44
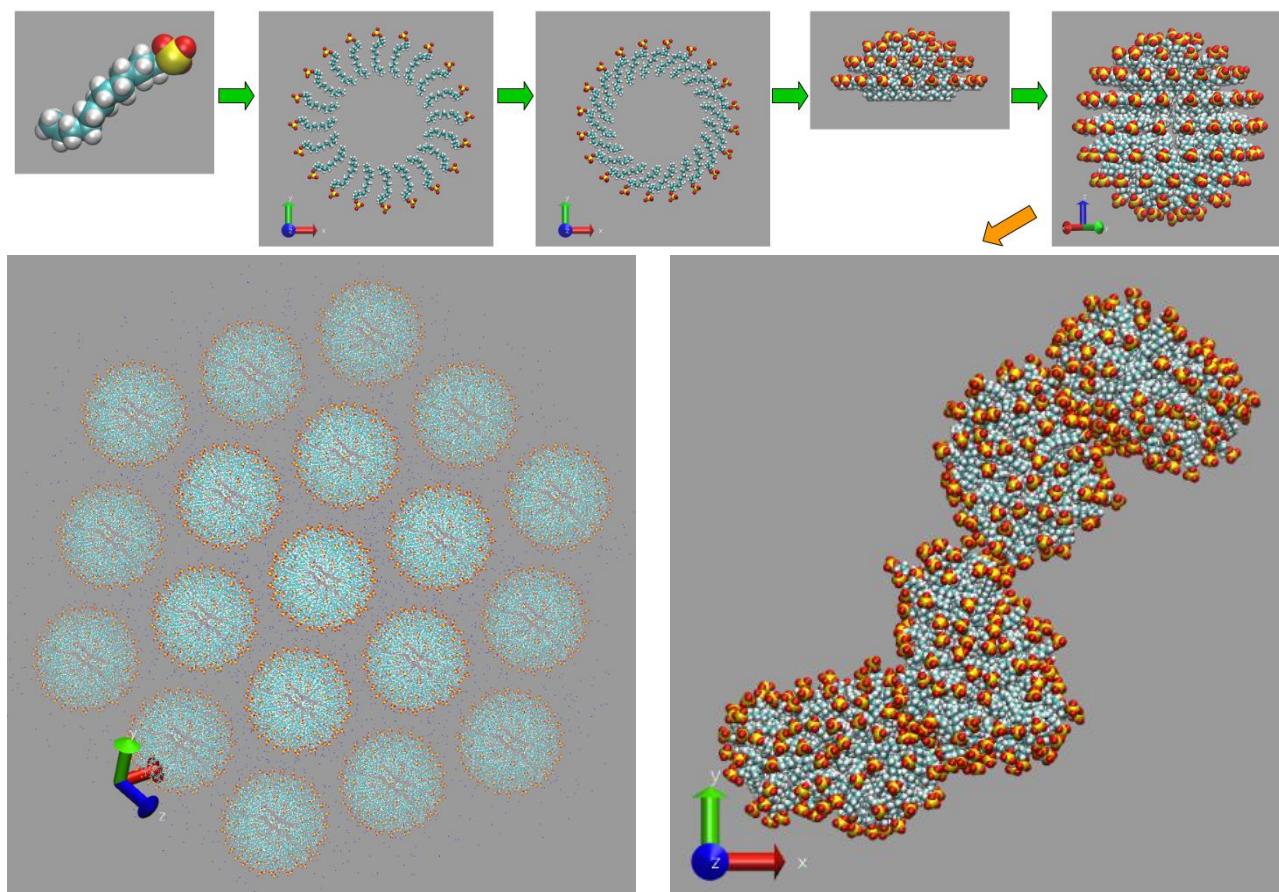
Figure 1. Upper row: illustration of the stages during generation of a spherical surfactant micelle with Shapespyer toolkit. Lower row: self-assembly of SDS surfactants (water and ionic species are omitted for clarity). Left panel: the initial configuration with micelles placed on a lattice. Right panel: four SDS micelles forming a larger aggregate.

1. Improving mechanical response in clay minerals using graphene

In this work we have used graphene to increase the mechanical response of montmorillonite clay to compression. We have used computational modelling to estimate elastic constants and bulk modulus of this hetero-structure.
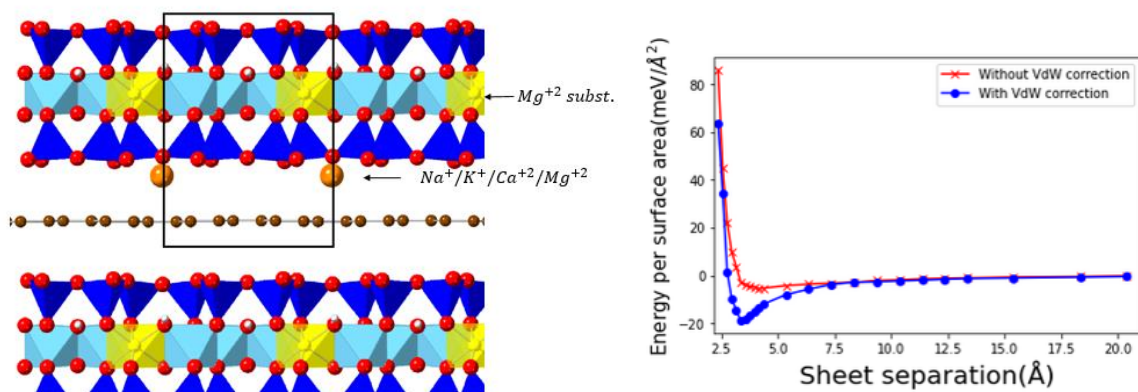
Figure 1. Left: Unit cell of the simulated structure. Right: Cleavage energy as a function of sheet separation

2. Incorporation of noble gasses in silicate minerals
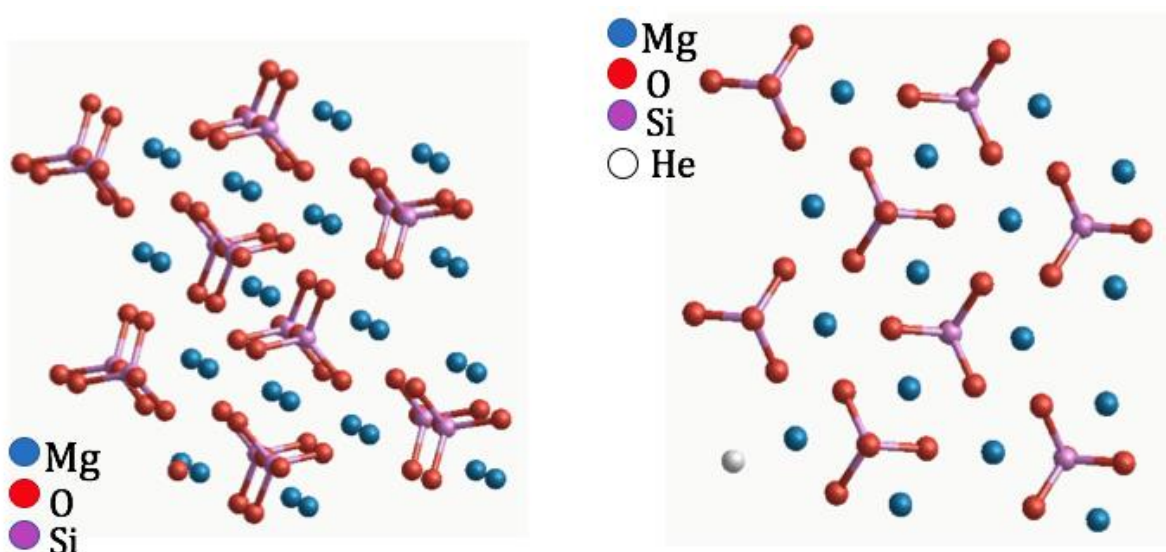
Figure 2. Forsterite (Mg2SiO4) structure with a H atom placed in a Mg site as a defect

Enhanced Spin−Orbit Coupling in Heavy Metals via Molecular Coupling

Satam Alotibi,[1] Bryan J. Hickey,[1] Gilberto Teobaldi,[2,3,4,5] Mannan Ali,[1] Joseph Barker,[1] Emiliano Poli,[2] David D. O'Regan,[6,7] Quentin Ramasse,[1,8] Gavin Burnell,[1] James Patchett,[9] Chiara Ciccarelli,[8] Mohammed Alyami,[1] Timothy Moorsom,[1] and Oscar Cespedes[1]

1.   *School of Physics and Astronomy, University of Leeds, Leeds, LS2 9JT, United Kingdom*
2.   *Scientific Computing Department, STFC-UKRI, Rutherford Appleton Laboratory, OX11 0QX Didcot, United Kingdom*
3.   *Beijing Computational Science Research Center, 100193 Beijing, China*
4.   *Stephenson Institute for Renewable Energy, Department of Chemistry, University of Liverpool, Liverpool, L69 3BX , United Kingdom*
5.   *School of Chemistry, University of Southampton, Southampton, SO17 1BJ, United Kingdom*
6.   *School of Physics, Trinity College Dublin, The University of Dublin, Dublin2, Ireland*
7.   *Centre of Research on Adaptive Nanostructures and Nanodevices (CRANN) and SFI Advances Material and Bio-Engineering Research Centre (AMBER), Dublin, Ireland*
8.   *SuperSTEM, SciTech Daresbury Science and Innovation Campus, Keckwick Lane, Daresbury, WA44AD, United Kingdom*
9.   *Cavendish Laboratory, University of Cambridge, JJ Thomson Avenue, Cambridge CB30HE, United Kingdom*

Spin-orbit coupling (**SOC**) is one of the most crucial interactions for magnetic devices and related technologies. It determines the magnetocrystalline anisotropy and is key to the propagation and electrical conversion of spin currents. The SOC also controls the efficiency of spin-charge conversion in the spin Hall, spin torque, and spin Seebeck effects. All of these processes are relevant for reducing the power consumption and energy dissipation of computing and electronic devices: an issue at the forefront of sustainable technology development.

In this work, we performed non-collinear Density Functional Theory (**DFT**) calculations using SCARF to support the interpretation of experimental measurements of the spin Hall magnetoresistance (**SHMR**) for composite Pt/C_{60} and Ta/C_{60} electrodes. The experimental measurements show that the SHMR for the composite electrodes are up to a factor of six higher than those for pristine Pt and Ta metals, resulting in a 20-60% increase in the spin Hall angle. At low fields of 1−30 mT, the presence of C_{60} increases the anisotropic magnetoresistance by up to 700%.

While our DFT simulations do not explicitly calculate the SHMR or transversal spin separation or accumulation, they do reveal that net magnetic moments can be acquired by Pt electrons due to the flowing of electrical currents. The magnitude of the calculated induced magnetic moments follows the experimental trends with respect to the thickness of the Pt films. Additional analysis based on non-collinear DFT band structures with explicit inclusion of the SOC reveal an inverse relationship between the C_{60}-enhanced magnetic moments and the thickness of the Pt slab.

One of the key-results derived from our DFT calculations is the quantification of the role of C_{60} in altering the SOC strength for Pt (E_{SOC}). Figure 1 shows the net and fractional changes of E_{SOC} for each layer of the Pt film when C_{60} is included in the calculations. The first two Pt layers directly beneath the C_{60} experience a marked decrease in E_{SOC}. Further from the interface with the C_{60}, there is a net enhancement of E_{SOC} in the third, fourth, and fifth Pt layers. These layers are further away from the C_{60} and closer to the interface with yttrium iron garnet (YIG, the magnetic insulator on which the heavy metal is deposited on experimentally). The percentage increase per Pt layer induced by C_{60} (compared to the same layer in the bare Pt film) is substantial and as large as 10−20% for the thinnest (1.1 nm) film modelled. Notably, such an enhancement persists deep within the Pt film, albeit reduced by a factor of roughly 2 in the bottommost (YIG-facing) layers of the thicker (2.5 and 3.9 nm) slabs. For these thicker films, the largest SOC enhancement is localised in layers progressively farther from the YIG interface. These results establish a correlation between the long-ranged, yet thickness-dependent, C_{60}-induced SOC enhancement and the measured enhancement of the SHMR in the composite Pt/C_{60} electrodes.

The enhancement of the effective SOC with molecular interfaces as demonstrated in this study can have applications, for example, in reducing the current densities in spin-transfer torque memories. Given its dependence on surface hybridisation and charge transfer, the SOC enhancement should be

controllable by application of an external voltage (electrical potential). This is a potentially significant development for dynamic external control of the SOC interactions, in contrast of static approaches (e.g. change in the device materials and composition) previously demonstrated.
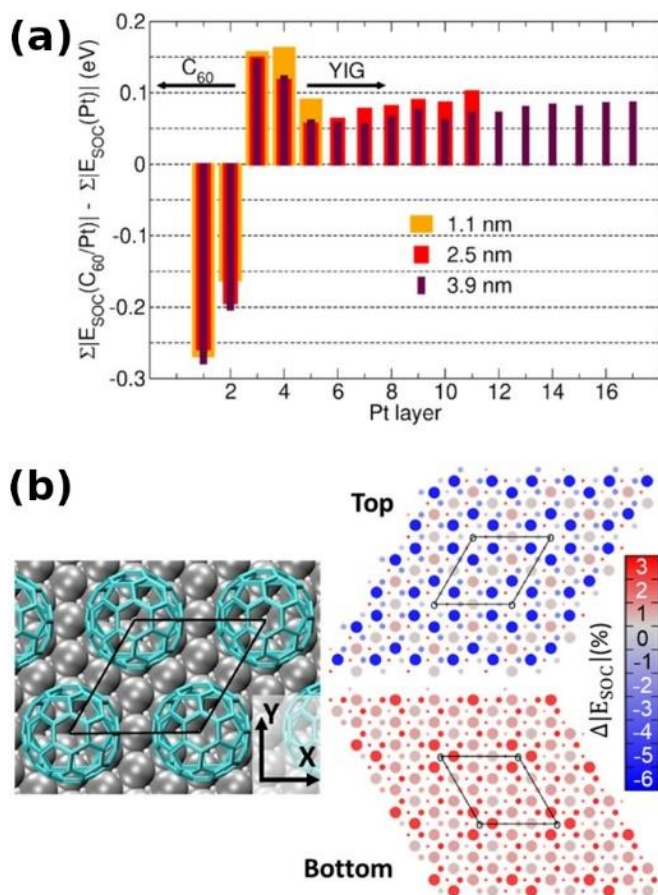
Figure 1*: (a) Pt layer-resolved, calculated C_{60}-induced changes in SOC strength (ΔE_{SOC}) as a function of the thickness of the Pt slab. Pt layer 1 is the closest to the C_{60} molecules. (b) Top view of the optimised C_{60}/Pt(111)-($2\sqrt{3} \times 2\sqrt{3}$)R30° interface DFT model. The C_{60} molecules are adsorbed on top of one Pt vacancy. The black polygon marks the in-plane periodicity of the system. Pt: silver and C: cyan. Right: Pt atom-resolved 2D maps of the C_{60}-induced changes in E_{SOC} ($\Delta|E_{SOC}|$) for the three topmost (top) and bottommost (bottom) Pt layers in C_{60}/Pt (1.1 nm)*

Observation of a molecular muonium polaron and its application to probing magnetic and electronic states

M. Rogers,[1] T. Prokscha,[2] G. Teobaldi,[3,4,5] Leandro Liborio,[3] S. Sturniolo,[3] E. Poli,[3] D. Jochym,[3] R. Stewart,[6] M. Flokstra,[6] S. Lee,[6] M. Ali,[1] B. J. Hickey,[1] T. Moorsom,[1] and O. Cespedes[1]

1. *School of Physics and Astronomy, University of Leeds, Leeds LS2 9JT, United Kingdom*
2. *Laboratory for Muon Spin Spectroscopy, Paul Scherrer Institute, 5232 Villigen, Switzerland*
3. *Scientific Computing Department, Science & Technology Facilities Council, Rutherford Appleton Laboratory, Didcot OX11 0QX. United Kingdom*
4. *Stephenson Institute for Renewable Energy, Department of Chemistry, University of Liverpool, Liverpool L69 3BX, United Kingdom*
5. *School of Chemistry, University of Southampton, Highfield, Southampton SO17 1BJ, United Kingdom*
6. *School of Physics and Astronomy, SUPA, University of St Andrews, St Andrews KY16 9SS, United Kingdom*

Direct spatial probing of interfacial spin ordering and electronic properties in composite materials is an ongoing experimental challenge, owing to the nm-scale localization and small magnitude of the effects. Mapping spin and charge distribution is an essential challenge for understanding and improvements in solid-state (thin-film) batteries and fullerene hybrid photovoltaics. Low-energy muon (μ^+) spin rotation (**LE-µSR**) is a powerful tool for characterizing interfacial and thin film spin phenomena for a multitude of systems. In this work, atomistic simulations were carried out to support the interpretation of LE-µSR measurement showing the presence of low frequency endohedral muonium polaron (a hydrogen-like bound state of the muon) in differently crystalline C_{60} films. Being coupled to the vibrational states of the C_{60} molecules in a wide range of temperatures, this muonium polaron can be used as highly sensitive probe to local electronic, vibrational and spin states.

Making use of the SCARF HPC infrastructure, we performed Density functional theory (**DFT**) simulations of muon and muonium species in differently crystalline C_{60} films both inside (*endohedral*) and outside (*exohedral*) the C_{60} molecules. Our calculations identify the endohedral muonium polaron (**ENDO$_f$**) state as the energetically favoured product of electron trapping at μ^+ sites in the presence of free-carriers in the conduction band of the C_{60} film, as produced by initial keV implantation of the μ^+ beam. The ENDO$_f$ polaronic state is characterized by a floating geometry for the μ^+ inside the C_{60}, slightly offset from the centre of mass of the molecule and at a distance of ~ 3 Å from the closest C-atom. This geometry presents no chemical bonding between the μ^+ particle and the C_{60}, leading to an electron spin-density localized around the μ^+.

Additional Born-Oppenheimer, DFT molecular dynamics (**BOMD**) simulations of μ^+ and muonium species confirmed the ENDO$_f$ state as the only system uncorrelated to the C_{60} rotational dynamics. This makes ENDO$_f$ the only species detectable in the experiments above 250 K, the temperature at which the free rotation of the C_{60} is activated. Path integral MD (**PIMD**) simulations of the ENDO$_f$ state at 50 and 300 K reiterate the localisation of this state around, but not exactly at, the centre of mass of the C_{60}. No quantum tunnelling through the C_{60} cage is observed during the (finite) timespan of the PIMD simulations. Additional modelling of the hyperfine coupling tensor elements and intrinsic muonium oscillation frequencies both in the presence and absence of external magnetic fields corroborates the assignment of the muonium polaronic state to the ENDO$_f$ species.

The ENDO$_f$ polaronic state responds to and can accordingly be used for detection of local magnetic fields as low as ~ 0.01 Gauss as well as charge transfer at a metallo-molecular interface. As C_{60} layers can be evaporated in situ on top of two-dimensional magnetic or ferroelectric materials, the discovery of this polaronic state opens up for depth-resolved, in situ studies of the magnetization, excess charge and dynamics of multi-layer materials for magnetic, solid-state batteries or photovoltaics applications.
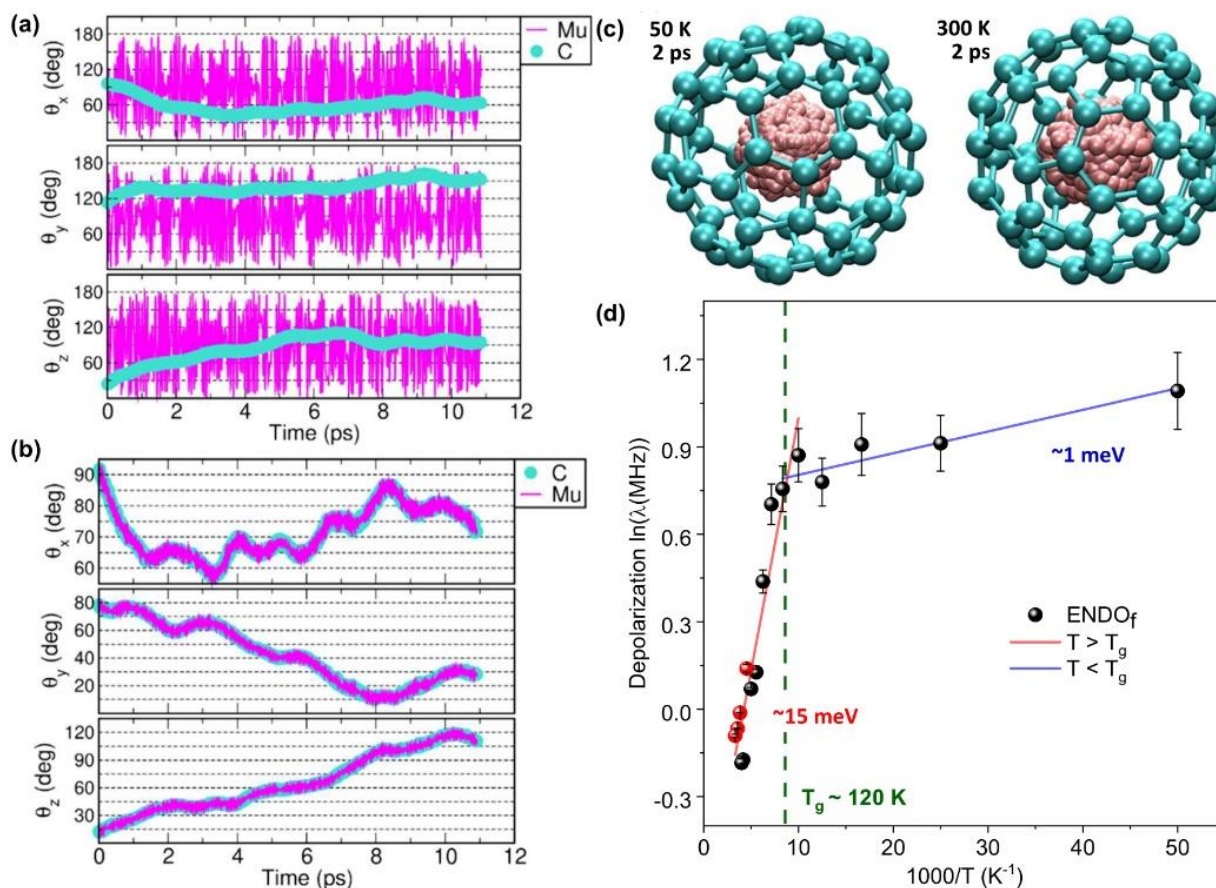
Figure1: *Muonium dynamics and activation energies. (**a**) Time evolution of the muon (Mu) and C-rotational dynamics in ENDO$_f$, as calculated by the angles between the instantaneous Mu (closest C-atom) radial distance from the C$_{60}$'s centre of mass and the x (θ_x), y (θ_y) and z (θ_z) axes. The C-trace reports the rotational evolution of the C-atom closest (~3 Å) to the Mu at the start of the BOMD trajectory. (**b**) As in (a), but for the EXO muonium state. The C-atom closest to the Mu does not change during the whole BOMD trajectory. Note that for the ENDO$_f$ state the dynamics of molecule and muonium are decoupled, whereas in the EXO state the muonium follows the molecular rotation. (**c**) PIMD distribution of the muon particle in the ENDO$_f$ at 50 and 300 K. For each of the 16 beads used in the simulations, 1000 frames (2 fs apart) were extracted from the production run and superimposed in the same image. The initial position of the C$_{60}$ is used to provide a better visualization of the quantum spread of the muonium inside the molecule. C: cyan, Mu: pink. (**d**) Temperature dependence of the depolarization rate associated with ENDO$_f$ state, showing the two thermal activation regimes above (red line fit) and below (blue) the glass transition Tg.*

π-anisotropy: A nanocarbon route to hard magnetism

Timothy Moorsom,[1] Shoug Alghamdi,[1,2] Sean Stansill,[1] Emiliano Poli,[3] Gilberto Teobaldi,[3,4,5,6] Marijan Beg,[7,8] Hans Fangohr,[7,8] Matt Rogers,[1] Zabeada Aslam,[1] Mannan Ali,[1] B. J. Hickey,[1] and Oscar Cespedes[1]

10. *School of Physics and Astronomy, University of Leeds, Leeds, LS2 9JT, United Kingdom*
11. *Department of Physics, Taibah University, Medina, 42331, Saudi Arabia*
12. *Scientific Computing Department, STFC-UKRI, Rutherford Appleton Laboratory, OX11 0QX Didcot, United Kingdom*
13. *Beijing Computational Science Research Center, 100193 Beijing, China*
14. *Stephenson Institute for Renewable Energy, Department of Chemistry, University of Liverpool, Liverpool, L69 3BX , United Kingdom*
15. *School of Chemistry, University of Southampton, Southampton, SO17 1BJ, United Kingdom*
16. *Faculty of Engineering and Physical Sciences, University of Southampton, Southampton, United Kingdom*
17. *European XFEL GmbH, Holzkoppel 4, 22869 Schenefeld, Germany*

Hard magnetic materials of high coercivity (the ability of a ferromagnetic material to withstand an external magnetic field without becoming demagnetized) are an essential component for renewable energy (wind and tidal power turbines), electric vehicles, and memory technologies. Most hard magnetic materials incorporate rare-earth metals such as neodymium and samarium, but concerns about the environmental impact and supply stability of these materials are prompting research into greener and more sustainable alternatives. In this work, we investigate a hybrid bilayer of cobalt (Co), a light transition metal, and the nanocarbon molecule C_{60}. The hybrid bilayer exhibits significantly enhanced coercivity with minimal reduction in magnetization with respect to the pristine Co substrate. Our DFT simulations, performed using SCARF HPC facilities, show that, on the (111) plane of thin films of Co in face cubic centred structure, the C_{60} preferentially adsorbs in a geometry with the edge between the C_{60} hexagonal and pentagonal (HP) carbon rings exposed to the Co-surface, leading to a breaking of the electronic symmetry for the underlying Co atoms. This in turn brings about a symmetry dependent interfacial spin polarization and additional magnetic anisotropy for the composite bilayer as experimentally measured by Prof Cespedes' group at the University of Leeds. If, however, the C_{60} molecules rotates exposing to the Co surface the edge between two of its hexagonal carbon rings (HH), the additional interfacial spin-polarization and magnetic anisotropy are cancelled. The effect is rationalised in terms of asymmetric electronic re-hybridisation between the *p* electrons of the C_{60} molecule and the *d* electrons of the Co film.

DFT simulations also indicate that, in spite the substantial adsorption energy of the C_{60} molecule on the Co surface (over 6 eV per molecule), the rotational energy barrier for interconversion of the HP and HH geometries is relatively low (0.25 eV). This corroborates the disappearance of the system's high coercivity at temperatures sufficiently high to activate the rotation of the C_{60} molecules on the Co surface, leading to interconversion of the HP geometry into the HH and the ensuing cancellation of the additional interface spin-polarisation and magnetic anisotropy.

The present work outlines a new form of magnetic anisotropy, arising from asymmetric magnetoelectric coupling in the metal-molecule interface. Since this phenomenon arises from π-d hybrid orbitals, we propose calling it *π-anisotropy*. Further computational and experimental research is ongoing towards protection of such π-anisotropy and of the ensuing increase in magnetic coercivity at room temperature, which is needed for practical development of more sustainable, rare-earth metal free, hard magnetism materials.
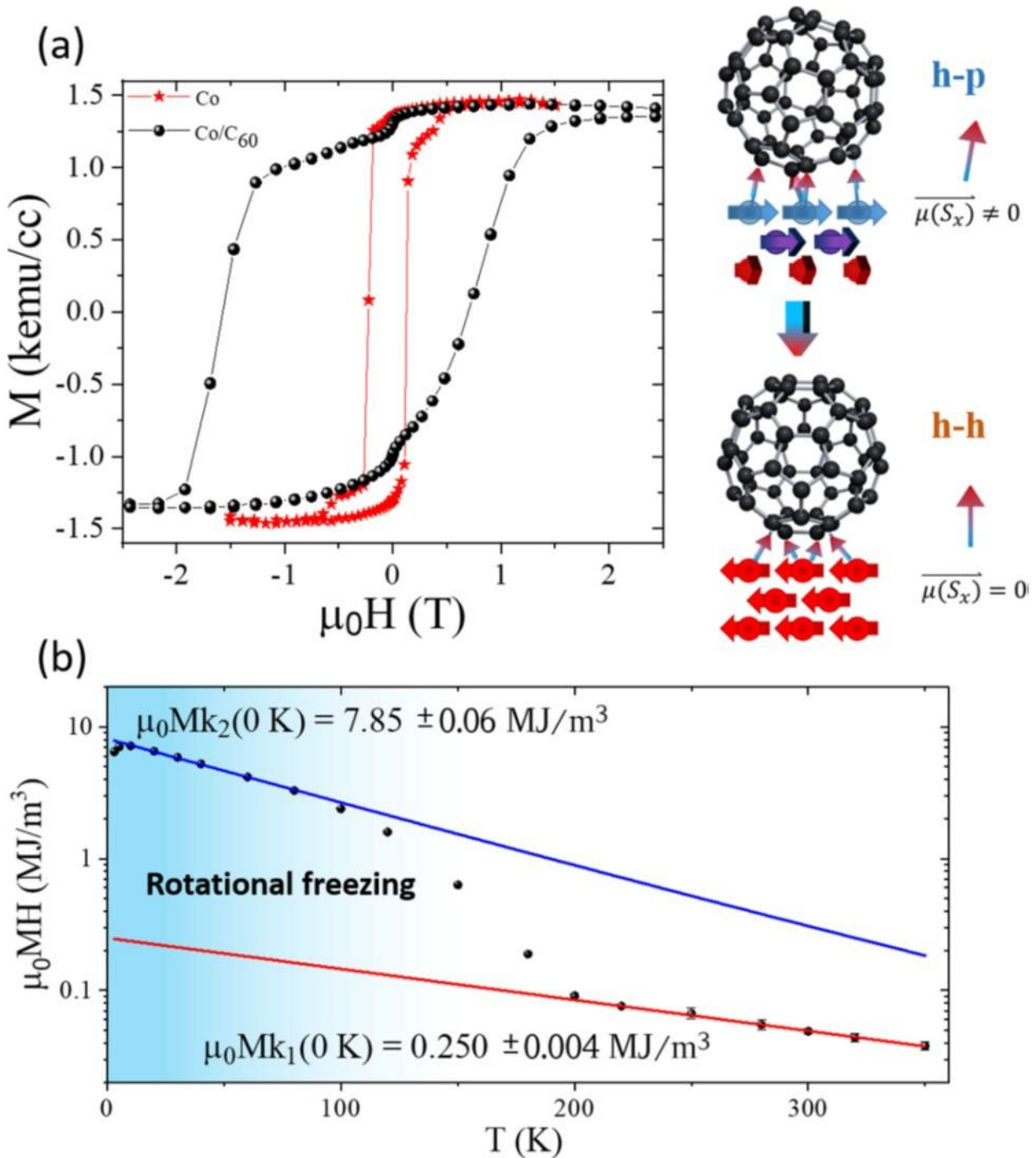
Figure. 1. *(a) MH curves for two identical bilayer films of Ta(4 nm)/Co(3 nm), cooled to 5 K in a 2 T applied field. The red curve (stars) is an uncapped film while the black curve (circles) is capped with a 35-nm film of C_{60}. The increase in the maximum energy product with the addition of C_{60} is 520%. The right-hand images show the computed orientation of the C_{60} molecule on the Co surface before demagnetization (top) and after (bottom). (b) The energy product for a Co/C_{60} film as a function of temperature. There are two distinct regimes above and below the rotational transition of C_{60} at 100 K. The red and blue fits are for the temperature dependent pinning factor as described in the temperature-dependent Jiles-Atherton model.*

Combined role of biaxial strain and nonstoichiometry for the electronic, magnetic, and redox properties of lithiated metal-oxide films: the LiMn₂O₄ case

Ivan Scivetti[1,3] and Gilberto Teobaldi[2,3,4]

1. Scientific Computing Department, STFC, Daresbury Laboratory, UK
2. Scientific Computing Department, STFC, Rutherford Appleton Laboratory, UK
3. Department of Chemistry, University of Liverpool, UK
4. School of Chemistry, University of Southampton, UK

Current commercial technologies for magnetic information storage and processing are based on compounds containing rare-earth metals, which are rare and expensive. The very low resilience to structural defects and chemical contamination of devices for information storage and electronic processing adds additional manufacturing challenges and costs to these technologies. In addition, rare metals present problems in terms of very harsh and unsustainable chemical processes needed for their extraction and purification, as well as geopolitical issues in terms of their mining, resourcing and distribution. Alternatives based on cheaper and environmentally more benign elements (such as light transition metals) would therefore present diversified benefits.

Lattice strain can be used to tune the electronic properties of materials and thin films, minimizing the risk of phase transformations and detrimental effects on structural integrity and functionality [1]. In recent years, film growth has benefited experimental research in surface chemistry and spintronics by enabling controlled manufacturing of relatively flat ultrathin films with the desired composition, crystallographic phase, and orientation. For such films, lattice strain can be induced by misfit at the interface with the supporting substrate. In spite of these advances, the interplay between lattice strain and chemical composition in metal-oxide surfaces for emerging electronic and magnetic properties has remained overlooked. To gain fundamental understanding of such interplay, we used SCARF HPC facilities to perform quantum mechanical simulations and study the electronic and magnetic structure of various model thin-films of LiMn₂O₄ (LMO), an archetypal metal oxide for battery applications. An example of such models is displayed in Fig. X1. We have considered over 30 different surface models for the low-energy facets of the crystal.
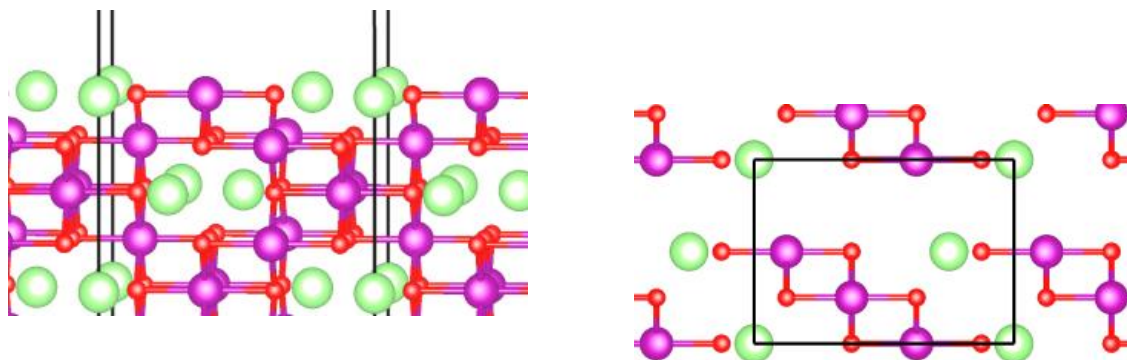
Figure X1. *Side and top view of a Li-terminated surface model for the (110) facet of LiMn₂O₄. Only the two outermost layers are displayed in the top views. The simulated in plane periodicity is indicated by the area inside the box. Mn: purple, O: red, Li: green.*

Calculations suggest that selected ferromagnetic surfaces with different chemical composition turn out to be half-metallic (i.e. metallic only for electrons of a given spin angular momentum) with a strong sensitivity on the applied strain for the band-gap and conduction properties of the minority-spin electrons (i.e. the electrons with an opposite spin angular momentum). These results are graphically summarised in Fig. X2. Compressive ($\varepsilon < 0$) and tensile ($\varepsilon > 0$) strain generally decreases and increases the minority spin band-gaps, respectively. Computed values are always larger than 1.4 eV, thus demonstrating a rather strong resilience of the half-metallic states to compositional changes [1].
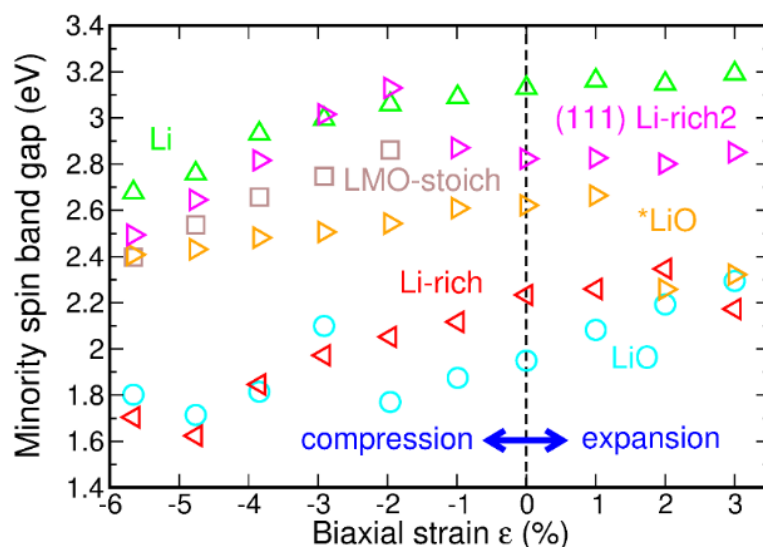
Figure X2. Calculated minority-spin band-gap for the selected half-metallic terminations of LiMn₂O₄ as a function of lattice strain (ε).

This response endows $LiMn_2O_4$ films with the capability of spin-selective electron transport, which is essential for the development of low-power, energy efficient information processing devices free of heat-dissipation, as inevitably present in commercial electronic devices based on spin-independent electron currents. The novel computational insights open up and inform new research avenues for development of more sustainable and energy-efficient solutions for information storage and processing.

[1] **Combined Role of Biaxial Strain and Nonstoichiometry for the Electronic, Magnetic, and Redox Properties of Lithiated Metal-Oxide Films: The LiMn2O4 Case. I. Scivetti, G Teobaldi. ACS Applied Materials & Interfaces 13 (45), 54610-54619 (2021).** https://doi.org/10.1021/acsami.1c18326

Quantitative resolution of complex stoichiometric changes during electrochemical cycling by Density Functional Theory assisted, Electrochemical Quartz Crystal Microbalance

Tzu-Ho Wu[1,2,3], Ivan Scivetti[2,4,5], Jia-Cing Chen[1], Jeng-An Wang[1], Gilberto Teobaldi[2,5,6], Chi-Chang Hu[1], and Laurence J. Hardwick[2]

1. Department of Chemical Engineering, National Tsing Hua University, Taiwan
2. Department of Chemistry, University of Liverpool, UK
3. Department of Chemical & Materials Engineering, National University of Science and Technology, Taiwan
4. Scientific Computing Department, STFC, Daresbury Laboratory, UK
5. Scientific Computing Department, STFC, Rutherford Appleton Laboratory, UK
6. Beijing Computational Science Research Center, China

Reversible ion-intercalation is one of the fundamental processes for electrochemical energy storage and conversion. In electrolyte ion batteries, this process involves the exchange of ions between the electrolyte and the host structure induced by charge/discharge voltage cycles. Repeated cycling eventually leads to battery degradation and loss of reversibility. This degradation occurs at different rates depending on the electrolytic ion species and the material under consideration. Unravelling the reasons behind degradation is key to the development of high performing, safer and sustainable electro-active materials.
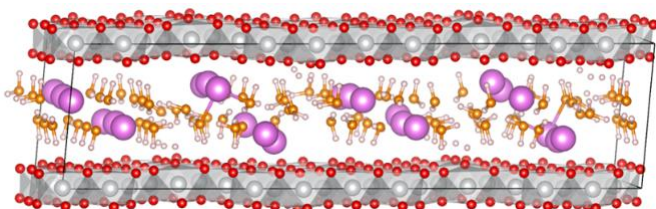
Figure X1. Example of a model structure for $H_zM_y(H_2O)_{1+x}(NiO_2)$ following ion-intercalation. M corresponds Na^+ in this case. Ni: grey, O in NiO_2: red, H: pink, O in H_2O: orange, Na: magenta. H-bonds are not displayed for the purpose of clarity.

A typical electro-active material is nickel hydroxide –$Ni(OH)_2$ comprising a layered structure with intercalated water and ions, as schematically shown in the model of Fig. X1. The general stoichiometric formula for this material is $H_zM_y(H_2O)_{1+x}(NiO_2)$, where M is the intercalated ion (Li^+, Na^+ or K^+). Intercalated water is crucial to provide structural stability for the material. A possible redox couple is the electrochemical cycling between the α-phase (with minimum amount of M) and the γ-phase (with intercalated M), as shown in Fig. X2a.
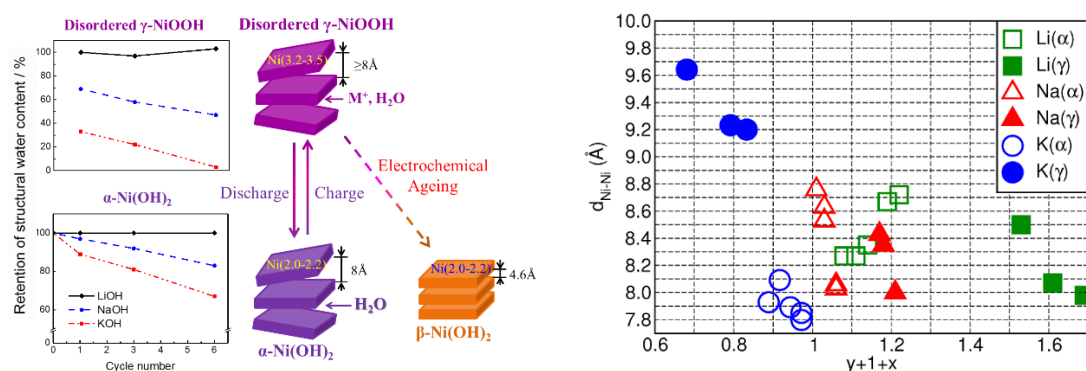
Figure X2. a) Redox couple between the α and γ phases of $Ni(OH)_2$. The retention of structural water is reported as a function of the cycle. Degradation for this material is manifested by the formation of the β-phase. b) Cation-resolved analysis of the computed Ni-Ni interlayer distance (d_{Ni-Ni}, Å) as a function of the cumulative water (x) and cation (y) content (y+1+x) for the energy-favoured optimised models of the charged (γ) and discharged (α) states, after electrochemical cycling.

Experimental changes in mass and charge associated with ion-intercalation were obtained by Electrochemical Quartz Crystal Microbalance (EQCM) [1]. The corresponding results indicate that when the samples are cycled in electrolytes containing Li^+ the electrode material shows less degradation than when cycled in Na^+ and K^+ containing electrolytes. For this material, degradation is manifested by the formation of the β-phase (Fig. X2a).

To investigate this degradation, we have developed a novel methodology that generates atomistic models of the intercalated structures compatible with EQCM data [1]. Using SCARF HPC facilities, we performed quantum simulations with Density Functional Theory (DFT). We find that computed average distances between NiO_2 layers (d_{Ni-Ni}) generally increase when the material changes from the α to the γ phase, and this increment is the largest for K^+ (see Fig. X2b). In addition, structural water in the material is almost completely removed upon the intercalation of K^+. Such a removal is reduced when intercalating Na^+ (Fig. X2a). This suggests that during the removal of K^+ or Na^+ (on discharge), if water molecules are not able to re-enter into the host material fast enough, the structure will be likely to collapse, leading to the formation of the β-phase and the electro-chemical degradation of the material. Conversely, since the amount of structural water remains practically unchanged when Li^+ is intercalated, the material takes much longer to degrade and exhibits a much better electrochemical performance.

[1] Quantitative Resolution of Complex Stoichiometric Changes During Electrochemical Cycling by Density Functional Theory Assisted, Electrochemical Quartz Crystal Microbalance. T-H. Wu; I. Scivetti; J-C. Chen; J-A. Wang; G. Teobaldi, C-C Hu; L.J. Hardwick. *ACS Appl. Energy Mater*. **3, 4, 3347–3357 (2020).**
https://doi.org/10.1021/acsaem.9b02386
Notes:
This work has been presented in the EMRS 2021 Fall meeting. Ivan Scivetti pre-recorded a video that was played in slot H.10.4 of the conference. See the following link:
https://www.youtube.com/watch?v=dogqL5DH5nk&list=PLFEB3YHuxu13XIcvx9Klld-a3LO3B0UWp

We also presented a posted in the "Next Generation Nanoelectrochemistry Faraday Discussion" (https://www.rsc.org/events/detail/43016/next-generation-nanoelectrochemistry-faraday-discussion)**.**

Accelerating Atomisitic Simulations With Machine Learning

K. Butler
Scientific Computing, STFC

Johannes Allotey – a PhD student based at the University of Bristol on the AIMLAC CDT on placement with the SciML group developed a new approach for providing confidence measures on the results of deep learning models for materials science. In recent years deep learning methods, notable graph neural networks (GNNs), have received a lot of attention in the materials science community. The reason that GNNs are gaining so much interest is that they can be trained to predict complex materials properties, such as formation energies, optical properties and mechanical strength, with comparable accuracy to quantum mechanics but in a fraction of the time and at a fraction of the computational cost. This kind of GNN based surrogate model is particularly appealing for materials design, where high-throughput screening on a computer is used to identify promising lead compounds for experiments.

However, a recurring question with GNNs and many deep learning approaches is: how much can we trust each prediction? Deep learning models have been shown to often be susceptible to so-called adversarial noise, where small, imperceptible changes to the input drastically change the output prediction of the model. The work in the SciML group looked for a way to develop GNNs that provide both a prediction and a measure of certainty/uncertainty on that prediction. By combining GNNs with another approach called Gaussian Processes (GPs) Johannes was able to build a model that provides accurate predictions as well as calibrated uncertainty measures.

The work was largely performed training the models on the SCARF and PEARL machines at SCD, where access to GPUs was critical for efficient training of the GNNs. The approach developed also allows for GNNs to be used in a so-called 'Active Learning' (AL) process, where the ML model can identify the most useful next experiment that can be performed to obtain new labelled data to train the model. The GNN-GP with AL has been shown to be more than twice as efficient as randomly choosing the next experiment, meaning that the model can learn much more efficiently and with less data.

Publications
J Allotey, KT Butler, J Thiyagalingam *The Journal of Chemical Physics* 155 (17), 174116, **2021**

Presentations
KT Butler – ACS Fall (Invited) 2021
KT Butler – MRS Fall (Invited) 2021
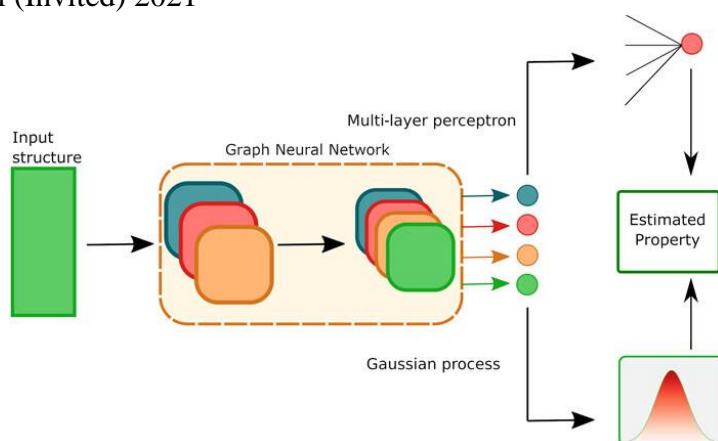
Machine learning for understanding neutron scattering

K. Butler
Scientific Computing, STFC

Machine learning (ML) and quantum mechanics have been combined by a team from ISIS Neutron and Muon Source and SciML to develop a new method that can analyse neutron scattering experiments and understand the magnetic structure of materials. Inelastic neutron scattering (INS) is a powerful technique that allows scientists to probe the atomic level structure of solids, it also reveals important information about how magnetic spins are arranged across individual atomic sites in the system. This level of understanding is critical for developing a range of exotic new technologies, such as quantum computers and high temperature superconductors.

Typically an INS experiment is analysed by careful, meticulous examination of the experimental results by a trained physicist. The process involves taking many samples from the experimental data and comparing these samples to simulations based on quantum mechanics. This procedure is both computationally and intellectually highly demanding and analysis of a single dataset can often take years to complete properly.

Now the team at SciML have developed a ML approach that can learn from simulated data and make predictions on the experimental data in a fraction of the time. It was also important for the scientists at ISIS that the methods are able to make statements about why the ML model gives the result that it does, so explainable ML was used to analyse the data. The results were very exciting, with the ML model identifying the same small regions of the INS data and correctly predicting the same magnetic structure of the materials tested as the scientists from ISIS had published some years before. While the analysis of the original data took more than two years, the entire process for training and running the ML model takes less than a week.

The success of the ML model was highly dependent on access to SCARF resources. First to develop the training dataset, quantum mechanics simulations were run in parallel on the SCARF nodes. Testing and developing of the ML models was then split between SCARF and PEARL machines both using GPUs to efficiently run the neural networks.

Publications
KT Butler, MD Le, J Thiyagalingam, TG Perring *Journal of Physics: Condensed Matter* 33 (19), 194006, **2021**

Presentations
KT Butler - Innovative Inelastic Neutron Scattering (Invited) 2021
KT Butler – AI4SD Conferences (Invited) 2022
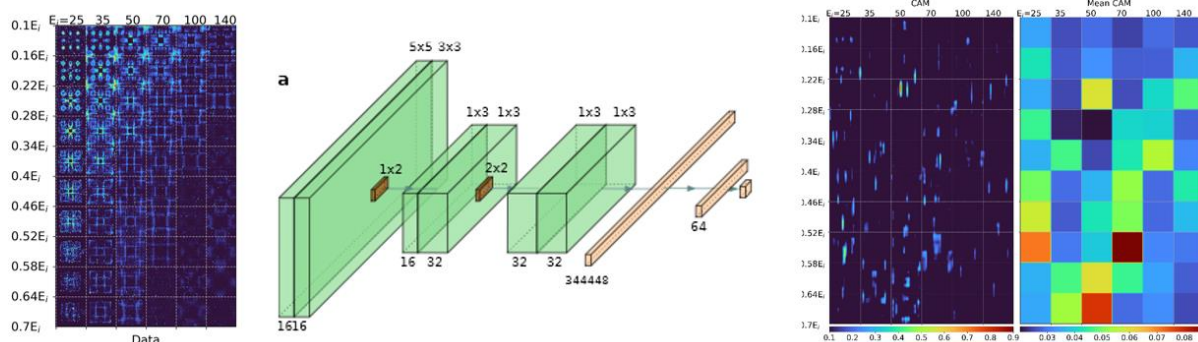
Computational prediction of muon stopping sites: a novel take on the unperturbed electrostatic potential method

S. Sturniolo[1], L. Liborio[1]

1 *Theoretical and Computational Physics Group, Scientific Computing Department, RAL, STFC, UK*

Finding the stopping site of the muon in a muon-spin relaxation experiment is one of the main problems of muon spectroscopy, and computational techniques that make use of quantum chemistry simulations can be of great help when looking for this stopping site. Hence, in this work, we presented a software implementation of the Unperturbed Electrostatic Potential (UEP) Method: an approach used for finding the muon stopping site in crystalline materials. The UEP method requires only one Density Functional Theory calculation, necessary to compute the electronic density. This, in turn, is used to calculate the minima of the crystalline material's electrostatic potential and the estimates of the muon stopping site. One of the main UEP's assumptions is that the muon stopping site will be one of the crystalline material's electrostatic potential minima. In this regard, we also propose some symmetry-based considerations about the properties of this crystalline material's electrostatic potential, in particular, which sites are more likely to be its minima and why the unperturbed approximation may be sufficiently robust for them. We introduce the Python software package `pymuon-suite` and the various utilities it provides to facilitate these calculations, and finally, we demonstrate the effectiveness of the method with some chosen example systems.
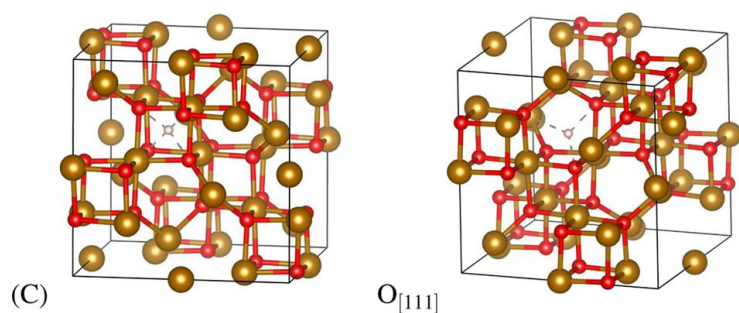
Predicted stopping sites in Fe_3O_4 are (a) located within a planar region that is perpendicular to the $\langle 111 \rangle$ direction and (b) situated within $\approx$1.5 Å of one of the oxygen atoms defining the planar region. The figure shows the $O_{[111]}$ and cubic sites predicted by the UEP method. The muon is located at $\approx$1.3 Å from its closest oxygen atom.

(C) $O_{[111]}$

FIG. 4. Predicted $O_{[111]}$ and cubic (C) μ stopping sites in Fe_3O_4.

A Muon Spectroscopic and Computational Study of the Microscopic Electronic Structure in Thermoelectric Hybrid Silicon Nanostructures

S. Sturniolo[1], L. Liborio[1] *et. al.*

1 *Theoretical and Computational Physics Group, Scientific Computing Department, RAL, STFC, UK*

Phenylacetylene-capped silicon nanoparticles (Phenyl-SiNPs) have attracted interest as a novel thermoelectric material. Here, we report a combined muon spectroscopic (μSR) and computational study of this material in solution to investigate the microscopic electronic structure of this system. For comparison, the model molecular compound tetrakis(2-phenylethynyl)silane has also been investigated. μSR measurements have shown that the muon isotropic hyperfine coupling constant, A_μ, which depends on spin density at the muon, is greatly reduced for the Phenyl-SiNPs system when compared to the model compound. Results have also demonstrated that the temperature dependence of A_μ for the Phenyl-SiNPs is of opposite sign and proportionally larger when compared to the model compound. Ab initio DFT methods have allowed us to determine the muon addition site in the model compound, while a wider computational study using both DFTB+ and CASTEP offers a qualitative explanation for the reduced coupling seen in the Phenyl-SiNPs system and also the contrasting temperature dependence of A_μ for the two materials. Calculations suggest an increase in the density of electronic states at the energy level of the highest occupied molecular state for the Phenyl-SiNPs, even in the presence of an organic cap, suggesting a mechanism for enhanced electron transport in this system when compared to the tetrakis model compound.
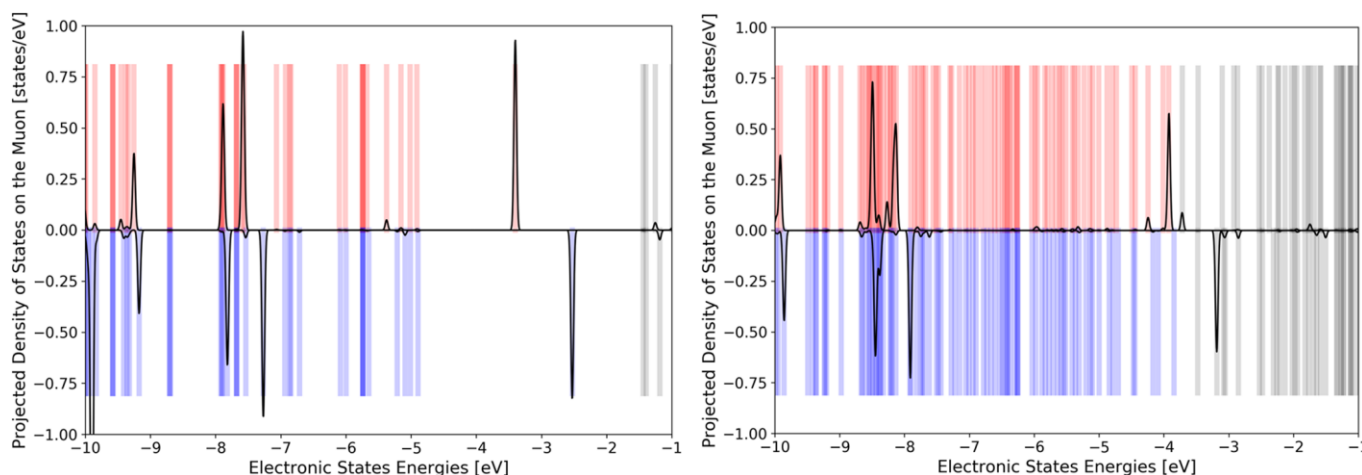
Calculated electronic energy states of the tetrakis(2-phenylethynyl)silane muoniated molecule (left) and those of the muoniated 6 Å Phenyl-SiNPs with six ligands attached (right). The red and blue vertical stripes represent the occupied electronic energy states for the α and β spin channels. The grey vertical stripes represent the unoccupied electronic energy states in both channels. The black plots superimposed on these electronic energy states represent the projected electronic states associated with the muon.

Observation of a molecular muonium polaron and its application to probing magnetic and electronic states

S. Sturniolo[1], L. Liborio[1], E. Poli[1], G. Teobaldi[1], D. Jochym[1] *et. al.*
1 *Theoretical and Computational Physics Group, Scientific Computing Department, RAL, STFC, UK*

Muonium is a combination of first- and second-generation matter formed by the electrostatic interaction be- tween an electron and an antimuon (μ+). Although a well-known physical system, their ability to form collective excitations in molecules had not been observed. Here, we give evidence for the detection of a muonium state that propagates in a molecular semiconductor lattice via thermally activated dynamics: a muonium polaron. By measuring the temperature dependence of the depolarization of the muonium state in C_{60}, we observe a thermal narrowing of the hyperfine distribution that we attribute to the dynamics of the muonium between molecular sites. As a result of the time scale for muonium decay, the energies involved, charge and spin selectivity, this quasiparticle is a widely applicable experimental tool. It is an excellent probe of emerging electronic, dynamic, and magnetic states at interfaces and in low dimensional systems, where direct spatial probing is an experimental challenge owing to the buried interface, nanoscale elements providing the functionality localization and small magnitude of the effects.
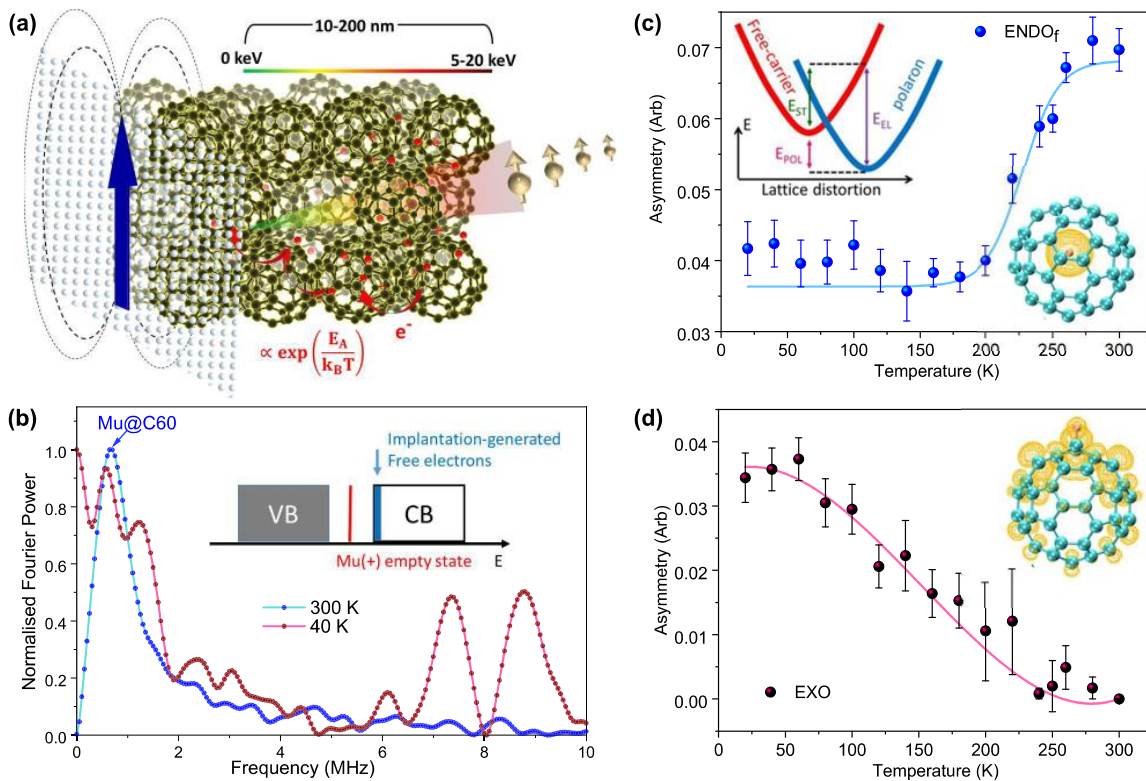
(a) Schematic picture of the formation of a muonium state via ionization, charge hopping, and trapping then coupled with molecular rotations. Its oscillation frequency is sensitive to, e.g., the electron transfer and emergent magnetism at interfaces. (b) Fourier transform of the time domain asymmetry data at zero field for a 210-nm- thick amorphous C_{60} film on a thermally oxidized Si substrate. The observed frequencies at 1.2, 7.4, and 8.6 MHz corresponds to a muonium state that is external to the C_{60} and is observable at 40 K. At 300 K, only the muonium state internal to the C_{60} is observed. Inset: (∼keV) muon-beam generated free carriers remain delocalized in the conduction band (CB) of the C_{60} film, leaving the e-acceptor state of the μ+ empty. (c) The temperature dependence of the asymmetry attributed to the low-frequency muonium state internal to the C_{60} together with the calculated spin-density using the PBE exchange-correlation (XC) functional (yellow: 10–6 μB Å–3). A

semiempirical model has been used to fit the temperature dependence leading to an activation energy (equivalent to $-EPOL$) for the muonium state internal to the C_{60} of EA = 300 ± 100 meV [30]. (d) Temperature dependence of the signal fraction that corresponds to the muonium state that is external to the C_{60}, also with the calculated PBE spin-density (yellow: 10–6 μB Å–3). The muonium state that is external to the C_{60} state becomes more apparent as we cool the system through the glass transition and the molecular rotations are frozen.

External injection from an RF linac as a testbed for staged plasma acceleration

L. R. Reid,[1, 2, □] J. Christie,[1, 2] and L. Corner[1, 2, †]

[1]*Department of Mechanical, Materials & Aerospace Engineering,*
University of Liverpool, The Quadrangle, Liverpool, L69 3GH
[2]*Cockcroft Institute, Sci-Tech Daresbury, Warrington, WA4 4AD*
(Dated: March 30, 2022)

Any high energy physics application of plasma based accelerators will require multiple stages where the beam is passed from one accelerating stage to another once the laser driving the interaction has depleted or the beam has entered dephasing. Understanding the external injection [1, 2] of the beam from one stage to another so that the desirable properties of the beam are maintained while it is accelerated is therefore critical for future plasma based accelerator facilities [3, 4]. However this is yet to be fully studied theoretically and experimentally. A path to testing and optimising this scheme is to start with a very high quality (low energy spread and emittance) and stable electron beam such as from a radiofrequency (RF) accelerator. This allows the interaction between the laser, plasma and electron beam to be tested in a controlled way. One such source is CLARA based at the STFC Daresbury Laboratory which after a scheduled upgrade will provide a high quality, repeatable election beam with of energy 250 MeV to users at a dedicated experimental area called "FEBE" (Full Energy Beam Exploitation). Particle-in-cell simulations using the code FBPIC [5, 6] were preformed on the SCARF cluster of the acceleration of the CLARA electron beam in a plasma acceleration stage driven by a high intensity laser pulse. The code is based on CUDA so GPU nodes of SCARF were utilised for this work. SCARF gave access to multiple nodes in parallel allowing for larger, more ambitious simulations which are too large for university scale computing clusters. We show that the FEBE beamline provides an opportunity for proposed electron acceleration schemes which simultaneously accelerate the beam while maintaining the initial beam quality to be tested in the laboratory for the first time. These simulations aimed to optimise the laser and plasma profile for two types of laser driver: a high peak power Ti:Sapphire laser typically found at plasma accelerator facilities and a high average power Ytterbium fibre laser.

For the Ti:Sapphire laser a peak power of 250 TW is used with $w_0 = 60$ μm, $\tau_{FWHM} = 25$ fs giving $a_0 = 1.4$. The electron beam has transverse and longitudinal lengths of $\sigma_r = 5$ μm and $\sigma_z = 1.5$ μm with 0.5 pC of charge, 1% RMS energy spread and normalised emittance 1 mm mrad. The plasma has plateau density of 1×10^{17} cm^{-3} and length 50 mm with a parabolic transverse profile to guide the laser through the plasma with a constant spot size. The vacuum to plasma transitions are linear and the same length for the up and down ramps and are in addition to the length of the plateau region. To couple the electron beam into the plasma and maintain the low energy spread and emittance, the length of the vacuum to plasma transition had to be optimised [7, 8]. This density transition allows the beam transverse envelope to be slowly reduced from the focus size to the matched plasma size which occurs when the beam emittance is balanced by the focusing field of the plasma wave $\sigma_{matched} = 1.04$ μm. A linear vacuum to
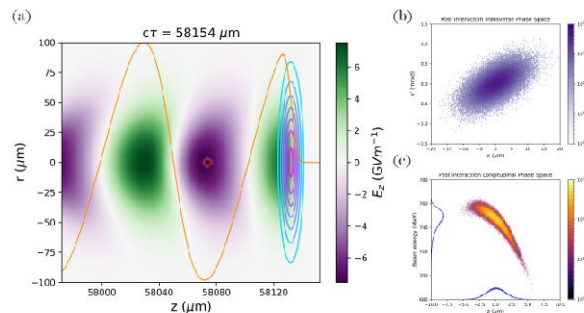
FIG. 1. (a) Accelerating (E_z) field of plasma with electron beam in red and position of laser represented by contours of intensity. Orange line shows shape of field along $r = 0$, scaled to fit inside box. (b) Transverse phase space of FEBE beam at the exit of the plasma. (c) Post interaction longitudinal phase space of FEBE beam.

□ Lewis.Reid@Liverpool.ac.uk
† Laura.Corner@Liverpool.ac.uk

Many-Body Quantum Muon Effects and Quadrupolar Coupling in Solid Nitrogen

M. Gomilšek[1,2,3], F. L. Pratt[4], S. P. Cottrell[4], S. J. Clark[3] and T. Lancaster[3]

[1] *Jožef Stefan Institute, Jamova c. 39, SI-1000 Ljubljana, Slovenia*
[2] *Faculty of Mathematics and Physics, University of Ljubljana, Jadranska u. 19, SI-1000 Ljubljana, Slovenia*
[3] *Department of Physics, Durham University, South Road, Durham DH1 3LE, United Kingdom*
[4] *ISIS Muon Group, Science and Technology Facilities Council (STFC), Didcot OX11 0QX, United Kingdom*

Once considered exotic, implanted muons are nowadays routinely used as exquisite and unique probes of magnetic materials at the atomic scale. Here, muon spin relaxation (µSR) has been indispensable in establishing some highly visible recent results in the field of quantum magnetism [1]. However, for unambiguous interpretation of experimental data, a thorough understanding of quantum zero-point motion (ZPM) of muons inside materials is essential. Namely, while ZPM of light nuclei like hydrogen is known to strongly affect the structure and dynamics of many materials [2], quantum effects of muons in solids can be even stronger due to the low mass of muons (~1/9 the mass of a proton), which can qualitatively change the measured µSR signal.

There has been much interest in using *ab initio* (often density functional theory, DFT) computation of muon stopping sites in materials to aid in the interpretation of µSR measurements. However, most computational techniques employed have either neglected ZPM of muons in solids, or applied uncontrolled approximations to it, with little clarity around their applicability in practice. To address this, we have developed a unified description of ZPM of light particles in materials [3], clarifying the role many-body quantum entanglement and anharmonicity play in determining its behavior, and identifying several distinct ZPM regimes. We applied these insights, as well as extensive DFT and path-integral molecular dynamics (PIMD) calculations, to our µSR quadrupolar level-crossing measurements (Fig. 1) to significantly improve the experimental accuracy of an important constant: the ^{14}N nuclear quadrupolar coupling constant of solid nitrogen, α–N_2, which represents the first improvement in its accuracy in over 45 years.
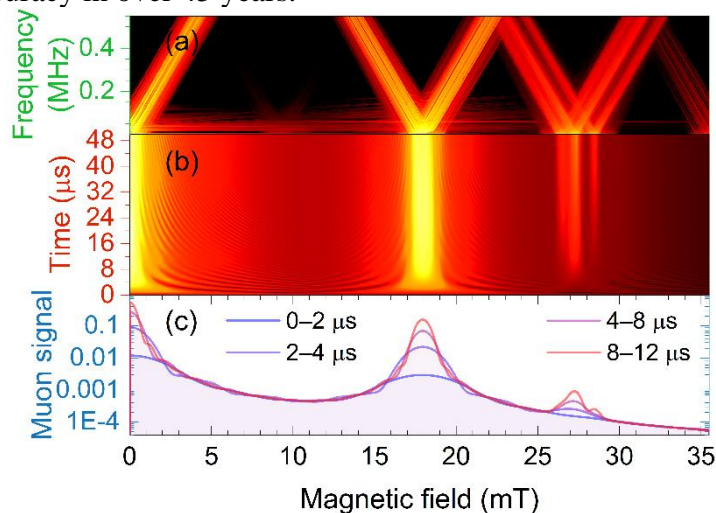
Figure 4: Quadrupolar level crossing resonance spectra from path-integral molecular-dynamics calculations of quantum muon motion in solid nitrogen as a function of (a) frequency, (b) time, or (c) integrated over time.

[1] M. Gomilšek *et al.*, Nat. Phys. **15**, 754 (2019).
[2] T. E. Markland and M. Ceriotti, Nat. Rev. Chem. **2**, 0109 (2018).
[3] M. Gomilšek *et al.*, arXiv:2202.05859.

Randomness-driven Spin Liquid in a Frustrated Antiferromagnet

J. Khatua[1], M. Gomilšek[2,3], J. C. Orain[4], A. M. Strydom[5,6], Z. Jagličić[3,7], C. V. Colin[8], S. Petit[9], A. Ozarowski[10], L. Mangin-Thro[11], K. Sethupathi[1], M.S. Ramachandra Rao[1], A. Zorko[2,3] and P. Khuntia[1]

[1] *Indian Institute of Technology Madras, Chennai 600036, India*
[2] *Jožef Stefan Institute, Jamova c. 39, 1000 Ljubljana, Slovenia*
[3] *University of Ljubljana, 1000 Ljubljana, Slovenia*
[4] *Paul Scherrer Institute, LMU 5232 Villigen PSI, Switzerland*
[5] *University of Johannesburg, PO Box 524, Auckland Park 2006, South Africa*
[6] *Max Planck Institute for Chemical Physics of Solids, 40 Nöthnitzerstr., Dresden D-01187, Germany*
[7] *Institute of Mathematics, Physics and Mechanics, 1000 Ljubljana, Slovenia*
[8] *Institut Néel, Université Grenoble Alpes, CNRS, Grenoble, 38042, France*
[9] *LLB, CEA, CNRS, Université Paris-Saclay, CEA Saclay, 91191 Gif-sur-Yvette, France*
[10] *National High Magnetic Field Laboratory, Florida State University, Tallahassee, FL 32310, USA*
[11] *Institut Laue-Langevin, 38042 Grenoble, France*

The impact of quenched disorder on the ground state of frustrated magnets is a pressing topic both from a fundamental point of view, but also as a practical matter, since disorder in many of the most studied quantum magnets, like the kagome antiferromagnet herbertsmithite, is often unavoidable [1]. Particularly interesting are cases where strong disorder stabilizes a randomness-induced spin-liquid state (a disordered, dynamical, and highly-entangled ground state of spins); for example a random-singlet state where a distribution of antiferromagnetic exchange interaction strengths between spins leads to characteristic, unconventional scaling laws for observables like magnetic susceptibility and specific heat at low temperatures [2].

The recently synthesized frustrated antiferromagnet Li_4CuTeO_6 (LCTO) [3] consists of spin-1/2 Cu^{2+} ions forming parallel random spin chain fragments with random 3D inter-chain couplings (Fig. 1) [4]. Using *ab initio* density functional theory (DFT) and exact diagonalization calculations to complement thermodynamic, muon spin relaxation, electron spin resonance, and scattering measurements, we find that disorder in LCTO stabilizes a novel, dynamical random-singlet state with peculiar scaling behavior but no spin freezing down to 45 mK. LCTO thus represents a rare, and particularly clear, realization of a 3D randomness-driven spin-liquid state.
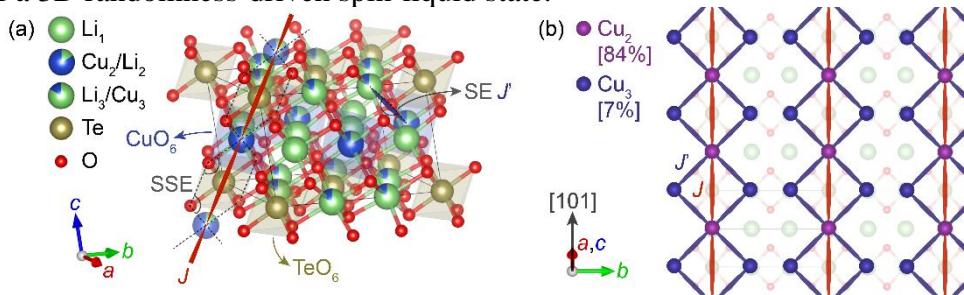
Figure 5: (a) Crystal structure and (b) high temperature random spin model of Li_4CuTeO_6 from density functional theory, consisting of random 1D spin chain and ladder fragments that couple in a random 3D lattice.

[1] M. R. Norman, Rev. Mod. Phys. **88**, 041002 (2016).
[2] I. Kimchi, A. Nahum, and T. Senthil, Phys. Rev. X **8**, 031028 (2018).
[3] V. Kumar *et al.*, Inorg. Chem. **51**, 10471 (2012).
[4] J. Khatua, M. Gomilšek *et al.*, to appear in Comm. Phys.

Origin of Magnetic Ordering in a Structurally Perfect Quantum Kagome Antiferromagnet

M. Gomilšek[1,2], T. Arh[1], P. Prelovšek[1], M. Pregelj[1], M. Klanjšek[1], A. Ozarowski[3], S. J. Clark[2], T. Lancaster[2], W. Sun[4], J.-X. Mi[4] and A. Zorko[1,5]

[1] *Jožef Stefan Institute, Jamova c. 39, SI-1000 Ljubljana, Slovenia*
[2] *Centre for Materials Physics, Durham University, South Road, Durham, DH1 3LE, UK*
[3] *National High Magnetic Field Laboratory, Florida State University, Tallahassee, Florida 32310, USA*
[4] *Fujian Provincial Key Laboratory of Advanced Materials, Department of Materials Science and Engineering, College of Materials, Xiamen University, Xiamen 361005, Fujian Province, People's Republic of China*
[5] *Faculty of Mathematics and Physics, University of Ljubljana, Jadranska u. 19, SI-1000 Ljubljana, Slovenia*

A common problem in magnetism is the determination of relevant microscopic spin-model exchange parameters, which give rise to a material's magnetic behaviour. Complementary to experimental measurements, whose interpretation depends on an assumed spin model, various *ab initio* calculation schemes have been developed to directly derive a full spin model from a material's crystal structure [1]. Amongst the most widely used approaches is the broken-symmetry (BS, total-energy) method based on density functional theory (DFT) calculations.

We have performed large-scale BS DFT calculations at the LDA+U level to derive a spin model for $YCu_3(OH)_6Cl_3$ [2], a new and rare realization of a defect- and distortion-free quantum kagome antiferromagnet (KAFM) [3,4]. Unlike the ideal nearest-neighbour Heisenberg KAFM, which has a disordered quantum-spin-liquid (QSL) ground state, $YCu_3(OH)_6Cl_3$ magnetically orders at low T. BS DFT calculations, performed in part using SCARF computational facilities with the CASTEP DFT code [5], in combination with experimental results (Fig. 1) [2] have enabled us to determine that the origin of magnetic order in $YCu_3(OH)_6Cl_3$ is strong Dzyaloshinskii-Moriya magnetic anisotropy that pushes across the quantum critical point separating a QSL from a magnetically-ordered KAFM ground state.
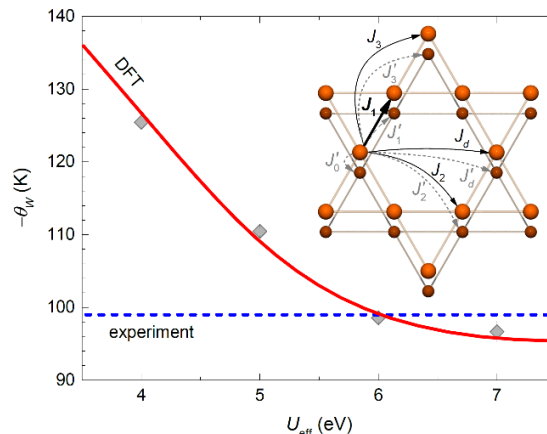
Figure 1: Dependence of the BS DFT+U calculated Weiss temperature (red) on the Hubbard U compared with experiment (blue) for the kagome antiferromagnet $YCu_3(OH)_6Cl_3$. Inset shows its crystal structure and spin model. Reproduced from [2].

References

[1] K. Riedl *et al.*, Phys. Status Solidi B **256**, 1800684 (2019).
[2] T. Arh *et al.*, Phys. Rev. Lett. **125**, 027203 (2020).
[3] A. Zorko *et al.*, Phys. Rev. B **99**, 214441 (2019).
[4] A. Zorko *et al.*, Phys. Rev. B **100**, 144420 (2019).
[5] S. J. Clark *et al.*, Z. Kristallogr. Cryst. Mater 220, 567 (2005).

Vibrational Dynamics of crystalline 4-phenylbenzaldehyde from INS spectra and periodic DFT calculations

Mariela M. Nolasco [1],*, Catarina F. Araujo [1], Pedro D. Vaz [2], A. M. Amado [3] and Paulo Ribeiro-Claro [1]

[1] CICECO, Departamento de Química, Universidade de Aveiro, P-3810-193 Aveiro, Portugal; mnolasco@ua.pt (M.M.N.); catarina.araujo@ua.pt (C.F.A.); prc@ua.pt (P.R.C.)

[2] Champalimaud Foundation, Champalimaud Centre for the Unknown, 1400-038 Lisboa, Portugal; pedro.vaz@fundacaochampalimaud.pt

[3] Química-Física Molecular, Departamento de Química, FCTUC, Universidade de Coimbra, P-3004-535 Coimbra, Portugal; amado.am@gmail.com.

* Correspondence: mnolasco@ua.pt; Tel.: +351 234 370 360

The present work is a simple exercise that illustrates the capabilities of periodic DFT as an aid in the vibrational assignment of organic crystals. Despite being more resource intensive than its discrete counterparts, the effort of running periodic DFT calculations pays off by delivering accurate estimated spectra which can be used as a direct guide for assignments. Even though in 4-phenylbenzaldehyde individual units are held together by weak C-H…O and pi-stacking interactions – therefore a prime candidate for the "cheaper" discrete model approach – a periodic description is necessary for reproducing the full vibrational features. An example of the latter is the phenyl torsion, whose frequency is severely underestimated by the single molecule approach, misleading its assignment. From the corrected torsional frequency, the torsional barrier value of $V_4 = 2600$ cm^{-1} is obtained for the phenyl group, well above the value of $V_4 = 860$ cm^{-1} predicted for the isolated molecule. This contrasts with the torsional barrier of the aldehyde group, -CHO, which is clearly less affected by crystal packing (4000 cm^{-1} vs. 3300 cm^{-1}, for crystal and isolated molecule, respectively).
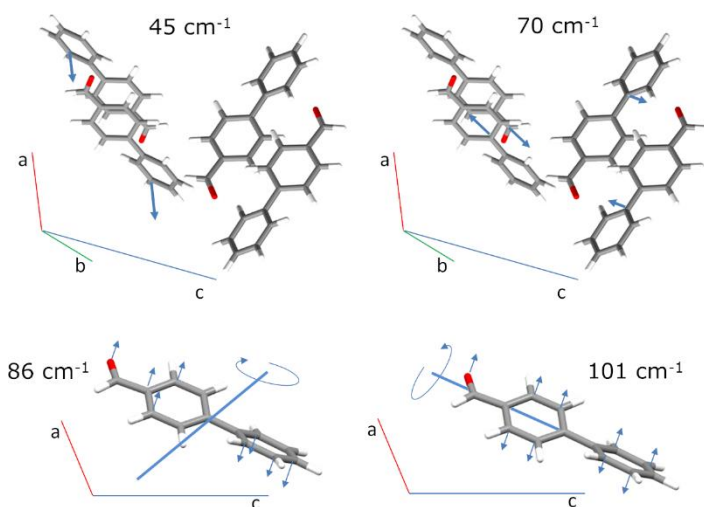
In addition, periodic DFT is fundamental for understanding the low wavenumber region of INS spectra, offering a bird's-eye view of collective modes such as the anti-translational motion of CH···O bonded pairs, a hallmark vibrational mode of systems where C-H…O contacts are an important feature. Figure shows a schematic representation of atomic displacements for the external modes at 45 cm^{-1}, 70 cm^{-1} (translations), 86 cm^{-1} and 101 cm^{-1} (librations). For better readability, only the total displacement of the molecules is shown for translations and only the displacements of heavy atoms is shown for librations. The translational mode at 70 cm^{-1} deserves particular discussion. As depicted in Figure above, the full displacement of the molecules in this external mode results in the "slipping" between pi-stacked molecules, and the "anti-translational" motion of the CH···O bonded molecules. This anti-translational mode, which in fact represents the stretching vibration of the H···O intermolecular hydrogen bond (νH···O), has been identified in other systems through INS spectroscopy [1-4]. In the Chloroform-Acetone complex this mode has been ascribed to the INS band at ca. 82 cm^{-1} [1]. More interestingly, cyclopentanone dimers – with a

symmetric double CH...O contact, as found for 4-phenylbenzaldehyde dimer – present the anti-translational mode at 95 cm^{-1} [2]. Although the mode in 4-phenylbenzaldehyde is not a pure hydrogen-bond stretching, as it also involves the ring slipping of pi-stacking dimers, it falls in the expected wavenumber range for the CH...O interaction.

1. Vaz, P.D.; Nolasco, M.M.; Gil, F.P.S.C.; Ribeiro-Claro, P.J.A.; Tomkinson, J. Hydrogen-bond dynamics of C-H···O interactions: The chloroform···acetone case. *Chem. - A Eur. J.* 2010, 16.
2. Vaz, P.D.; Nolasco, M.M.; Ribeiro-Claro, P.J.A. Intermolecular C-H...O interactions in cyclopentanone: An inelastic neutron scattering study. *Chem. Phys.* 2013, 427.
3. Li, J.C.; Ross, D.K. Evidence for 2 Kinds of Hydrogen-Bond in Ice. *Nature* 1993, 365, 327–329.
4. Corsaro, C.; Crupi, V.; Longo, F.; Majolino, D.; Venuti, V.; Wanderlingh, U. Mobility of water in Linde type A synthetic zeolites: an inelastic neutron scattering study. *J. Physics-Condensed Matter* 2005, 17, 7925–7934.

New insights on the vibrational dynamics of 2-methoxy-, 4-methoxy- and 4-ethoxy-benzaldehyde from INS spectra and periodic DFT calculations

Paulo J.A. Ribeiro-Claro [1], Pedro D. Vaz [2], Mariela Nolasco [1,*], Francisco P.S.C. Gil [3], Luís A.E. Batista de Carvalho [4], M. Paula M. Marques [4,5] and Ana M. Amado [4]

CICECO, Departamento de Química, Universidade de Aveiro, P-3810-193 Aveiro, Portugal; prc@ua.pt

[2] Champalimaud Foundation, Champalimaud Centre for the Unknown, 1400-038 Lisboa, Portugal;pedro.vaz@fundacaochampalimaud.pt

[3] Departamento de Física, Universidade de Coimbra, 3004-516 Coimbra, Portugal; fgil@uc.pt

[4] Química-Física Molecular, Departamento de Química, Universidade de Coimbra, 3004-535 Coimbra, Portugal; labc@ci.uc.pt (L.A.B.E.B.C.); amadoam@gmail.com (A.M.A.)

[5] Departamento de Ciências da Vida, Universidade de Coimbra, 3000-456 Coimbra, Portugal; pmc@ci.uc.pt

* Correspondence: mnolasco@ua.pt; Tel.:+351-234-370-360

The dynamics of 2-methoxybenzaldehyde, 4-methoxybenzaldehyde, and 4-ethoxybenzaldehyde in the solid state are assessed through INS spectroscopy combined with periodic DFT calculations. In the absence of experimental data for 4-ethoxybenzaldehyde, a tentative crystal structure, based on the similarity with 4-methoxybenzaldehyde, is considered and evaluated.
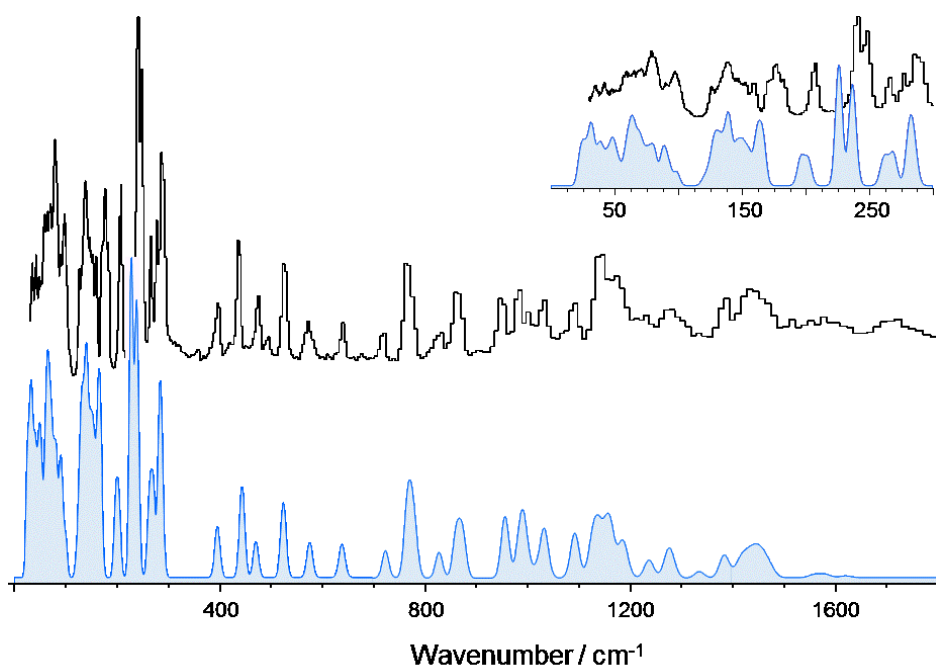
Figure shows the INS spectra of 2MeOB up to 1800 cm^{-1}: Experimental (top) and simulated from periodic DFT calculations (bottom, CASTEP).The inset provides a detailed view of the low wavenumber region. As it becomes obvious from Fig. 2, there is a remarkable nearly one-to-one match between the calculated and observed bands.

The excellent agreement between calculated and experimental INS spectra provides a good basis for interpreting the vibrational spectra and assessing the structure and dynamics of the title compounds in the crystal form. The molecular (internal) modes are better described than the collective (external) modes, a well-known drawback of periodic calculations. Nevertheless, several spectral features are unambiguously assigned and torsional potential barriers for the methyl groups are obtained. The intramolecular nature of the potential energy barrier about O-CH$_3$

bonds compares with the one reported for torsion about saturated C-CH$_3$ bonds, while the intermolecular contribution to the potential energy barrier may represent 1/3 of the barrier height.

To the best of our knowledge, there are no reports on the crystal structure of 4-ethoxybenzaldehyde. Since the equilibrium crystal structure is a requirement to obtain the periodic DFT simulation of the INS spectrum, a tentative unit cell was built from the experimental structure of the 4-methoxybenzaldehyde analogue, and optimized with fixed and relaxed cell parameters, as described in the computational section. The optimized cell structures are shown in Figure below.
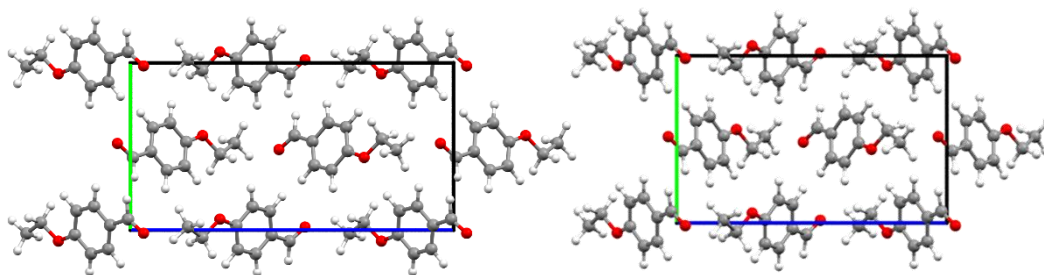
On the whole, the model crystal structure proposed for 4EtOB fails for important details (such as the splitting of the methyl group torsional mode) and it is not unambiguous concerning the description of the collective modes. However, it provides a good description of the vibrational spectra for a large number of spectral features – including the Far-IR region – allowing a reliable assignment of the INS spectrum.

Substrate–Solvent Crosstalk—Effects on Reaction Kinetics and Product Selectivity in Olefin Oxidation Catalysis

Rita N. Sales [1], Samantha K. Callear [2], Pedro D. Vaz [3,4,*] and Carla D. Nunes [1,*]

[1] Centro de Química Estrutural, Faculdade de Ciências da Universidade de Lisboa, 1749-016 Lisboa, Portugal; ritansales@gmail.com

[2] ISIS Neutron & Muon Source, Rutherford Appleton Laboratory, Chilton, Didcot, Oxfordshire OX11 0QX, UK; sam.k.callear@gmail.com

[3] CICECO—Aveiro Institute of Materials, Department of Chemistry, University of Aveiro, 3810-193 Aveiro, Portugal

[4] Champalimaud Foundation, Champalimaud Centre for the Unknown, 1400-038 Lisboa, Portugal

[*] Correspondence: pedro.vaz@fundacaochampalimaud.pt (P.D.V.); cmnunes@ciencias.ulisboa.pt (C.D.N.); Tel.: +351-210-480-200 (P.D.V.); +351-217-500-876 (C.D.N.)

In this work, we explored how solvents can affect olefin oxidation reactions catalyzed by MCM-bpy-Mo catalysts and whether their control can be made with those players. The results of this study demonstrated that polar and apolar aprotic solvents modulated the reactions in different ways. Experimental data showed that acetonitrile (aprotic polar) could largely hinder the reaction rate, whereas toluene (aprotic apolar) did not. Based on recent reports assessing the structure of liquids by means of neutron scattering techniques [1,2], in this work, we conducted an experiment to assess the local structure of styrene and the solvents mentioned above (acetonitrile and toluene) under the same *in operando* catalysis conditions. Styrene was chosen given that it is readily available as a deuterated isotopomer, which is a requirement for such experiments. According to Figure 1, the neutron diffraction experiment (SANDALS) demonstrated that there are differences correlated with the intermolecular interactions between styrene and the solvents (acetonitrile and toluene).
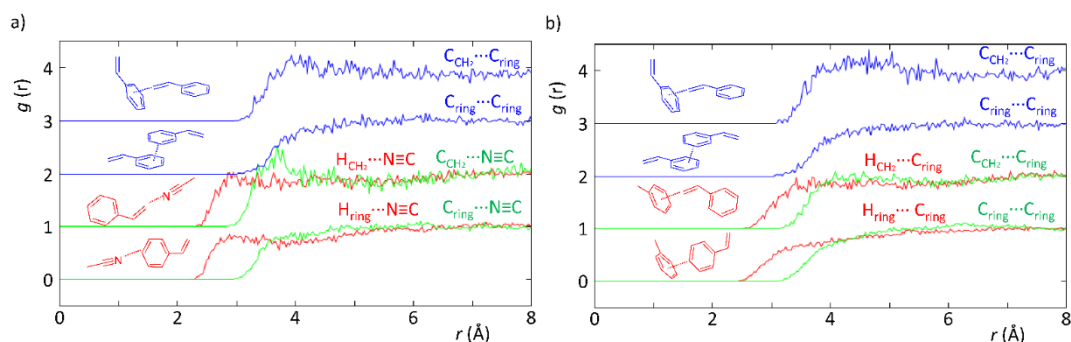
Figure 1. Partial radial distribution functions from EPSR simulation of experimental data obtained with SANDALS data from experiment RB1600022 on the styrene–acetonitrile (**a**) and styrene–toluene (**b**) systems replicating the ratios used in a catalytic experiment.

In particular, the EPSR model revealed the existence of H-bonds when acetonitrile was present, whereas these were absent when toluene was used instead. This is evidenced in Figure 3a by the $H_{CH2} \cdots N \equiv C$ and $H_{ring} \cdots N \equiv C$ curves, which show a more defined peak than those in Figure 3b for the curves representing the $H_{CH2} \cdots C_{ring}$ and $H_{ring} \cdots C_{ring}$ interactions. The reason supporting the fainter peak profile in the latter is indicative of the existence of weaker intermolecular interactions. In fact, this is expected since in the styrene–toluene system (Figure 3b), intermolecular interactions are mostly C–H···π, whereas in the styrene–acetonitrile system (Figure 3a), the interactions are mostly C–H···N, which are stronger yielding; therefore, a higher degree of organization of the mixture as observed. This is verified in Figure 3a, where the $H_{CH2} \cdots N \equiv C$ curve clearly shows the existence of H-bonding between the acetonitrile N-atom and H-atoms in the vinyl group of styrene at lower interaction distances than those found for the H-atoms from the vinyl group and toluene. In addition, the $C_{CH2} \cdots N \equiv C$ curve also displays a very defined peak at 3.6–3.8 Å, confirming the existence of specific geometries most probably interacting by means of hydrogen bonds. These results provide clear and strong evidence that the existence of specific interactions between solvent and substrate is likely to be responsible for the observed kinetic effects and substrate conversion levels.

The above assumptions were evaluated for feasibility under the framework of DFT calculations to assess possible structures of styrene oxide with solvent molecules. As can be seen in Figure 2, the optimized structures of styrene oxide with solvent molecules (acetonitrile or toluene) display the presence of specific interactions through H-bonds. In the case of toluene, the CH$_2$ group in styrene oxide can interact with toluene through C–H⋯π bonds, whereas in the case of acetonitrile, the interaction takes place by means of C–H⋯N bonds.

(**a**)   (**b**)
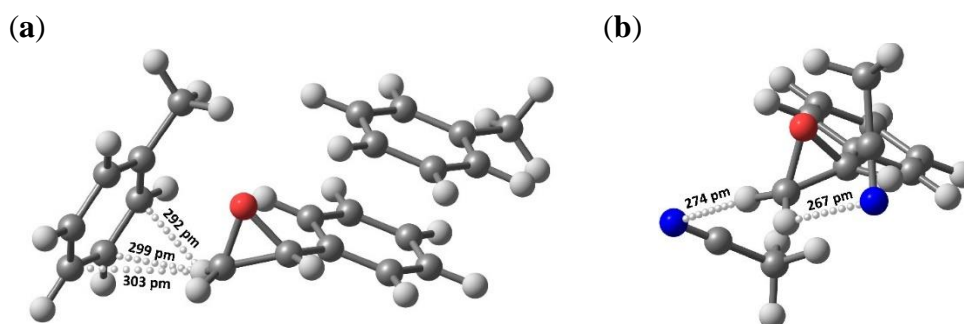
Figure 2. Optimized geometries using a DFT method showing H-bonding interactions between styrene oxide and toluene (C–H⋯π, **a**) or acetonitrile (C–H⋯N, **b**).

DFT results showed that the interaction distance is shorter for the latter— 270 pm on average — compared to that in the former — 298 pm, rendering a stronger bonding energy for the C–H⋯N interactions. These findings were corroborated by NBO topological analyses, where the Wiberg bond orders were 0.009 and 0.002 for the C–H⋯N and C–H⋯π bonds, respectively. In addition, according to Figure 2a, the represented optimized geometry shows a free unbonded H-atom in the oxirane ring, which may also be re-sponsible for the reactivity demonstrated by this system compared with the geometry found for the acetonitrile version (Figure 2b) where both H-atoms are bonded and unavailable for reaction to benzaldehyde. Moreover, the findings from the DFT calculations and those obtained experimentally from the neutron diffraction experiment are coherent

1. Szala-Bilnik, J.; Falkowska, M.; Bowron, D.T.; Hardacre, C.; Youngs, T.G.A. The Structure of Ethylbenzene, Styrene and Phenylacetylene Determined by Total Neutron Scattering. ChemPhysChem 2017, 18, 2541–2548, doi:10.1002/cphc.201700393.

2. Silva, N.U.; Fernandes, C.I.; Nunes, T.G.; Saraiva, M.S.; Nunes, C.D.; Vaz, P.D. Performance evaluation of mesoporous host materials in olefin epoxidation using Mo(II) and Mo(VI) active species-Inorganic vs. hybrid matrix. Appl. Catal. A Gen. 2011, 408, 105–116, doi:10.1016/j.apcata.2011.09.012.

API-DES: improving drug solubility with deep eutectic solvents

Sónia Pedro[1], Carla Vilela[1], Paulo J.A. Ribeiro-Claro[1], Armando J. D. Silvestre[1], Pedro D. Vaz[2], Mariela Nolasco[1]

[1] CICECO, Departamento de Química, Universidade de Aveiro, P-3810-193 Aveiro, Portugal; mnolasco@ua.pt

[2] Champalimaud Foundation, Champalimaud Centre for the Unknown, 1400-038 Lisboa, Portugal;

Improving the efficiency of existing drugs is currently one of the major goals of pharmaceutical industries. Rather than developing new drugs with higher bioavailability, which requires new clinical trials, there are undisputable assurances and profits in improving the already tried-and-tested therapies.[1]. One of the characteristics with great ceiling for improvement is hydrophilicity: approximately 40% of approved drugs and nearly 90% of drugs under development are poorly water soluble, which leads to low bioavailability and permeation [2]. These drugs are generally marketed in the solid form, often exhibiting polymorphism with changes in their chemical stability, solubility and absorption, leading to less effective treatments and undesired side effects. Thereby, there is a demand for alternative and sustainable solvents capable of improving the solubility of active pharmaceutical ingredients (API) in aqueous media and support a maximum therapeutic response in the target, leading to faster therapeutic effects. In this sense, deep eutectic solvents [3] comprising active pharmaceutical ingredients (API-DES) have emerged as alternative solvents capable of solubilizing poorly soluble compounds and enhance their bioavailability, being suitable for posterior use in low-toxicity drug delivery systems [1].
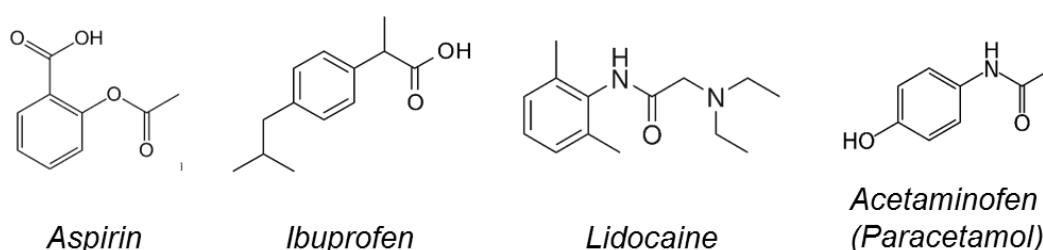
Scheme 1. Chemical structures of APIs to be studied in this project.

Despite the existence of several studies on API-DES in literature, there is still a profound lack of information on the molecular-level mechanisms responsible for the high solubilisation capacity of DES [5]. Therefore, strong efforts must be made to fill this gap. Results on this field will allow the proper design of API-DES for target applications, avoiding trial-and-error approaches, and changing the therapeutics efficacy as we know it. Our team is particularly focused on the DES capacity to increase the solubility of APIs in aqueous solution.

The herein proposed systems are well-characterized and include the APIs often reported as "model drugs" for API-DES solubility studies. For instance, Aspirin:Reline system profits from the use of a small API molecule with an "acquainted" DES [4]. Ibuprofen has been one of the most studied APIs for dissolution in DES [1] and recent results from our lab show a >1000-fold increase of solubility in Arginine:Glycerol mixture, compared with its solubility in water. For the lidocaine-DES system, a recent theoretical study suggests that the molecules forming the DES tend to be placed above the lidocaine molecular plan, centred above the phenyl ring, carbonyl and amine groups [5]. CASTEP simulations to understand the dynamics of the APIs in DES as assessed by INS on TOSCA will be of utmost importance as evidenced by the preliminary results shown in Figure 1.
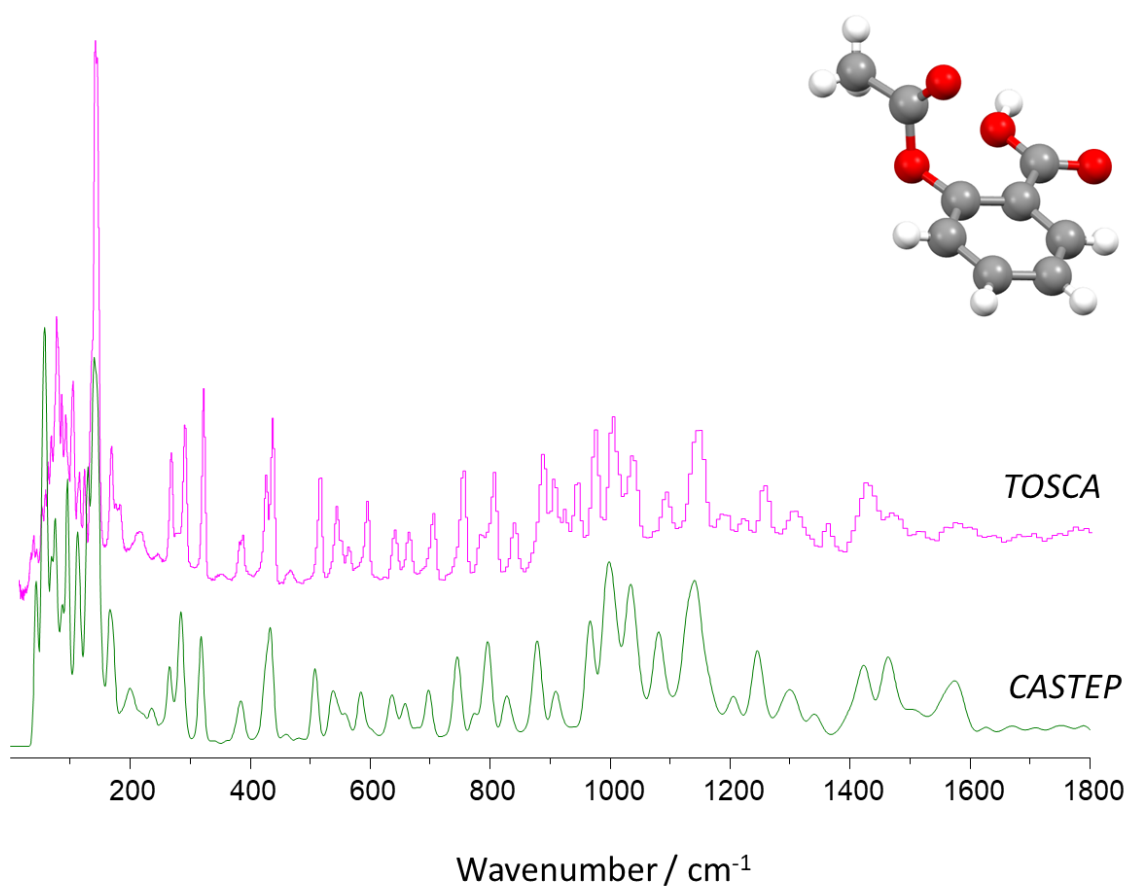
Figure 1. Comparison of INS experimental and simulated spectra for acetylsalicylic acid (aspirin) API.

[1] Pedro, S.N.; Freire, M.G.; Freire, C.S.R.; Silvestre, A.J.D. "Deep eutectic solvents comprising active pharmaceutical ingredients in the development of drug delivery systems". Expert Opinion on Drug Delivery (2019). DOI: 10.1080/17425247.2019.1604680

[2] Kalepu, S.; Nekkanti, V. "Insoluble drug delivery strategies: review of recent advances and business prospects". Acta Pharm. Sin. B 5 (2015) 442–453. DOI: 10.1016/j.apsb.2015.07.003

[3] DES are formed by the association of a hydrogen bond-capable salt with a neutral hydrogen bond donor species. In the eutectic composition, the mixture has a melting point much lower than that of the corresponding ideal mixture. The iconic example of DES is "Reline", a 1:2 mixture of choline chloride and urea – already studied by us, using INS at TOSCA [3].

[4] Araújo, C.F.; Coutinho, J.A.P.; Nolasco, M.M.; Parker, S.F.; Ribeiro-Claro, P.J.A.; Rudić, S.; Soares, B.I.G.; Vaz, P. D. "Inelastic Neutron Scattering study of Reline". Phys. Chem. Chem. Phys. 19 (2017) 17998-18009. DOI: 10.1039/C7CP01286A

[5] Gutiérrez, A.; Atilhan, M.; Aparicio, S. "A theoretical study on lidocaine solubility in deep eutectic solvents". Phys. Chem. Chem. Phys. 20 (2018) 27464-27473. DOI: 10.1039/C8CP05641B

Magnetic and superconducting ground states probed with computationally assisted spectroscopic techniques.

Ifeanyi John Onuorah, Pietro Bonfà, Muhammad Maikudi Isah, Roberto De Renzi
Department of Mathematical, Physical and Computer Sciences, University of Parma, Italy.

Nuclear Magnetic Resonance (NMR) and Muon Spin Rotation Spectroscopy (µSR) are very powerful tools to probe the magnetic and superconducting states of matter. Both these techniques provide a local probe, i.e. a way to analyse the electronic ground states without introducing spatial averages.

Electronic properties are obtained in both cases by exploiting the hyperfine interaction between the electrons and the nuclei or the muon. Unfortunately, the quantitative details of this interaction are generally unknown. In addition, in the case of µSR, the interstitial position of the muon is also unknown and its injection in the system may, under rare circumstances, perturb the compound under investigation.
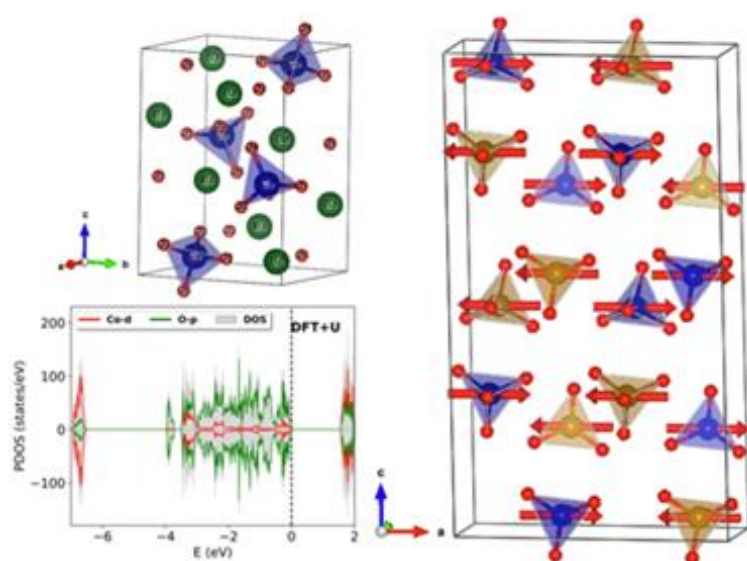
Figure 1: Lattice structure, magnetic order and density of states in Ba_2CoO_4.

Using Density Functional Theory based simulations performed on the SCARF cluster, we have characterized hyperfine couplings and (absence of) muon induced perturbations in a number of compounds including functional materials like Fe_2P [1], the Heavy-Fermion $Yb_2Pd_2In_{1-x}Sn_x$ [2] and a large set of superconductors with time-reversal symmetry breaking TRSB [3].

These simulations, together with NMR and µSR measurements revealed, in the first two cases, the details of the magnetic ground states. On the other hand, in TRSB, the intrinsic nature of the magnetic moment observed below the superconducting transition was established.

In a different study, the magnetic ground state of Ba_2CoO_4, a compound showing peculiar tetrahedrally coordinated magnetic Co, was detailed with *ab initio* simulations [4]. We identified the presence of strong magnetic frustration by modeling the magnetic interactions of the system assuming localized moments and computing the isotropic exchange parameters defining an Heisenberg Hamiltonian. We also described the fundamental role that spin polarized oxygen atoms play in the exchange interaction.
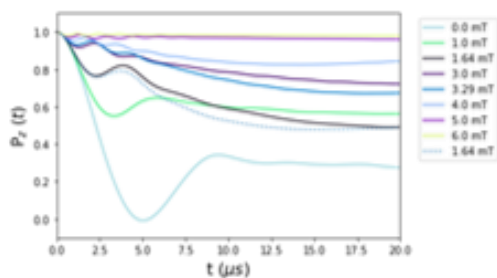
Figure 2: Avoided level crossing in face-center-cubic Al.

Finally, we are developing a combined computational and experimental method for the identification of muon sites in crystalline materials based on the detailed description of the interaction between the muon spin and the nuclear moments. This requires the approximate solution of large spin Hamiltonians that describe the coupling of the muon with a number of nearest neighbours. The method and the associated code have been presented in a recent publication [5].

References

[1] Pietro Bonfà, Muhammad Maikudi Isah, Benjamin A. Frandsen, Ethan J. Gibson, Ekkes Bruck, Ifeanyi John Onuorah, Roberto De Renzi and Giuseppe Allodi "Ab initio modeling and experimental investigation of Fe_2P by DFT and spin spectroscopies", Phy. Rev. Materials 5, 044411, (2021)

[2] G. Lamura, I. J. Onuorah, P. Bonfà, S. Sanna, Z. Shermadini, R. Khasanov, J. C. Orain, C. Baines, F. Gastaldo, M. Giovannini, I. Curlik, A. Dzubinska, G. Pristas, M. Reiffers, A. Martinelli, C. Ritter, B. Joseph, E. Bauer, R. De Renzi, and T. Shiroka, "Pressure-Induced Antiferromagnetic Dome in the Heavy-Fermion $Yb_2Pd_2In_{1-x}Sn_x$ System", Phys. Rev. B 101, 054410, (2020).

[3] B. M. Huddart, I. J. Onuorah, M. M. Isah, P. Bonfà, S. J. Blundell, S. J. Clark, R. De Renzi, T. Lancaster "Intrinsic nature of spontaneous magnetic fields in superconductors with time-reversal symmetry breaking", Phy. Rev. Lett. 127, 237002, (2021).

[4] Ifeanyi John Onuorah, Muhammad Maikudi Isah, Roberto De Renzi, Pietro Bonfà "Frustrated network of indirect exchange paths between tetrahedrally coordinated Co in Ba_2CoO_4 ". Phy. Rev. Materials 5, 124407, (2021).

[5] Pietro Bonfà, Jonathan Frassineti, Muhammad Maikudi Isah, Ifeanyi John Onuorah, Samuele Sanna "UNDI: An open-source library to simulate muon-nuclear interactions in solids",Com Phys Comm 260, 107719,(2021).

The fast electrons transport in hybrid resistive guide target

R. A. B. Alraddadi[1], A. P. L. Robinson[2] and N. C. Woolsey[3].

[1]Physics Department, Science Colleges, King Saud University, Riyadh, Saudi Arabia.
[2]Central Laser Facility, Rutherford Appleton Laboratory, Didcot, UK.
[3]York Plasma Institute, Department of Physics, University of York, York, UK.

The collimation and then guiding the fast electrons is a significant challenge yet it is an essential for the success of certain applications, such as fast ignition (FI) approach to inertial confinement fusion. The resistive guiding concept is promising technique to enable the collimation laser-driven relativistic electron beams [1,2]. When a high atomic number (high-Z) wire is embedded in a lower-Z substrate a resistivity gradient is created across the interface between two the materials. This resistivity change enables the growth of a strong magnetic field in range of kT within 100's of femtoseconds. This fast growing and strong magnetic field limits the transverse expansion of the relativistic electrons confining them to wire enabling the propagation of a beam over long distances (100's μm) along the guide.

In our numerical work using SCARF facilities, hybrid resistive guide targets have been investigated which are made from a pure foam or of combining both foam and solid materials. We use SCARF-derevolutionibus resources to run three-dimensional Hybrid-PIC code ZEPHYROS [3] to investigate their performance. Figure 1 shows an example of these targets as a function of ion density.
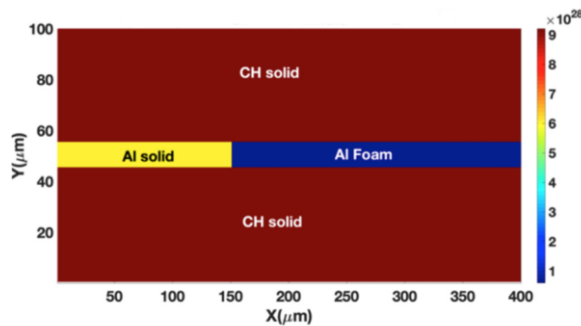
Figure 1: A two-dimensional slice of target ion density profile of hybrid resistive guide.

Using these new guides and typical Vulcan petawatt laser parameters we find that large number of the fast electrons can travel deep through the guide as shown in Figure 2(a). Here, the wire-guide's material is longitudinally changes from solid on to foam. The laser comes from the left to avoid the de-collimating field growth due to the use of foam. Figure 2 (b) shows that strong magnetic fields grow up to 300 μm at 1.5 ps.
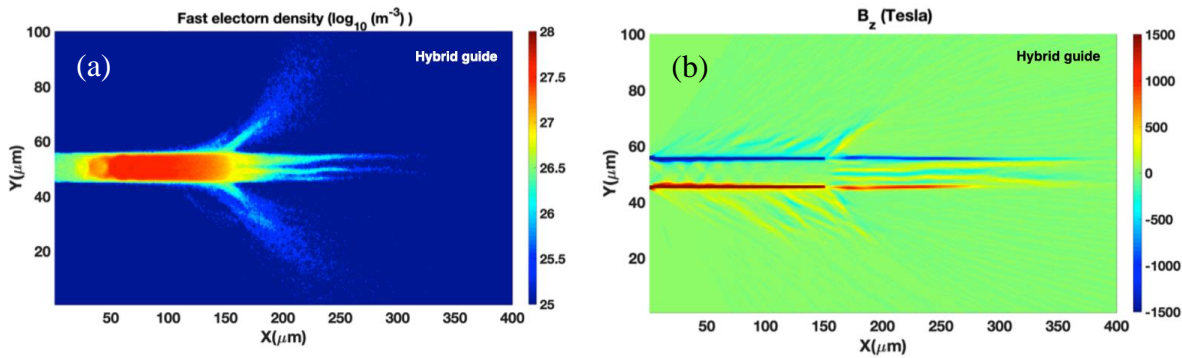
Figure 2: two-dimensional slice of (a) the fast number electron density using the logarithmic color scale, (b) the magnetic flux density, $B_z(T)$.

Our hybrid resistive guide target, uses the excellent collimating properties of a solid density wire-guide at the injection site, and at appropriate distances from this region, couples these electrons to a low collisionality foam wire-guide for an excellent collimation in the foam.

References:

[1] A. P. L. Robinson and M. Sherlock, *Phys. Plasmas*,14 (2007)083105.
[2] A. P. L. Robinson et al, *Phys. Plasmas*, 20(2013)122701.
[3] A. P. L. Robinson et al, *Nuclear Fusion,* 54.5 (2014) 054003.

The original Paper:
R. A. B. Alraddadi, A. P. L. Robinson and N. C. Woolsey, *Phys. Plasmas*, 27, 092701 (2020).

Conferences:

1- Oral presentation given at 16th direct drive fast ignition workshop (Virtual meeting), ELI Beamline, Czech Republic (24/03/2021).
2- Oral presentation given at Christmas CLF High Power Laser Science Community Meeting (Virtual meeting), Guildhall, Abingdon, Oxfordshire, United kingdom (09/02/2021).

Ferroelectricity in CBDC : The role of normal modes

Sanghamitra Mukhopadhyay

ISIS Facility, Rutherford Appleton Laboratory, Science and Technology Facilities Council, UKRI

Organic ferroelectrics are considered as materials of next generation technologies for their potential applications to address global challenges in the sector of energy and biological applications. These lightweight, flexible and nontoxic ferroelectrics have potential applications as ferroelectric random access memories in computers, super capacitors for energy storage, transducers for medical ultrasound imaging and functional materials in flexible electronics [1-2]. As a result of their excellent dielectric, pyro- and piezo-electric properties, comparable to traditional inorganic ferroelectrics, and with unique coexistence of flexibility and ferroelectricity, organic ferroelectrics are candidates of intense research promising of designing new bespoke functional materials. These materials are often hydrogen or halogen bonded molecular crystals [3-4] and dynamics or motion of protons from the centro symmetric to non-centrosymmetric positions are considered as the key mechanisms of their functionality. Some of these ferroelectrics not only exhibit room temperature ferroelectricity, such as croconic acid ($C_5O_5H_2$), their ferroelectric polarisations increase with increasing temperatures. This is counter intuitive due to the fact that strength of hydrogen bonds decrease with increasing temperatures. To understand this mechanism, microscopic knowledge of structure and dynamics of those bonds are thus crucial.

Neutron vibrational spectroscopy experiments along with IR and Raman are done on a number of hydrogen and halogen bonded ferroelectric materials, such as croconic acid ($C_5O_5H_2$), 1-cyclobutene-1,2-dicarboxylic acid (CBDC, $C_6H_8O_4$) and 2-phenylmalondialdehyde (PhMDA, $C_9H_8O_2$) and dichloromethylimidazole ($C_4H_4Cl_2N_2$). Inelastic neutron scattering spectroscopy (INS)are done on TOSCA at ISIS and on Lagrange at ILL [5-8]. Low energy neutron spectroscopies are performed on IRIS and OSIRIS, pico-second quasi-elastic instruments at ISIS, to understand the structures and hydrogen/ halogen bond motifs in these ferroelectrics. The mechanism of ferroelectricity at high temperature is explored from temperature dependent INS and neutron diffraction experiments.
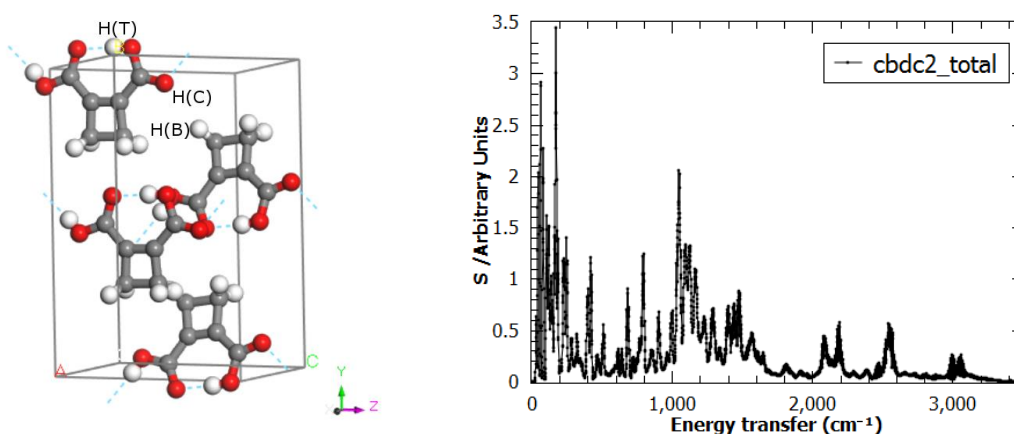
Fig. 1. Left: Hydrogen bond structure in CBDC , Right: Calculated INS of CBDC

Modelling is done using plane wave pseudo potential density functional theory (DFT). Electronic-structures and subsequently lattice dynamics calculations are performed with the DFT code CASTEP on SCARF computer. Optimized normconserving pseudopotentials generated with the Perdew–

Burke–Ernzerhof (PBE) functional within the generalized-gradient approximation (GGA) have been used. The dispersion corrections (PBE+D) to this functional proves as important. This corrections are incorporated following the methodology of Tkatchenko and Scheffler (TS) . A plane-wave cutoff of 800 eV and a Brillouin-zone (BZ) sampling on 18 symmetry reduced k-points are used to converge energy and atomic forces to 9.6×10^{-3} eV per ion and 1.0×10^{-3} eV Å^{-1}, respectively. The lattice dynamics calculations are done via diagonalisation of dynamical matrices computed using density-functional perturbation theory (DFPT) and linear-response methods. Unit-cell polarizations are obtained via Berry-phase method, as implemented in CASTEP. The INS spectrum has been obtained from the calculated phonon densities of states using abINS code as implemented in Mantid [9].

Analysing the spectroscopic data with this DFT based lattice dynamics calculations, we have identified bending modes of hydrogen bond motifs, O-H—O vibrations, as finger print motions of the ferroelectricity of these materials. A correlation with the structure and dynamics have been found by comparing the experimental and calculated INS spectrum. It is found that intensities of the bending modes associated with O-H—O vibrations   directly correlated with the ferroelectricity in these hydrogen bonded ferroelectricities. Further investigation reveals a large LO-TO splitting of O-H stretching modes predicting that hydrogen bonded protons are most sensitive to electric fields and contributes more to the ferroelectric properties of the materials. Due to the sensitivity of these O-H stretching modes on long range Coulomb interactions, any distortion in that interaction may contribute to the ferroelectric properties of that material. It has been proposed that vibrational spectroscopy combining with DFT calculations can be a characterisation tool for predicting ferroelectric properties of CBDC crystals. This microscopic knowledge will be helpful in designing new ferroelectric organic materials for technological applications, such as flexible energy storage materials. More information will be found in the Ref[10].

References:

[1] S. Horiuchi et. al, Nat. Mat. 2008, 7, 267,
[2] F. Kagawa et. al., Nat. Phys. 2010, 6, 169.
[3] A. Stroppa et. al., Phys. Rev. B, 2011, 84, 014101.
[4] M. Owczarek et al. Nature Commn 2016, 7, 1308.
[5] S. Mukhopadhyay et. al., Phys. Chem. Chem. Phys. 2014, 16, 26234.
[6] F. Fernandez-Alonso et. al, J. Phys. Soc. Japan, 2013, 82, SA001,.
[7] S. Mukhopadhyay et. al., Chem Phys., 2013, 427, 95.
[8] S. Mukhopadhyay et. al., Phys. Chem. Chem. Phys. 2017, 19, 32147.
[9] K. Dymkowsk,et al. : Physica B 551, 443 (2018).
[10] S. Mukhopadhyay, J. Phys. Comm. **3**, 113001 (2019)

Assignment of H-adsorption on catalytic Pt nanocluster using ab-initio Molecular Dynamics and Neutron Spectroscopy

Sanghamitra Mukhopadhyay and Stewart Parker

ISIS Facility, Rutherford Appleton Laboratory, Science and Technology Facilities Council, UKRI

Platinum (Pt) is one of the most important material for heterogeneous catalysis of hydrogenation reactions [1,2]. Major applications of using these catalysts include: the reduction of nitroarenes to aromatic aminoarenes for use in polyurethane manufacture, as a component in the three-way automotive catalyst, and as the anode in polymer electrolyte membrane fuel cells (PEMFC). Apart from this technological importance hydrogen on metal surfaces provides a unique opportunity to observe the crossover from classical to quantum dynamics at relatively elevated temperatures [3]. For this reason hydrogen on metal surfaces, and in particular on Pt(111), has received considerable experimental and theoretical interest.

The absorption of hydrogen (H) on Pt is often explored using vibrational spectroscopy. Although a range of experimental and computational work are done on H on Pt in last decade, no concensus has been reached on the assignment of its vibrational spectrum. A recent computational study has shown that in a Pt nanostructure, Pt44, with only {111} facets, undergoes considerable reconstruction as hydrogen is added to produce a $Pt_{44}H_{80}$ C2h tetradecahedron of fcc packing, with 8 {111} facets, 6 {100} facets and 18 apex Pt atoms (see Figure 1). This structure has 18 on-top, 44 twofold, 18 threefold, 0 fourfold coordinated hydrogen and no subsurface hydrogen. The observation of this reconstruction is consistent with the extremely small solubility of hydrogen in platinum.

Lattice dynamics calculations were carried out using the plane-wave pseudopotential method based on density functional theory (DFT) as implemented in the CASTEP code. Perdew-Burke-Ernzerhof (PBE) functional have been used within the generalized gradient approximation (GGA). Geometry optimisation was done by Broyden-Fletcher-Goldfarb-Shanno (BFGS) method where residual forces were converged to within ±0.0047 eV Å-1. Phonon frequencies were obtained by diagonalisation of dynamical matrices computed using density-functional perturbation theory[(DFPT).
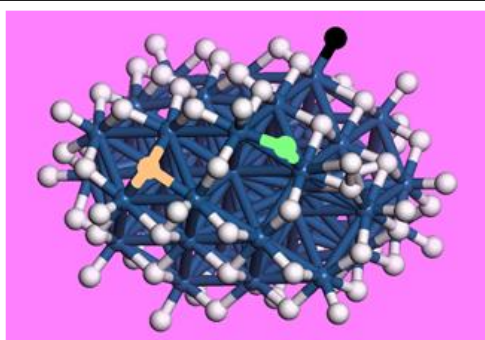
Fig. 1. Pt44H80 nanocluster

To incorporate anharmonic contributions in the vibrational spectra, ab-initio molecular dynamics (AIMD) simulations have been performed on a nanocluster consisting of 44 Pt and 80 hydrogen atoms, at a single k point with periodic boundary condition and plane-wave pseudopotentials as implemented in the CASTEP code. The same pseudopotentials and functionals used for lattice dynamics simulations mentioned above were used. Dispersion corrections to the PBE functional (PBE+D) were included following the methodology of Tkatchenko and Scheffler. The Nose-Hoover thermostat and Andersen-Hoover barostat have been used within NPT ensemble to stabilize temperature and pressure, respectively. The Andersen method of pressure control allows the cell to change volume with temperatures by keeping the shape preserved which is suitable for nanostructure simulations. A relaxation time for the thermostat and the cell was specified as 0.5 ps and 500 ps, respectively. A MD time step of 0.5 fs was used all throughout. The temperature of the system was kept constant at 87 K, which is experimental temperature. The AIMD calculation was run by 80 ps including 10 ps time taken for equilibration. More information about these calculations done on SCARF using 250 CPU will be found elsewhere [4].

The Cartesian densities of states (CDOS) has been calculated by a Fourier-cosine transformation of the time-dependent velocity autocorrelation function (VACF) obtained from AIMD simulations. This calculated CDOS was then weighted by the incoherent neutron-scattering cross section of each species for comparison with the experimental inelastic neutron scattering (INS) data obtained from TOSCA instrument at ISIS (see Fig. 2) .
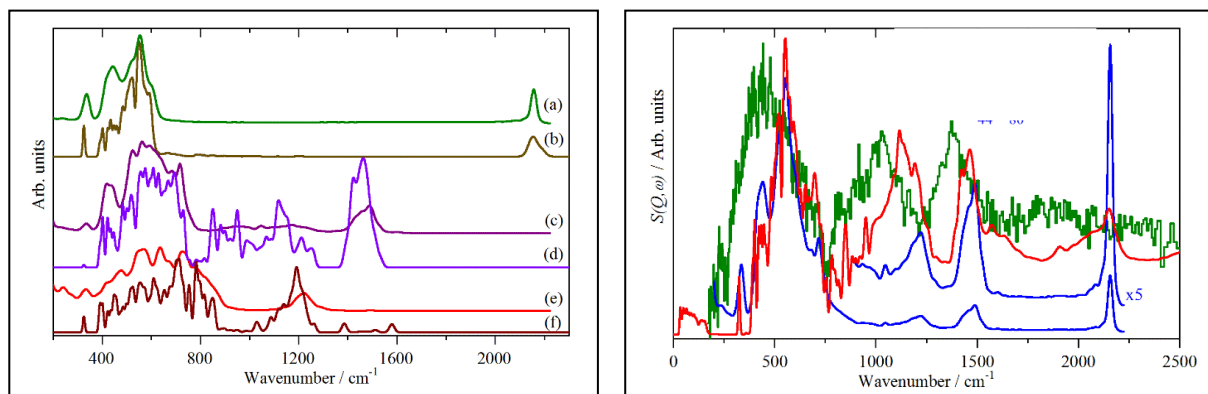
Fig. 2. Left: Partial INS spectra of the Pt44H80 nanoparticle from different cites: (a) and (b) on-top, (c) and (d) twofold, (e) and (f) threefold. (a), (c) and (e) are from the AIMD calculation and (b), (d) and (f) are from the lattice dynamics calculation. Only the fundamental ($0 \rightarrow 1$) transitions are shown.

Right: Experimental and simulated INS spectrum: (Green) experimental spectrum of H on Pt obtained from TOSCA, (Red) calculated spectra obtained from lattice dynamics, (blue) calculated spectra obtained from AIMD.

Our calculations show that dominant contributions in the INS spectra is coming from two fold sites of H, not from the three fold sites as accepted widely previously. It is also found that the anharmonic contributions in these vibrations is negligible. This finding has provided answer to an important scientific issue unsolved for about half a century. For more information see Ref [4].

References:

[1] S. Horch, H. T. Lorensen, S. Helveg, E. Lægsgaard, I. Stensgaard, K. M. Jacobsen, J. K. Nørskov, and Besenbacher, Nature (London) **398**, 134 (1999).
[2] A. P. Graham, A. Menzel, and J. P. Toennies, J. Chem. Phys.**111**, 1676 (1999).
[3] S¸. C. Bˇadescu, S. C. Ying, and T. Ala-Nissilä, Phys. Rev. Lett. **86**, 5092 (2001).
[4] S. F Parker, S Mukhopadhyay, M. J Jiménez-Ruiz, P. W Albers, Chem Eur J **25**, 6496 (2019).

Oxygen Ion Diffusion and Phonons and in Bi_2O_3 and $(Bi_{0.7} Y_{0.3})_2O_3$

Sanghamitra Mukhopadhyay[1], P. Goel[2], M. Gupta[2], R. Mittal[2], S. Skinner[3], S. Rols[4], S. Chaplot[2]

[1]ISIS Facility, Rutherford Appleton Laboratory, Science and Technology Facilities Council, UKRI
[2]Bhaba Atomic Research Center, Mumbai, India
[3]Imperial College London, UK
[4]Institute Laue Langevin, France.

Anion conductors such as Bi_2O_3, yttria stabilized Bi_2O_3, have long been identified as fast oxide ion conductors with applications in a range of energy technologies including fuel cells, photo-catalysts, gas separation membranes and sensors [1-4]. The conductivity of B_2O_3 is two orders of magnitudes higher than that in well known oxygen ion conductor Yittria stabilized Zirconia (YSZ). High ionic conductivity in these compounds helps the migration of oxygen-ion vacancies at high temperature. To fully optimise these materials it is essential to determine the nature of the charge carriers, and to know the dynamics of the oxygen transport. Quasi elastic neutron scattering (QENS) has been used to investigate these oxygen transport at operating temperature upto 1000 K. To interpret the neutron spectroscopic result large scale ab-initio molecular dynamics (AIMD) calculations have been done on Scarf computer.

The AIMD calculations were performed on $2 \times 2 \times 2$ supercell of the monoclinic α-phase of Bi_2O_3 (consisting of 160 atoms) and also a $2 \times 2 \times 2$ supercell of the disordered cubic δ-phase of $(Bi_{0.7} Y_{0.3})_2O_3$ (consisting of 80 atoms). Plane wave pseudo potential calculations were done with energy cut-off 900eV and a single k-point in the Brillouin zone. The generalized gradient approximation (GGA) exchange-correlation within parameterization of Perdew, Burke and Ernzerhof has been used for the computation of total energy and forces using the projected augmented wave (PAW) formalism of DFT. MD calculations were done within NVT ensemble with a time step of 2 femtosecond. VASP computational simulations package have been used for these calculations.

The self-consistent energy and atomic forces converges to 10^{-5} eV per ion and 1.0×10^{-3} eV $Å^{-1}$, respectively. The structure was equilibrated for 10 ps to stabilize the required temperature using NVT simulations using a Nose thermostat. A production run of 60 ps has been performed using NVE simulations. The long time simulations was necessary to predict the long jump time for oxygen diffusion. Production runs have been done at temperatures 300 K, 773 K, 973 K, 1048 K and 1100 K to compare with QENS experiments.

The AIMD calculations show that even at 1000 K in δ-phase Bi_2O_3, Bi–Bi correlations remain ordered like in the crystalline lattice, on the other hand the correlations between O–O show liquid like disordered behaviour. Time dependent positions of selected oxygen ions are shown in Fig. 1. It shows that the two selected oxygen ions diffuse first along the crystallographic b-direction and then along the c-direction.
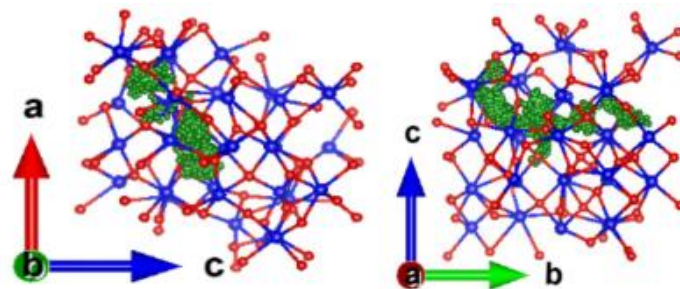
Fig. 1.   Trajectories of selected O atoms at 1000 K in δ-Bi2O3. Trajectories of two different oxygen atoms are shown. Red : O, blue : Bi ; Green coloured dots represents the time-dependent positions of the selected oxygen atoms.
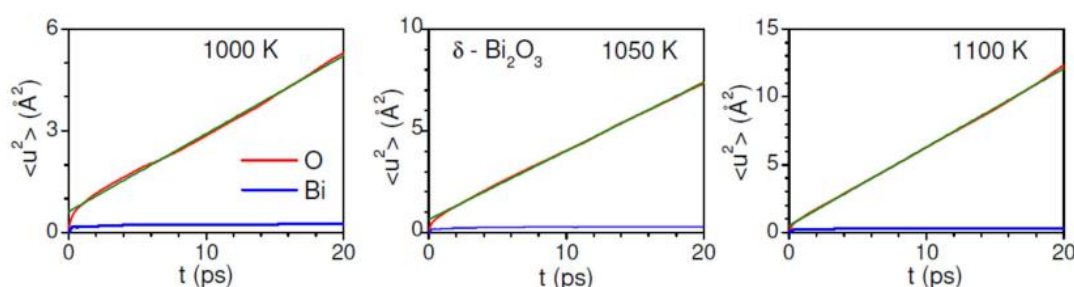
Fig.2. Calculated mean square displacement of δ-Bi2O3. Partial displacement for O and Bi are shown for three different simulations temperatures.

The calculated mean square displacement (MSD) ($<u^2>$) of various atoms in amorphous δ-Bi_2O_3 at various temperatures is shown in Fig. 2. From the plot it is clear that the MSD of Bi atoms is small and does not increase with time. This implies that Bi atoms do not diffuse
and form a rigid framework, while oxygen atoms show significant diffusion. The calculated value of the MSD for δ-Bi2O3 at 1100 K at 20 ps is obtained to be about 13 $Å^2$ which is in
agreement with reported results [4].

From the calculations it has been found that oxygen ions travels through the solid using jumping motions. For low Q, i.e., below 1.3 $Å^{-1}$ the jump length and relaxation time are of 10.8 Å and 5.1 ps, respectively. On the other hand, for Q above 1.3 $Å^{-1}$ jump distance and relaxation time are of 3.3 Å and 4.1 ps, respectively. The calculated diffusion constant of oxygens compared well with that obtained from QENS experiments [5] . This shows that ab-initio MD is an essential tools to interpret neutron experiments, particularly QENS.

References

1.   R.J. Packer and S.J. Skinner, Adv. Mater. **22,** 1616 (2010).
2.   M. Burriel, et al., J. Mater.Chem.**18**, 416 (2008).
3.   S.J. Skinner et. al, Solid State Ion., **135**, 709 (2000) .
4.   J. Wind, R. A. Mole, D. Yu and C. D. Ling Chem. Mater. **29** 7408 (2017).
5.   P. Goel, M. Gupta, R. Mittal, S. Skinner, S. Mukhopadhyay, S. Rols, S. Chaplot. J. Phys. Cond. Mat **32**, 334002 (2020).

Spectroscopic Signatures of Hydrogen-Bonding Motifs in Protonic Ionic Liquid Systems: Insights from Diethylammonium Nitrate in the Solid State

Isabel Vázquez-Fernández[1], Kacper Druzbicki[2,3], ˙Felix Fernandez-Alonso[2,4,5,6], Sanghamitra Mukhopadhyay[7,8], Peter Nockemann[1], Stewart F. Parker[7], Svemir Rudić[7], Simona-Maria Stana[1], John Tomkinson[7], Darius J. Yeadon[1], Kenneth R. Seddon[1], and Natalia V. Plechkova[1]

1. The QUILL Research Centre, The Queen's University of Belfast
2. Materials Physics Center, CSIC-UPV/EHU
3. Centre of Molecular and Macromolecular Studies, Polish Academy of Sciences
4. Donostia International Physics Center (DIPC)
5. Department of Physics and Astronomy, University College London
6. IKERBASQUE, Basque Foundation for Science
7. ISIS Facility, Rutherford Appleton Laboratory
8. Department of Materials, Imperial College London

Ionic liquids (ILs) have attracted a phenomenal amount of attention over the past two decades, but the focus has been principally on the development of industrial applications and sustainable processes. Although many theoretical models of IL structures have been developed and published, we are still a long way from predictive certainty, or even good qualitative models for describing the principle interionic interactions. To fill this gap, a robust physico-chemical interpretation of the structure and vibrational response of an archetypal IL system has been explored using harmonic phonon calculations and ab initio molecular dynamics (AIMD) simulations.[1]
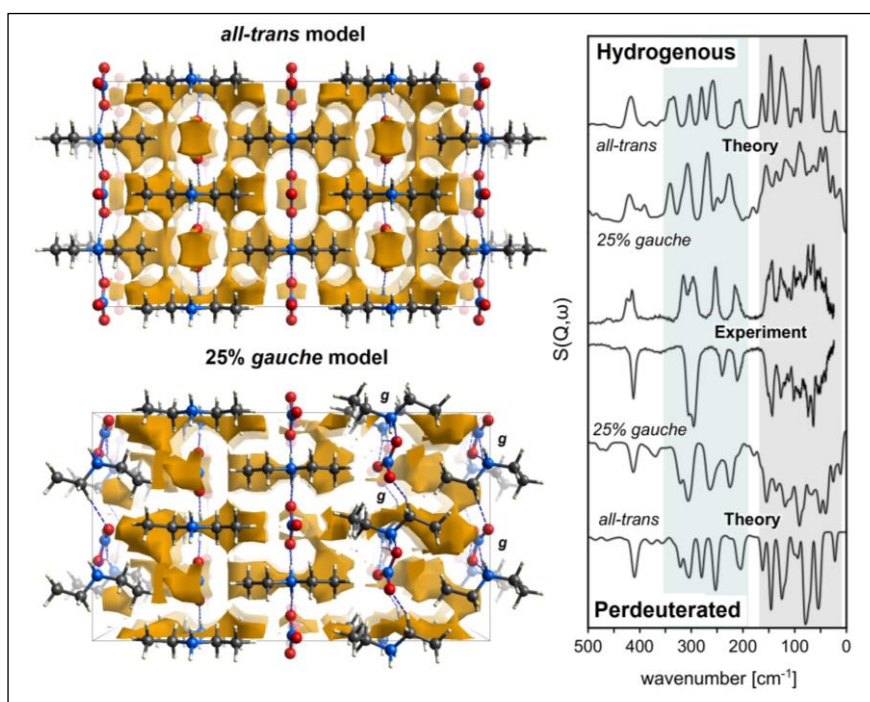
Figure 1: (Captions on the left) Two models of the crystal structure of DEAN with different extent of disorder and with crystal voids shown in brown. (Spectra on the right) Experimental and theoretical INS spectra of both hydrogenous and perdeuterated DEAN in the low-energy regime (500–24 cm^{-1}). The theoretical spectra come from phonon calculations for both considered structural models.

The archetypal diethylammonium nitrate (DEAN), $[N_{0\,0\,2\,2}][NO_3]$, and its perdeuterated analogue, $[N_{D\,D\,2\,2}][NO_3]$, were structurally characterized and studied by infrared, Raman, and inelastic neutron scattering (INS) spectroscopies. Using calculations performed on the SCARF cluster with CASTEP code and inelastic neutron scattering studies performed on TOSCA at ISIS, we reported unambiguous

spectroscopic signatures of hydrogen-bonding interactions between the two counterions.[2-3]

The first-principles calculations were performed within the framework of semi-local plane-wave DFT, and imposed Density Functional Perturbation Theory (DFPT) to predict phonon properties and optical vibrational spectra. The adopted numerical methodology has proven to be entirely adequate for a robust interpretation of the vibrational spectra in a well-defined crystal environment. The optical and neutron vibrational spectra compare very well with the experimental data for most of the assigned spectral features.

An exhaustive assignment of the spectral features observed with each technique has been provided, and a number of distinct modes related to NH⋯O dynamics have been identified. We put a particular emphasis on a detailed interpretation of the high-resolution broadband INS experiments, which allowed us to quantify a degree of disorder in solid DEAN. Such a peculiarity has been associated with *trans – gauche* conformational changes within the alkyl chains (see Figure 1). Further insight at finite-temperatures and beyond harmonic approximations were derived from AIMD simulations performed in a wide range of temperatures.

In hindsight, the wealth of experimental and computational data collected in this work can serve as a high-quality benchmark for much-needed developments of accurate classical force-fields for PILs.

References

1. I. Vázquez-Fernández, K. Druzbicki, F. Fernandez-Alonso, S. Mukhopadhyay, P. Nockemann, S.F. Parker, S. Rudić, S.-M. Stana, J. Tomkinson, D.J. Yeadon, K.R. Seddon, and N.V. Plechkova, J. Phys. Chem. C 125, 24463 (2021).

2. S. J. Clark, M. D. Segall, C. J. Pickard, P. J. Hasnip, M. J. Probert, K. Refson, M. C. Payne "First principles methods using CASTEP", Zeitschrift fuer Kristallographie, 220(5-6), 567 (2005).

3. R. S. Pinna, M. Zanetti, S. Rudić, S. F. Parker, J. Armstrong, S. P. Waller, D. Zacek, C. Smith, S. M. Harrison, G. Gorini, The TOSCA Spectrometer at ISIS: the Guide Upgrade and Beyond. J. Phys.: Conf. Ser. 1021, 012029 (2018).

Inelastic Neutron Scattering Investigation of MgCl₂ Nanoparticle-Based Ziegler-Natta Catalysts for Olefin Polymerization

Maddalena D'Amore*,[1,3] Alessandro Piovano,[1,2,3] Eleonora Vottero,[1,2,4] Andrea Piovano,[4] Svemir Rudić,[5] Alessandro Erba,[1] Elena Groppo,[1,2] and Bartolomeo Civalleri[1,2]

1. Department of Chemistry and NIS Centre, University of Turin, Via P. Giuria 7, 10125 Torino, Italy
2. INSTM, University of Turin, via G. Quarello 15/A, 101235 Torino, Italy
3. DPI, P.O. Box 902, 5600 AX Eindhoven, The Netherlands
4. Institut Laue-Langevin (ILL), 71 Avenue des Martyrs, 38042 Grenoble, France
5. ISIS Facility, Rutherford Appleton Laboratory, Chilton, Didcot, Oxfordshire, OX11 0QX, UK

The formation of nanosized and defective δ-MgCl₂ is essential for preparing performant Ziegler-Natta catalysts, and it can be achieved either by chemical or mechanical routes [1]. In this work [2], the effect of nanosize and structural disorder on the MgCl₂ support of Ziegler-Natta catalysts has been investigated in terms of induced changes to their vibrational spectroscopic fingerprint. In particular, the inelastic neutron scattering (INS) technique was used, which allowed sampling of the whole lattice dynamics support. The experimental INS spectra of several ball-milled, polycrystalline, samples of MgCl₂ were collected for the first time and compared to simulated spectra from quantum-mechanical density functional theory calculations. Theoretical calculations were performed on a variety of MgCl₂ structural models: (i) ordered and disordered bulk (3D); (ii) low-dimensional structures such as surfaces (2D) and nanorods (1D); and nanoclusters (0D). This allowed us to link specific features of the spectra to specific changes in MgCl₂ atomic structure and dynamics. In particular, the effect of translational symmetry breaking and rotational disorder is discussed. Furthermore, the present data suggest that the ball-milling process mostly leads to the formation of bulk-like crystallites rather than nanoparticles. This work ultimately highlights the combined use of INS measurements and quantum-mechanical simulations as an effective approach for the atomistic characterization of defective (nano)materials.
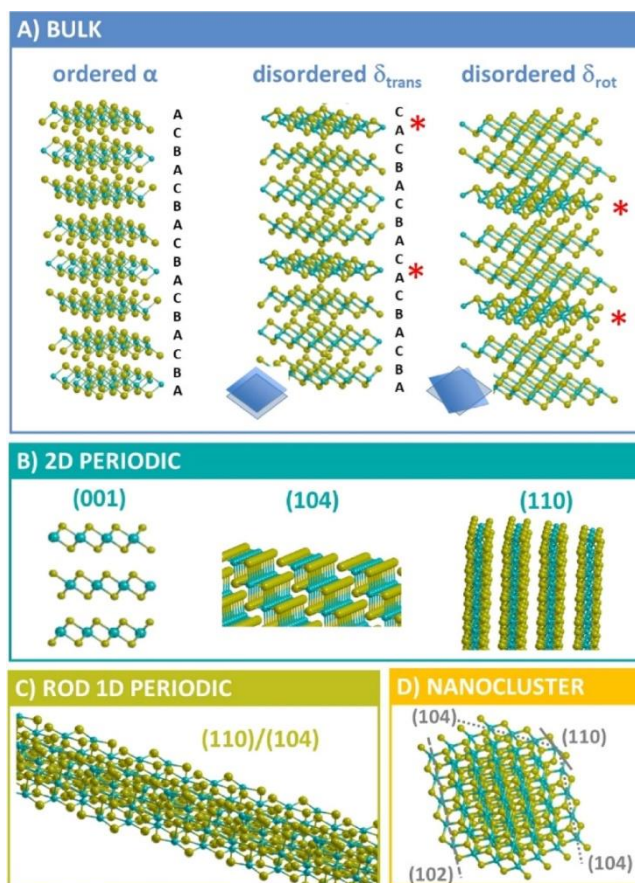
Figure 1. Ordered and disordered 3D models for MgCl2 [panel (A)] as well as low-dimensionality models ranging from 2D to 0D adopted for simulating the INS spectra. In models of disordered δ forms, the faults have been indicated by red asterisks. Panel (B) reports main surfaces of interest in catalytic processes (110) and (104), together with the basal (001) surfaces, whereas in panel (C), a polymeric model (i.e., 104/110 rod) is reported. The nanocluster in panel (D) is obtained according to the calculated Wulff polar plot. All structures represent local topologies typical of polycrystalline $MgCl_2$ adopted in Ziegler–Natta catalysis [2].

References

[1] T. Wada, G. Takasao, A. Piovano, M. D'Amore, A. Thakur, P. Chammingkwan, P. C. Bruzzese, M. Terano, B. Civalleri, S. Bordiga, E. Groppo, T. Taniike, *J. Catal.* **2020**, 385 (2020) 76-86
[2] M. D'Amore, A. Piovano, E. Vottero, A. Piovano, S. Rudić, A. Erba, E. Groppo, B. Civalleri, *ACS Appl. Nano Mater.*, **2020**, 3, 11118-11128.

Spectroscopic Fingerprints of MgCl₂/TiCl₄ Nanoclusters Determined by Machine Learning and DFT

M. D'Amore*,[1] G. Takasao,[2] H. Chikuma,[2] T. Wada,[2] T. Taniike,[2] F. Pascale,[3] A. M. Ferrari[1]

1. Department of Chemistry, University of Turin, Via P. Giuria 7, 10125 Torino, Italy
2. Graduate School of Advanced Science and Technology, Japan Advanced Institute of Science and Technology, Nomi, Ishikawa 923-1292, Japan.
3. Université de Lorraine-Nancy, CNRS, Laboratoire de Physique et Chimie Théoriques, UMR 7019, Faculté des Sciences, Vandoeuvre-les-Nancy 54500, France.

Model nanoclusters of naked $MgCl_2$ and $MgCl_2/TiCl_4$ support have been obtained by means of a nonempirical structure determination method exploiting an evolutionary algorithm. The bare $50MgCl_2$ predominantly exposes pentacoordinated sites (P) of the kind of Mg^{2+} sites typically exposed by (104), (107), (012) surfaces and isolated tetracoordinated sites (T). In the presence of $TiCl_4$, a significant increase in the fraction of T sites is found in $50MgCl_2/3TiCl_4$ system. T sites are present as isolate site but mostly as couples and close to rows of P sites.

Vibrational spectroscopy can sensitively probe the morphology and active species of $MgCl_2/ TiCl_4$. Here, we determined vibrational spectroscopic fingerprints of $50MgCl_2$ and $50MgCl_2/3TiCl_4$ which were obtained by nonempirical structure determination based on an evolutionary algorithm and DFT. The adsorption of CO, $TiCl_4$, and Ti_2Cl_8 dimers was also modelled on each of the coordinatively unsaturated Mg^{2+} sites available for binding including so-called defect sites, which are likely present at the surface of activated $MgCl_2$ nanocrystals and plausible sites for strong $TiCl_4$ species adsorption. Vibrational analysis (IR and Raman) on plausible models of $TiCl_4/ MgCl_2$ nanoclusters revealed that IR response is useful for distinguishing between the different ways of binding of $TiCl_4$ on different sites of adsorption, whereas Raman response provides a clear fingerprint of supported $TiCl_4$ species, in fact in Raman spectra, the two very intense lines of $TiCl_4$ at 465 and 485 cm^{-1}, appear as the dominant bands providing indeed an unambiguous fingerprint of the presence of the adduct. When we pass to dimer Ti_2Cl_8 on P sites again, the Raman spectrum is highly informative, which can be particularly ascribed to the Ti−Cl−Ti bridges. The features of monomeric and dimeric adducts are different in shape and are also well separated by about 10 cm^{-1}.
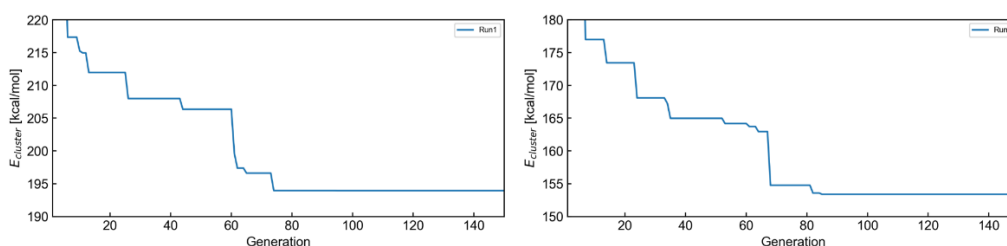
Figure 1. Evolutionary progress plot for the structure determination of naked $50MgCl_2$ (left panel) and $50MgCl_2/3TiCl_4$ (right panel). The energy of the best-of-generation individual (i.e., the most stable structure in a generation) is plotted against the generation.
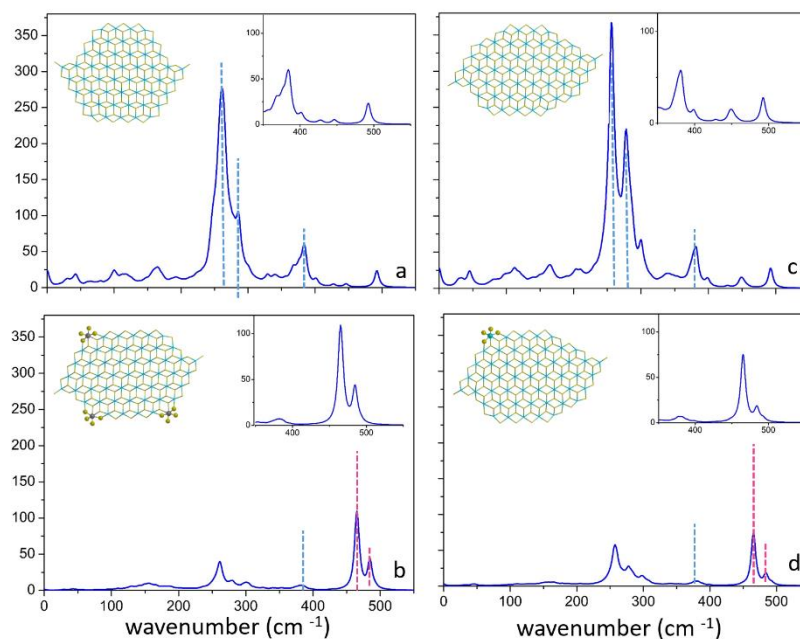
Figure 2. Simulated Raman spectra at B3LYP-D2/TZVP level of calculation of: naked 50 $MgCl_2$ cluster (panel a) and $50MgCl_2/3TiCl_4$ (i.e. 3 $TiCl_4$ molecules chemisorbed on type-B sites of the cluster) (panel b) as obtained by genetic algorithm; $50MgCl_2*$ (panel c) and $50MgCl_2*/1TiCl_4$ (i.e. one $TiCl_4$ molecule chemisorbed on type-B sites of the cluster) (panel d). Simple models of adducts are also reported: atoms belonging to the nanoplatelet and not involved in the adsorption process are represented as sticks whereas atoms of $TiCl_4$ molecules as balls; Chlorine and Titanium atoms are shown in green and dark grey, respectively.

Reference

[1] M. D'Amore, G. Takasao, H. Chikuma, T. Wada, T. Taniike, F. Pascale, A. M. Ferrari, J. Phys. Chem. C, **2021**, 125, 36, 20048–20058.

Effect of Internal Donors on Raman and IR Spectroscopic Fingerprints of MgCl$_2$/TiCl$_4$ Nanoclusters Determined by Machine Learning and DFT

M. D'Amore*,[1] T. Taniike, [2] M. Terano, [2] A. M. Ferrari[1]

1. Department of Chemistry, University of Turin, Via P. Giuria 7, 10125 Torino, Italy
2. Graduate School of Advanced Science and Technology, Japan Advanced Institute of Science and Technology, Nomi, Ishikawa 923-1292, Japan.

To fully understand the structure and properties of precatalytic nanoclusters MgCl$_2$/TiCl$_4$ in presence of Lewis bases as internal donors (ID). In this work MgCl$_2$/TiCl$_4$ nanoplatelets derived by machine learning and DFT calculations have been used to model the interaction with ethyl-benzoate EB as ID, with available exposed sites of binary Ti$_x$Cl$_y$/MgCl$_2$ systems. The influence of vicinal Ti$_2$Cl$_8$ and coadsorbed TiCl$_4$ on energetic, structural and spectroscopic behaviour of EB has been considered. The adsorption of homogeneous-like TiCl$_4$EB and TiCl$_4$(EB)$_2$ at the various surface sites have been also simulated. B3LYP-D2 and M06 functionals combined with TZVP quality basis set have been adopted for calculations. The adducts have been characterized by computing IR and Raman spectra that have been found to provide specific fingerprints useful to identify surface species; IR spectra have been successfully compared to available experimental data.

Inspection of the IR spectrum shows that the two main features are the ν(C=O) peak, sharp and narrow (its width is ~12 cm^{-1}), centred at 1678 cm^{-1} and the ν(C-O-C) vibration that leads to a group of signals in the 1275-1350 cm^{-1} range. ν(C=O) peak appears to be sensitive to the coordination number of Mg^{+2}, but scarcely affected by the chemical environment of the surface cations; therefore, the characteristic shape of the ν(C-O) signal can unambiguously probe a simultaneous presence of tetra and pentacoordinated Mg^{+2} sites. Computed IR spectra are in excellent agreement with available experimental data (see Figure 2). The homogeneous like TiCl$_4$EB and TiCl$_4$EB$_2$ complexes can easily bind at the Mg^{+2} sites of MgCl$_2$.
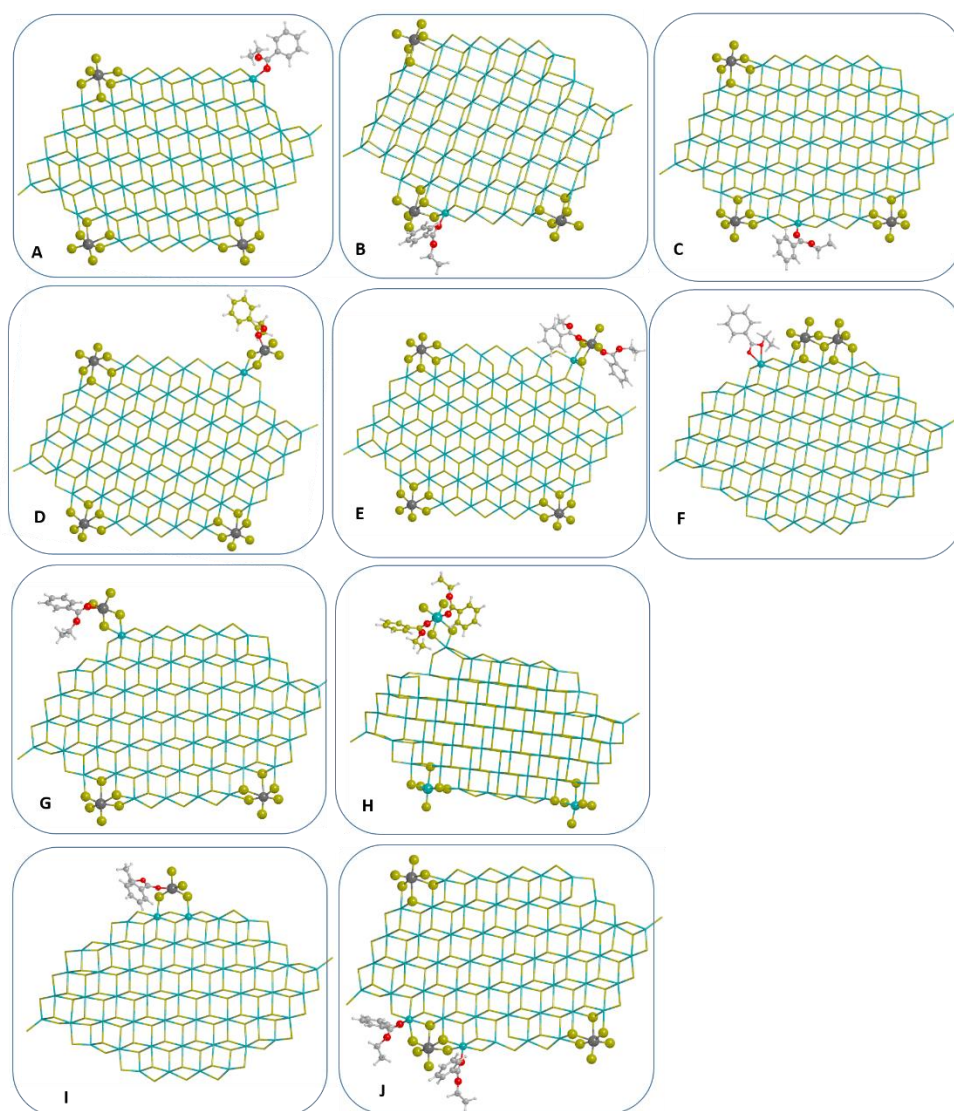
Figure 1. Coadsorption models of nanoplatelets (50MgCl$_2$/TiCl$_4$) and EB with different way of binding (A-C); models of homogeneous-like TiCl$_4$ (EB)$_x$ (x = 1, 2) complexes on the same platelet (D, E, G, H) and models obtained after the coadsorption of EB and Ti$_2$Cl$_8$ on naked MgCl$_2$ nanoplatelet (F, I). Optimizations have been performed at B3LYP-D2/TZVP level. Chlorine, Magnesium and Titanium atoms are represented in green, yellow and dark grey, respectively. All generic atoms belonging to the nanoplatelet are represented as sticks, whereas atoms of TiCl$_4$ and EB molecules and Mg atoms involved in the adsorption process are reported as balls.
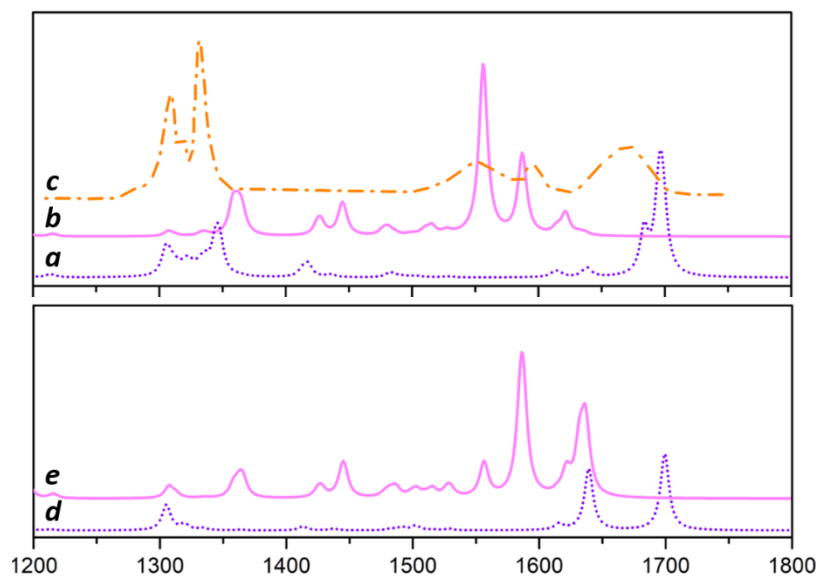
Figure 2. Sum of simulated IR intensity at B3LYP-D2/TZVP, for co-adsorption models A, B, C, F (line a) and for homogeneous-like adducts, models D, E, (line b) reported in Figure 1. Experimental IR spectrum reported in the 1200-1350 and 1550-1800 cm^{-1} spectral range (line c). Sum of simulated Raman intensity at B3LYP-D2/TZVP, for co-adsorption models A, B, C, F (line d) and for homogeneous-like adducts, models D, E (line e). The spectral region considered is 1200 - 1800 cm^{-1}, the intensities are in arbitrary units.

Reference

[1] M. D'Amore, T. Taniike, M. Terano, A. M. Ferrari, Materials, **2022**, 15 (3), 909.

Crystal Analyzers for Indirect-Geometry Broadband Neutron Spectrometers: Adding Reality to Idealized Design

M. Zanetti,[1,2] F. Masi,[2] S. Rudić,[2] J. Armstrong,[2] S.F. Parker,[2] F. Fernandez-Alonso,[3,6,7] and G. Gorini[4,5]

1. Consiglio Nazionale delle Ricerche, Dipartimento di Scienze Fisiche e Tecnologie della Materia, Roma, 00185 Italia
2. ISIS Facility, Rutherford Appleton Laboratory, Chilton, Didcot, Oxfordshire, OX11 0QX United Kingdom
3. Department of Physics and Astronomy, University College London, London, WC1E 6BT United Kingdom
4. Universitá degli Studi di Milano-Bicocca, Milano, 20126 Italia
5. Istituto di Fisica del Plasma "P. Caldirola," Consiglio Nazionale delle Ricerche, Milano, 20125 Italia
6. Materials Physics Center, CSIC-UPV/EHU, Donostia–San Sebastian, 20018 Spain
7. IKERBASQUE, Basque Foundation for Science, Bilbao, 48013 Spain

The recent trend to fully utilize neutrons from pulsed spallation sources for broadband neutron spectrometers with indirect-geometry seeks to improve their performance by using large-area curved analyzers that focus neutrons in time, energy and space. Here we describe ongoing collaborative efforts towards future upgrades of TOSCA at ISIS, which are also essential for the design and subsequent construction of VESPA at the ESS. This performance improvement is due to both a larger detector coverage using a curved geometry and a corresponding tuning of analyzer crystal characteristics. To achieve high resolution in the entire spectral range 0–500 meV, the time-focusing of neutrons from the sample to the detector should be carried out within tight tolerances. The effect of graphite mosaicity and its variation from crystal-to-crystal across the whole analyzer, as well as the impact of manufacturing tolerances on instrument performance, and of the detector pixelation were investigated to inform about the design in order to balance the efficiency of neutron collection with the resolution requirements.
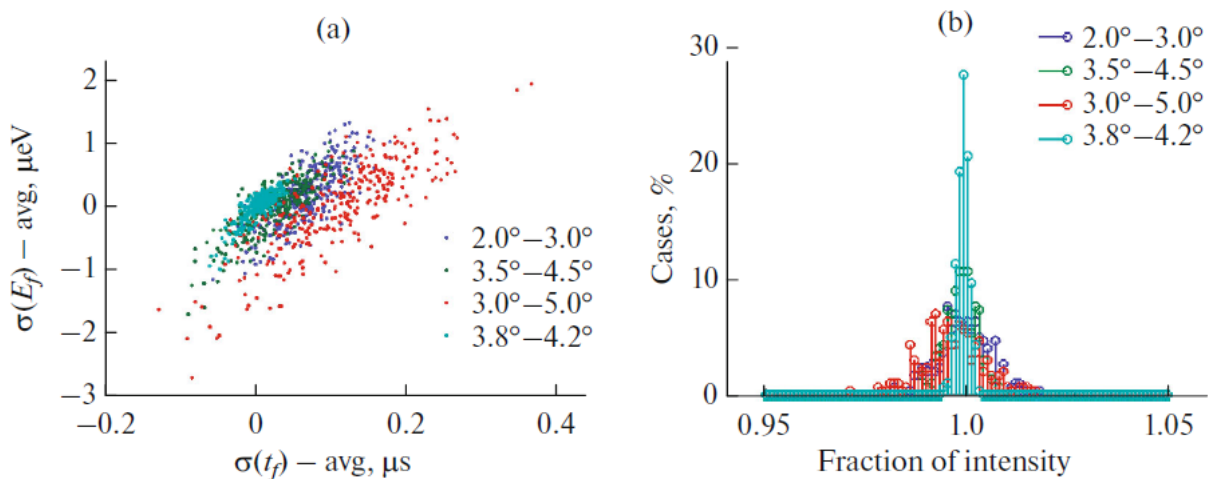
Figure 1. Figures of merit for 300 random configurations for each mosaicity range: (a) dispersion of uncertainties relative to the ideal case; (b) intensity fraction with respect to the ideal case.

The extensive neutron-transport simulations performed on the SCARF cluster required very high statistics in order to generate high-quality results. Depending on the case, we used up to 40 cores for

up to 160 hours (300 x 16 = 4800 simulations, each one lasting on average 2 minutes). SCARF was essential to these simulations because the physical processes involved are manifold and difficult to disentangle without recourse to detailed simulations, i.e., neutron moderation, reflection in the neutron guides, scattering processes and Bragg diffraction onto the analyser.

Reference

1. M. Zanetti, F. Masi, S. Rudić, J. Armstrong, S.F. Parker, F. Fernandez-Alonso, G. Gorini, Journal of Surface Investigation: X-ray, Synchrotron and Neutron Techniques 14, S242 (2020).

Investigation of non-neutral electron plasmas confined in a Penning-Malmberg trap

Titus-Stefan Dascalu

Imperial College London

LhARA (The Laser-hybrid Accelerator for Radiobiological Applications) [1] is a novel concept facility that aims to provide uniquely flexible proton and ion beams for the study of radiobiology. The hybrid approach is based on a laser to drive the creation of a high flux of protons or light ions that are captured using a plasma (Gabor) lens [2] and formed into a beam. The laser-driven source together with the high-transmission capture system allow a high instantaneous dose-rate to be delivered and, thus, the study of a new regimen of particle-beam therapy.

A plasma lens represents a cost-effective alternative to conventional solenoids for laser driven proton and ion beams. Such beams have large divergence and large energy spread at the source and require a strong-focusing element to efficiently capture the particles. However, an ideal lens requires a high-density plasma ($\sim 10^{15}$ m^{-3}) for short focal lengths and a uniform electron cloud confined in a volume larger than that occupied by plasmas in conventional Penning-Malmberg traps. The high electron density, large plasma length and the proximity of the plasma to the conducting walls of the trap may lead to plasma instabilities. These instabilities need to be identified and supressed for the lens to act as an efficient beam-focusing device.

With SCARF support we have been able to investigate the behaviour of the electron plasmas in a few different trap configurations and over a variety of plasma parameters. We use SCARF resources and the three-dimensional particle-in-cell (PIC) code VSim [3] to run computationally intensive simulations of the confinement of non-neutral electron plasmas. At the high electron density of interest, PIC simulations require a fine mesh and the simultaneous tracking of more than 10^7 macroparticles. Running a simulation in parallel on multiple SCARF nodes decreases the total duration of one simulation and allowed us to run tens of simulations that were critical in our investigations. For example, we have been able to identify a particular plasma instability (Figure 1) as the cause for the anomalous beam focusing observed in a beam test of a first Gabor lens prototype [4] built for LhARA. Further work is ongoing on SCARF to validate predictions from PIC simulations against a different experiment with trapped electrons.
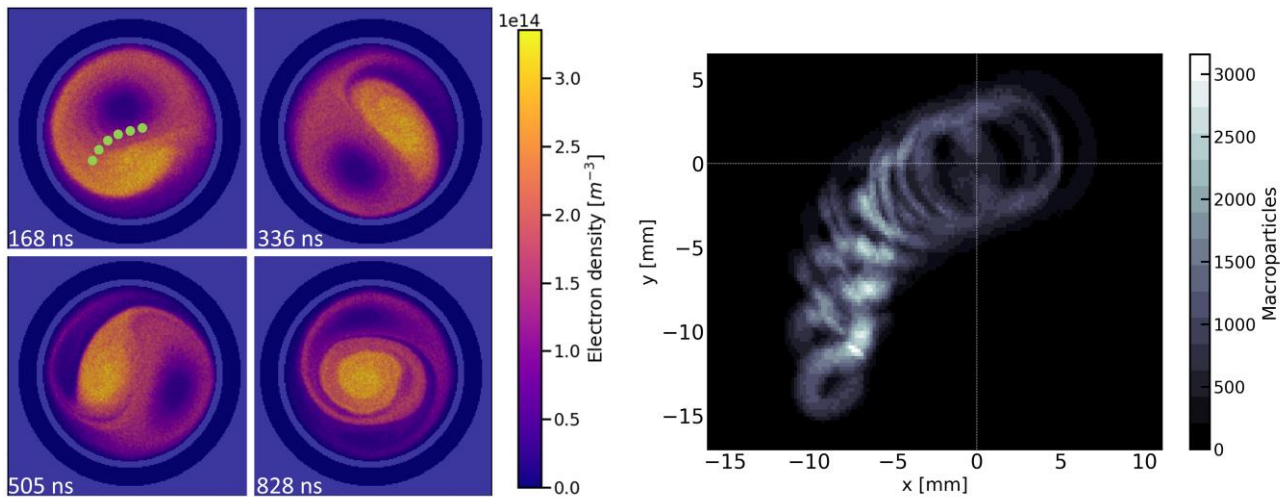
Figure 1: PIC simulation of a plasma instability that was observed to focus the proton pencil beams into rings. Left: the averaged density of plasma in a transverse cross-section through the lens at four different time steps during the evolution of the instability. The green spots mark the entry position of proton pencil beams. Right: number of macroparticles hitting a screen 67 cm downstream of the lens

References
[1] Aymar, G., Becker, T., Boogert, S., Borghesi, M., Bingham, R., Brenner, C., Burrows, P.N., Ettlinger, O.C., Dascalu, T., Gibson, S. and Greenshaw, T., 2020. LhARA: the laser-hybrid accelerator for radiobiological applications. *Frontiers in Physics*, p.432. https://doi.org/10.3389/fphy.2020.567738
[2] Gabor, D. A Space-Charge Lens for the Focusing of Ion Beams. *Nature* **160,** 89–90 (1947). https://doi.org/10.1038/160089b0
[3] VSim: an electromagnetics and plasma computational application. https://www.txcorp.com/vsim
[4] Nonnenmacher, T.; Dascalu, T.-S.; Bingham, R.; Cheung, C.L.; Lau, H.-T.; Long, K.; Pozimski, J.; Whyte, C. Anomalous Beam Transport through Gabor (Plasma) Lens Prototype. *Appl. Sci.* **2021**, *11*, 4357. https://doi.org/10.3390/app11104357

Muons found to be faithful probes of exotic superconductors

Professor Tom Lancaster
Department of Physics
Durham University
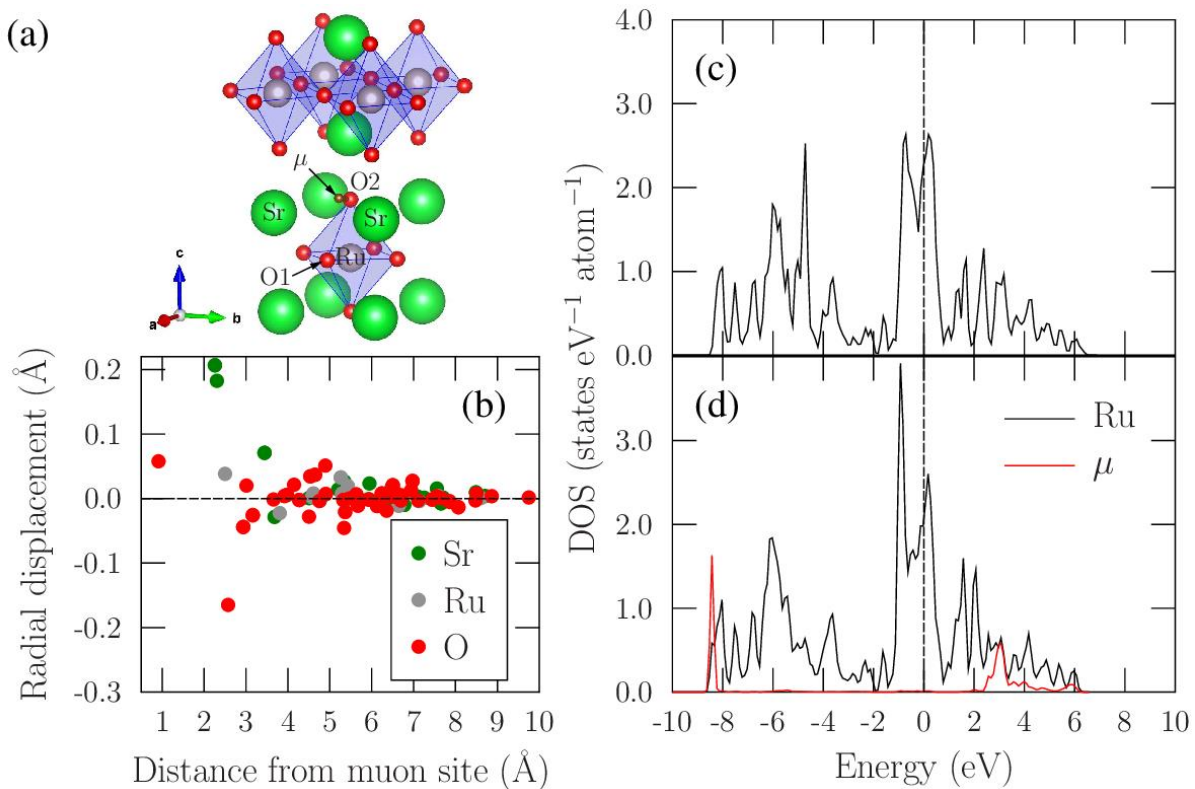
Researchers in the Centre for Materials Physics have demonstrated that spontaneous magnetic fields, detected by implanting sub-atomic muons in superconducting materials, are likely to be intrinsic to an exotic, time-reversal symmetry broken, superconducting state.

Owing to the Meissner effect, the expulsion of magnetic fields from a superconductor, it is often claimed that superconductivity and magnetism are antagonistic states of matter. However, there are a growing number of systems for which small internal magnetic fields have been detected in the superconducting state. These fields are signatures of time-reversal symmetry breaking (TRSB), a symmetry that is preserved in the case of conventional superconductors described by Bardeen-Cooper-Schrieffer (BCS) theory, which describes the superconducting state as a condensate of pairs of electrons called 'Cooper pairs'. The presence of TRSB implies the occurrence of superconductivity with exotic symmetries and the possibility of novel electron-pairing mechanisms. However, in most cases, TRSB has been observed only using implanted muons.

Muons, subatomic charged particles that are produced in particle accelerators, are extremely sensitive probes of magnetism and thus ideally suited to detecting these small internal magnetic fields. However, a common concern regarding the muon spectroscopy technique is whether the degree to which the implanted muon perturbs the system which it aims to measure, and one might therefore question whether these internal magnetic fields are not intrinsic to the sample under study but are instead a result of a muon-induced effect.

In a recent collaboration between Durham University researchers Ben Huddart, Tom Lancaster and Stewart Clark and researchers at Oxford University and the University of Parma, a systematic study of the muon stopping states in a series of superconducting materials that exhibit time-reversal symmetry breaking was carried out. This was achieved by calculating muon stopping sites using density functional theory (a procedure known as DFT+μ), which is a recent method developed by many of the authors of this study. They show that in a wide range of systems, which included the widely studied unconventional superconductor Sr_2RuO_4 (shown in the figure), any structural or electronic distortions caused by the muon are very small and are unlikely to lead to the generation of local magnetic fields. These results strongly suggest that the spontaneous magnetic fields observed in previous muon-spin spectroscopy experiments are not artefacts due to the presence of a muon, but instead reflect the time-reversal symmetry breaking present in the superconducting state.

The results of this study have been published in Physical Review Letters.

"Intrinsic Nature of Spontaneous Magnetic Fields in Superconductors with Time-Reversal Symmetry Breaking", B. M. Huddart, I. J. Onuorah, M. M. Isah, P. Bonfà, S. J. Blundell, S. J. Clark, R. De Renzi, and T. Lancaster, Phys. Rev. Lett. **127**, 237002 (2021).

https://doi.org/10.1103/PhysRevLett.127.237002

Computational modelling of biological membrane systems

Valeria Losasso, Martyn Winn

Scientific Computing Department, STFC Daresbury Laboratory, Keckwick Lane, Daresbury

The SCARF cluster has been used for a variety of projects, in collaboration with multiple people and institutions, involving molecular dynamics (MD) simulations of biological membranes in different conditions, with different goals. Where the bulk of the calculations has been performed on dedicated resources elsewhere (Hartree, Archer), SCARF has been extensively used for extending simulations, post-processing and data analysis.

The one among these which has formally ended has been just published on Biophysical Journal[1]. Here, in collaboration with Unilever and IBM at Hartree, we show that small molecule additives enhance the potency of antimicrobial peptides (AMP), key components of the human immune system. We simulated POPG and POPC as mimics of bacterial and mammalian membranes, respectively, in complex with the AMP LL-37 and niacinamide derivatives (Fig. 1), and showed that there is a clear synergistic effect between LL-37 and niacinamide in terms of altering the physical properties of the membrane, ultimately leading to the membrane disruption, and that this effect is specific to bacterial membranes.
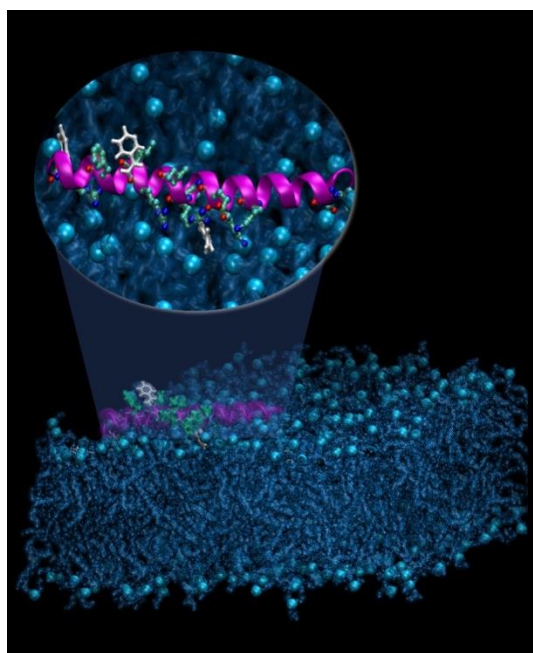
Fig. 1. POPG bilayer (blue) in complex with LL-37 (pink cartoon) and niacinamide (white sticks).

Other projects are still ongoing and include:

1) A study, in collaboration with F. Martelli (IBM/Hartree), on the mutual interactions between water and biological membrane through the inspection of the hydrogen bond network in water[2]. The systems studied here are composed of several hundred thousand atoms (Fig. 2a). These sizes are necessary to analyse multiple layers of water at varying distances from the membrane, however make the simulations computationally expensive, requiring running jobs on multiple SCARF nodes.

2) A study, in collaboration with A. Hughes (ISIS), the use of MD simulations in the analysis of neutron reflectometry data from membranes[3]. In this approach, MD trajectories are converted into atomic number densities (Fig. 2b) and finally, from the latter, to scattered length densities (SLD), used to fit the measured data. Current studies are based on membrane monolayers (Fig. 2c).
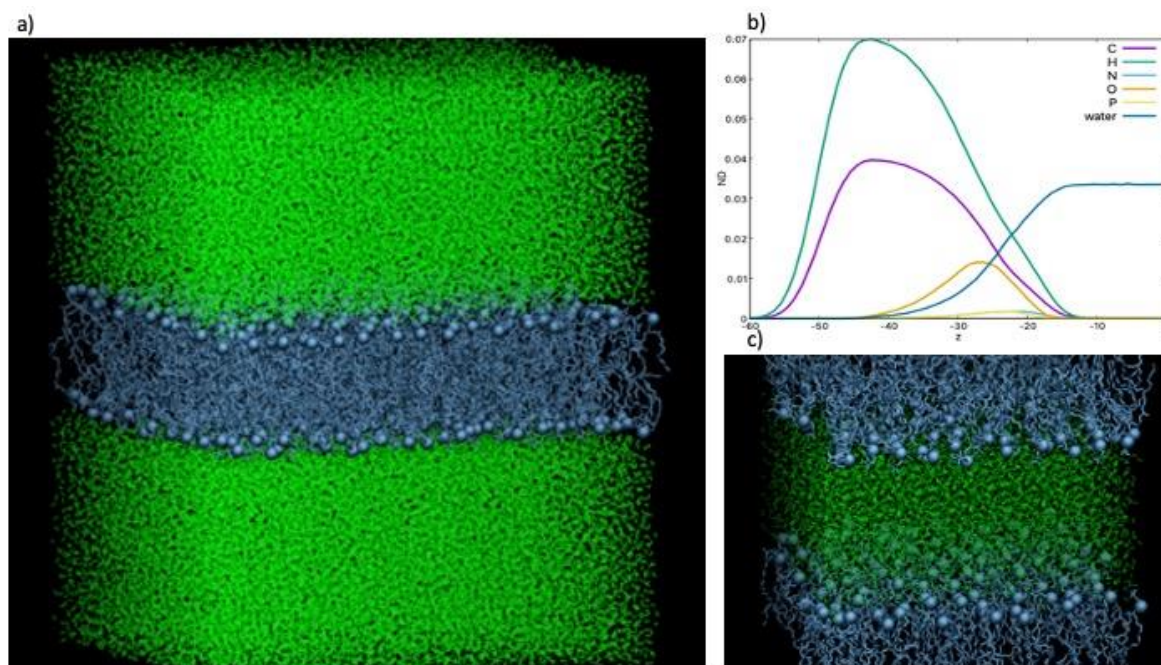
Fig 2. a) DLPC/DLPG bilayer with a 60 Å water layer on each side. b) Atomic number density profile for a simulation of a DSPC monolayer. c) DSPC monolayer (two replicas in the system). Lipids are represented in blue sticks, headgroups in blue spheres, water in green.

References

1. Losasso V., Agarwal K., Waskar M., Majumdar A., Crain J., Winn M., Hoptroff M. Small molecules enhance the potency of natural antimicrobial peptides. *Biophys. J.* 121(3):491-501, 2022.
2. Martelli F., Crain J. and Franzese G. Network Topology in Water Nanoconfined between Phospholipid Membranes. *ACS Nano* 14(7):8616-8623, 2020.
3. A.V. Hughes et al. On the interpretation of reflectivity data from lipid bilayers in terms of molecular-dynamics models. *Acta Cryst.* D72:1227-1240, 2016.

4. APPENDIX A1: SCARF HARDWARE DETAILS – CPU NODES

Host group	CPU	Nodes	Cores /node	Total cores	Interconnect	Total mem (GB)
SCARF 21	AMD EPYC 7502	168	32	5376	HDR Infiniband	43008
SCARF 20	AMD EPYC 7502	78	32	2560	EDR Infiniband	21504
SCARF 19	Intel Xeon Gold 6126	16	24	384	EDR Infiniband	3072
SCARF 18	Intel Xeon Gold 6126	148	24	3552	EDR Infiniband	28416
SCARF 17/ DeRevolutionIbus	Intel E5-2650 v4	201	24	4824	EDR Infiniband	5728
SCARF 16/ MagnaCarta/ IBIS	Intel E5-2650 v3	20	20	400	FDR Infiniband	2560
SCARF 15	Intel E5-2650 v3	68	20	1360	FDR Infiniband	8704
Total		**699**		**16,156**		**112,992**

5. APPENDIX A2: SCARF HARDWARE DETAILS – GPU NODES

Host group	CPU	GPU	Nodes	Cores /node	Total cores	Interconnect
SCARF 21	AMD 7302	NVIDIA A100x4	6	32	192	HDR Infiniband
GPU13	Intel E5-2650v2	NVIDIA K40x2	12	8	86	FDR Infiniband

6. APPENDIX B: PUBLICATIONS AND PRESENTATIONS

Publications

	Title	Authors	Journal
1	Ab initio study of structural, elastic and thermodynamic properties of Fe3S at high pressure: Implications for planetary cores.	K. Valencia, A. de Moya, G. Morard, N. L. Allan and C. Pinilla	American Mineralogist, 107, 248-256 (2022)
2	Enhanced spin-orbit coupling in heavy metals via molecular coupling	S. Alotibi, B. J. Hickey, G. Teobaldi, M. Ali, J. Barker, E. Poli, D. D. O'Regan, Q. Ramasse, G. Burnell, J. Patchett, C. Ciccarelli, M. Alyami, T. Moorsom, and O. Cespedes	ACS Applied Materials Interfaces (2021) 13 4, 5228-5234. DOI: 10.1021/acsami.0c19403
3	Observation of a molecular muonium polaron and its application to probing magnetic, dynamic and electronic states.	M. Rogers, T. Prokscha, G. Teobaldi, L. Liborio, S. Sturniolo, E. Poli, D. Jochym, R. Stewart, M. Flokstra, S. Lee, T. Moorsom and O. Cespedes	PRB 104, 064429. DOI:http://dx.doi.org/10.1103/PhysRevB.104.064429.
4	π-anisotropy: A nanocarbon route to hard magnetism.	T. Moorsom, S. Alghamdi, S. Stansill, E. Poli, G. Teobaldi, M. Beg, H. Fangohr, M. Rogers, Z. Aslam, M. Ali, B. J. Hickey, & O. Cespedes	Phys. Rev. B (2020) 101, 060408(R)
5	Entropy-based active learning of graph neural network surrogate models for materials properties	J Allotey, KT Butler, J Thiyagalingam	*The Journal of Chemical Physics* 155 (17), 174116, 2021
6	Interpretable, calibrated neural networks for analysis and understanding of inelastic neutron scattering data	KT Butler, MD Le, J Thiyagalingam, TG Perring	*Journal of Physics: Condensed Matter* 33 (19), 194006, 2021
7	Computational prediction of muon stopping sites: a novel take on the unperturbed electrostatic potential method	S. Sturniolo1, L. Liborio1	J. Chem. Phys. 153, 044111 (2020)
8	A Muon Spectroscopic and Computational Study of the Microscopic Electronic Structure in Thermoelectric Hybrid Silicon Nanostructures	S. Sturniolo1, L. Liborio1 et. al.	J. Phys. Chem. C 2020, 124, 9656−9664

9	Observation of a molecular muonium polaron and its application to probing magnetic and electronic states	S. Sturniolo1, L. Liborio1, E. Poli1, G. Teobaldi1, D. Jochym1 et. al.	PHYSICAL REVIEW B 104, 064429 (2021)
10	The Origin of Magnetic Ordering in a Structurally-Perfect Quantum Kagome Antiferromagnet	T. Arh, P. Prelovšek, M. Pregelj, M. Klanjšek, A. Ozarowski, S. J. Clark, T. Lancaster, W. Sun, J.-X. Mi and A. Zorko	Phys. Rev. Lett. 125, 027203 (2020).
11	Signature of a randomness-driven spin-liquid state in a frustrated magnet	J. Khatua, M. Gomilšek, J. C. Orain, A. M. Strydom, Z. Jagličić, C. V. Colin, S. Petit, A. Ozarowski, L. Mangin-Thro, K. Sethupathi, M.S. Ramachandra Rao, A. Zorko and P. Khuntia	To appear in Comm. Phys. (2022).
12	The Origin of Magnetic Ordering in a Structurally-Perfect Quantum Kagome Antiferromagnet, Phys. Rev. Lett. 125, 027203 (2020).	T. Arh, P. Prelovšek, M. Pregelj, M. Klanjšek, A. Ozarowski, S. J. Clark, T. Lancaster, W. Sun, J.-X. Mi and A. Zorko	Phys. Rev. Lett. 125, 027203 (2020).
13	Vibrational Dynamics of Crystalline 4-Phenylbenzaldehyde from INS Spectra and Periodic DFT Calculations	Mariela M. Nolasco, Catarina F. Araujo, Pedro D. Vaz, Ana M. Amado, Paulo Ribeiro-Claro	Molecules, 25 (2020) 1374. DOI: 10.3390/molecules25061374
14	New Insights on the Vibrational Dynamics of 2-Methoxy-, 4-Methoxy- and 4-Ethoxy-Benzaldehyde from INS Spectra and Periodic DFT Calculations,	Paulo J. A. Ribeiro-Claro, Pedro D. Vaz, Mariela M. Nolasco, Francisco P. S. C. Gil, Luís A. E. Batista de Carvalho, Maria Paula M. Marques, Ana M. Amado	Materials, 14 (2021) 4561. DOI: 10.3390/ma14164561
15	Exploiting the flexibility of the pyrochlore composition for acid-resilient iridium oxide electrocatalysts in proton exchange membranes	D.L. Burnett, E. Petrucco, R.J. Kashtiban, S.F. Parker, J.D.B. Sharman and R.I. Walton	Journal of Materials Chemistry A (2021) [doi: 10.1039/D1TA05457K] Gold OA
16	Spectroscopic signatures of hydrogen-bonding motifs in protonic ionic liquids	I. Vazquez-Fernandez, K. Druzbicki, F. Fernandez-Alonso, S. Mukhopadhyay, P. Nockemann, S.F. Parker, S. Rudić, S.-M. Stana, J. Tomkinson, D. Yeadon, K. Seddon and N. Plechkova	Journal of Physical Chemistry C 125 (2021) 24463–24476 doi: 10.1021/acs.jpcc.1c05137] Gold OA

17	Structure and spectroscopy of methionyl-methionine for aquaculture	S.F. Parker, N.P. Funnell, K. Shankland, E. Kabova, T. Häußner, H.-J. Hasselbach, S. Braune, C. Kobler and P.W. Albers	Scientific Reports 11 (2021) 458 [doi: 10.1038/s41598-020-80385-z] Gold OA
18	Crystal analyzers for indirect-geometry broadband neutron spectrometers: adding reality to idealized design	M. Zanetti, F. Masi, S. Rudić, J. Armstrong, S.F. Parker, F. Fernandez-Alonso and G. Gorini	Journal of Surface Investigation: X-ray, Synchrotron and Neutron Techniques 14 (2020) S242–S250 [doi: 10.1134/S1027451020070526] Green OA
19	The structure and vibrational spectroscopy of cryolite, Na3AlF6	S.F. Parker, A.J. Ramirez-Cuesta and L.L. Daemen	Royal Society Open Science 7 (2020) 200776 [doi: 10.1098/rsos.200776]. Gold OA
20	Structure and vibrational spectroscopy of lithium and potassium methanesulfonates	S.F. Parker, E.J. Revill-Hivet, D.W. Nye and M.J. Gutmann	Royal Society Open Science 7 (2020) 200776 [doi: 10.1098/rsos.200776]. Gold OA
21	Computational and spectroscopic studies of carbon disulfide	I.B. Adilina, F. Aulia, M.A. Fitriady, F. Oemry, R.R. Widjaya and S.F. Parker	Molecules 25 (2020) 1271. [doi: 10.3390/molecules25061271] Gold OA
22	Structure and dynamics of the superprotonic conductor caesium hydrogen sulfate, CsHSO4	S.F. Parker, H Cavaye and S.K. Callear	Molecules 25 (2020) 1271. [doi: 10.3390/molecules25061271] Gold OA
23	The methyl torsion in unsaturated compounds	A. Zachariou, A.P. Hawkins, P. Collier, R.F. Howe, D. Lennon and S.F. Parker	ACS Omega 5 (2020) 2755-2765 [doi: 10.1021/acsomega.9b03351]. Gold OA
24	Substrate–Solvent Crosstalk—Effects on Reaction Kinetics and Product Selectivity in Olefin Oxidation Catalysis	Rita N. Sales, Samantha K. Callear, Pedro D. Vaz, Carla D. Nunes	Chemistry, 3 (2021) 753–764. DOI: 10.3390/chemistry3030054
25	Improved fast electron transport through the use of foam guides	R. A. B. Alraddadi, A. P. L. Robinson and N. C. Woolsey	Phys. Plasmas, 27, 092701 (2020).
26	Spectroscopic Signatures of Hydrogen-Bonding Motifs in Protonic Ionic Liquid Systems: Insights from Diethylammonium Nitrate in the Solid State	1. I. Vázquez-Fernández, K. Drużbicki, F. Fernandez-Alonso, S. Mukhopadhyay, P. Nockemann), S. F. Parker, S. Rudić, S. Stana J. Tomkinson, D. J.	. Phys. Chem C 125, 44, 24463-24476 (2021). doi:10.1021/acs.jpcc.1c05137

		Yeadon, K. R. Seddon. N. V. Plechkova	
27	Phonons and oxygen diffusion in Bi_2O_3 and $(Bi_{0.7}Y_{0.3})_2O_3$	2. P. Goel, M. Gupta, R. Mittal, S. Skinner, S. Mukhopadhyay, S. Rols, S. Chaplot. J	Phys. Cond. Mat 32, 334002 (2020). https://doi.org/10.1088/1361-648X/ab88f8
28	Identification of normal modes responsible for ferroelectric properties in organic ferroelectric CBDC	S Mukhopadhyay	Journal of Physics Communications 3, 113001 (2019): doi:10.1088/2399-6528/ab5431
29	Adsorbed States of Hydrogen on Platinum: A New Perspective	S. F Parker, S Mukhopadhyay, M. J Jiménez-Ruiz, P. W Albers	Chem Eur J 25, 6496 (2019). doi:10.1002/chem.201900351
30	Characterization of the surface species on carbon supported Pd and Pt catalysts	S. F Parker, S Mukhopadhyay, M. J Jiménez-Ruiz, P. W Albers	Abs Pap Am Chem Soc 257 (2019): 79. Is in proceedings of: National Meeting of the American Chemical Society, 31 Mar - 4 Apr, Orlando, Florida, US (2019).
31	Finger print vibrations of ferroelectricity in organic ferroelectrics for energy applications	S. Mukhopadhyay	14th International conference on materials chemistry (MC14), 8 - 11 July Birmingham, UK (2019).
32	Structure property correlations and finger-prints of ferroelectricity in organic ferroelectrics	S. Mukhopadhyay	Materials and Molecular Modelling Hub, 31st May, University College London (2019).
33	Spectroscopic signatures of hydrogen-bonding motifs in protonic ionic-liquids systems: insights from diethylammonium nitrate in the solid state,	I. Vázquez-Fernández, K. Druzbicki, F. Fernandez-Alonso, S. Mukhopadhyay, P. Nockemann, S.F. Parker, S. Rudić, S.-M. Stana, J. Tomkinson, D.J. Yeadon, K.R. Seddon, and N.V. Plechkova	J. Phys. Chem. C 125, 24463 (2021).
34	Inelastic neutron scattering investigation of $MgCl_2$ nanoparticle-based Ziegler Natta catalysts for olefin polymerization	M. D'Amore*, A. Piovano, E. Vottero, A. Piovano, S. Rudic, A. Erba, E. Groppo, B. Civalleri	*ACS Applied Nano Materials*, 2020, 3 (11), 11118-111128.
35	Spectroscopic Fingerprints of $MgCl_2/TiCl_4$ Nanoclusters Determined by Machine Learning and DFT	M. D'Amore*, G. Takasao, H. Chikuma, T. Wada, T. Taniike, F. Pascale, A. M. Ferrari	*Journal of Physical Chemistry C,* 2021, 125, 36, 20048–20058.
36	Effect of Internal Donors on Raman and IR Spectroscopic Fingerprints of	M. D'Amore*, T. Taniike, M. Terano, A. M. Ferrari	Materials, 2022, 15 (3), 909.

	$MgCl_2/TiCl_4$ Nanoclusters Determined by Machine Learning and DFT		
37	Crystal analysers for indirect-geometry broadband neutron spectrometers: adding reality to idealised design	M. Zanetti, F. Masi, S. Rudić, J. Armstrong, S.F. Parker, F. Fernandez-Alonso, G. Gorini	Journal of Surface Investigation: X-ray, Synchrotron and Neutron Techniques 14, S242 (2020).
38	Anomalous Beam Transport through Gabor (Plasma) Lens Prototype.	Nonnenmacher, T.; Dascalu, T.-S.; Bingham, R.; Cheung, C.L.; Lau, H.-T.; Long, K.; Pozimski, J.; Whyte, C	*Appl. Sci.* 2021, *11*, 4357. https://doi.org/10.3390/app1104357
39	Second Beam Test and Numerical Investigation of the Imperial College Plasma (Gabor) Lens Prototype	Dascalu, T.-S. et al.	Proc. IPAC'21, Campinas, SP, Brazil, May 2021, pp. 2943-2946. doi:10.18429/JACoW-IPAC2021-WEPAB140
40	Intrinsic Nature of Spontaneous Magnetic Fields in Superconductors with Time-Reversal Symmetry Breaking	B. M. Huddart, I. J. Onuorah, M. M. Isah, P. Bonfà, S. J. Blundell, S. J. Clark, R. De Renzi, and T. Lancaster	Phys. Rev. Lett. 127, 237002 (2021). https://doi.org/10.1103/PhysRevLett.127.237002

Presentations

	Conference	Title	Presenter
1	Goldschmidt conference 2021, Lyon, France.	First-Principles Investigation of Equilibrium Iron Isotope Fractionation in Fe1-xSx Alloys at Earth's Core Formation Conditions.	C. Pinilla. doi: 10.7185/gold2021.5379
2	EMRS 2021 Fall meeting	Modern computational Methods and their applications In materials science	Dr Ivan Scivetti https://www.youtube.com/watch?v=dogqL5DH5nk&list=PLFEB3YHuxu13XIcvx9Klld-a3LO3B0UWp
3	ACS Fall 2021, MRS Fall 2021	Accelerating Atomisitic Simulations with Machine Learning	KT Butler
5	Innovative Inelastic Neutron Scattering 2021, AI4SD Conferences 2022	Machine learning for understanding neutron scattering	KT Butler
7	2020 Edition Muon Site Calculation Meeting (Virtual Edition) Friday 4th September, 2020	SCARF related work	S. Sturniolo, L. Liborio
8	Muon Jamboree! 13-16 December 2021	SCARF related work	S. Sturniolo, L. Liborio
9	2021 Galaxy Community Conference, 28 June 10 July	SCARF related work	S. Sturniolo, L. Liborio
10	CMP seminar at Durham University, 22nd July 2020	Quantum effects in muon spin spectroscopy	M. Gomilšek
11	Muon Site Calculation Meeting, 4th September 2020	Quantum effects at muon stopping sites	M. Gomilšek
12	Faculty of Mathematics and Physics, University of Ljubljana, 12th October 2020, Ljubljana, Slovenia	Quantum motion of muons	M. Gomilšek
13	VII Italian Conference on Magnetism (Magnet2021)	Online Poster Presentation: Spin States and magnetic interactions in isolated CoO4 tetrahedra of Ba_2CoO_4 from first principles.	Ifeanyi John Onuorah, Pietro Bonfà, Muhammad Maikudi Isah, Roberto De Renzi
14	16th direct drive fast ignition workshop (Virtual meeting) ELI Beamline, Czech Republic (24/03/2021)	Oral Presentation	R. A. B. Alraddadi[1], A. P. L. Robinson[2] and N. C. Woolsey[3].

15	Christmas CLF High Power Laser Science Community Meeting (Virtual meeting), Guildhall, Abingdon, Oxfordshire, United Kingdom (09/02/2021)	Oral Presentation	R. A. B. Alraddadi[1], A. P. L. Robinson[2] and N. C. Woolsey[3].
16	National Meeting of the American Chemical Society, 31 Mar - 4 Apr, Orlando, Florida, US (2019).	Characterization of the surface species on carbon supported Pd and Pt catalysts	S. F Parker, S Mukhopadhyay, M. J Jiménez-Ruiz, P. W Albers
17	14th International conference on materials chemistry (MC14), 8 - 11 July Birmingham, UK (2019)	Fingerprint vibrations of ferroelectricity in organic ferroelectrics for energy applications	S. Mukhopadhyay
18	Materials and Molecular Modelling Hub, 31st May, University College London (2019).	Structure property correlations and finger-prints of ferroelectricity in organic ferroelectrics	S. Mukhopadhyay
19	26-28 September 2021, *1st International Conference on Computational and Applied Physics (ICCAP2021),* Blida (Algeria).	Understanding structure and properties of $MgCl_2$ supported Ziegler Natta nanoclusters by DFT, spectroscopy and machine learning. How modelling uncovers the origin of industrial catalysis	Maddalena D'Amore, Gentoku Takasao, Hiroki Chikuma, Toru Wada, Toshiaki Taniike, Fabien Pascale, and Anna Maria Ferrari
20	April 18-20 2022, *Materials Science & Engineering,* Boston (USA)	Revisiting the identity of δ-$MgCl2$: structure and properties of nanoclusters by DFT, spectroscopy and machine learning. How modelling uncovers the origin of industrial catalysis	Maddalena D'Amore, G. Takasao, T. Wada, T. Taniike, A. Piovano, P. C. Bruzzese, P. Chammingkwan, F. Pascale, E. Groppo, B. Civalleri, M. Terano, S. Bordiga, A. M. Ferrari
	CATCHEM, June 20-21, 2022 Berlin (Germany)	Revisiting the identity of δ-$MgCl_2$: structure and properties of nanoclusters by DFT, spectroscopy and machine learning. How modelling uncovers the origin of industrial catalysis	Maddalena D'Amore, G. Takasao, H. Chikuma, T. Wada, T. Taniike*, A. Piovano, P. C. Bruzzese, P. Chammingkwan, F. Pascale, E. Groppo, B. Civalleri, M. Terano, S. Bordiga, A. M. Ferrari
	IPAC'21, Campinas, SP, Brazil, May 2021	Second Beam Test and Numerical Investigation of the Imperial College Plasma (Gabor) Lens Prototype	Dascalu, T.-S. et al.

7. APPENDIX C: SCARF QUEUE USAGE 2020-21

General SCARF Queues

Unsurprisingly, of the non-restricted queues, usage of the scarf queue dominates. The preemptable queue allows users to run across all hardware (including that which is normally restricted) with the caveat that the job may be ended if the nodes are required by a job in another queue that the hardware normally prioritises. The devel queue is intended for short interactive workloads. Uptake of these queues has been slow. It is possible that this is due to them not being publicised enough and that increased awareness of their specific purposes may encourage their use.
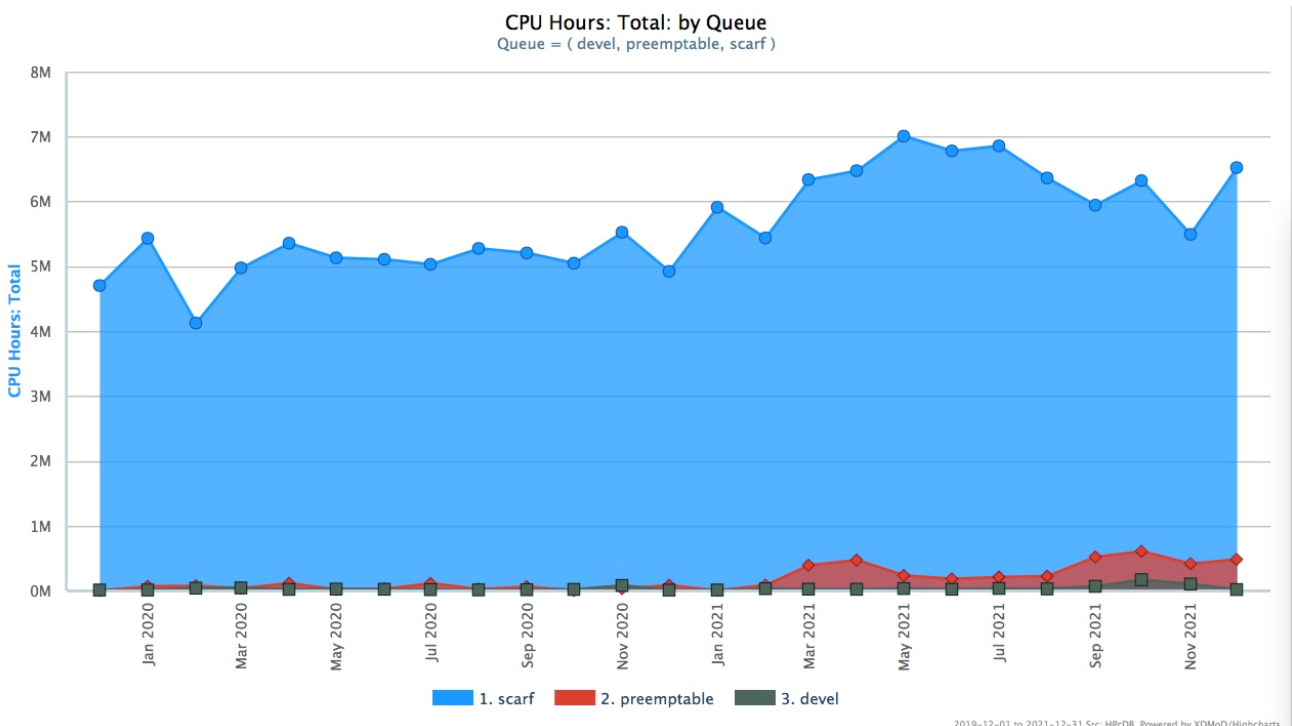
Figure 6: SCARF Queue Usage

MagnaCarta, DeRevolutionibus and Demagnate

These queues are primarily for CLF Plasma Physics use. MagnaCarta has 480 cores purchased in 2016. DeRevolutionibus has 1608 cores purchased in 2017. Demagnate has 384 cores and was purchased in 2019.
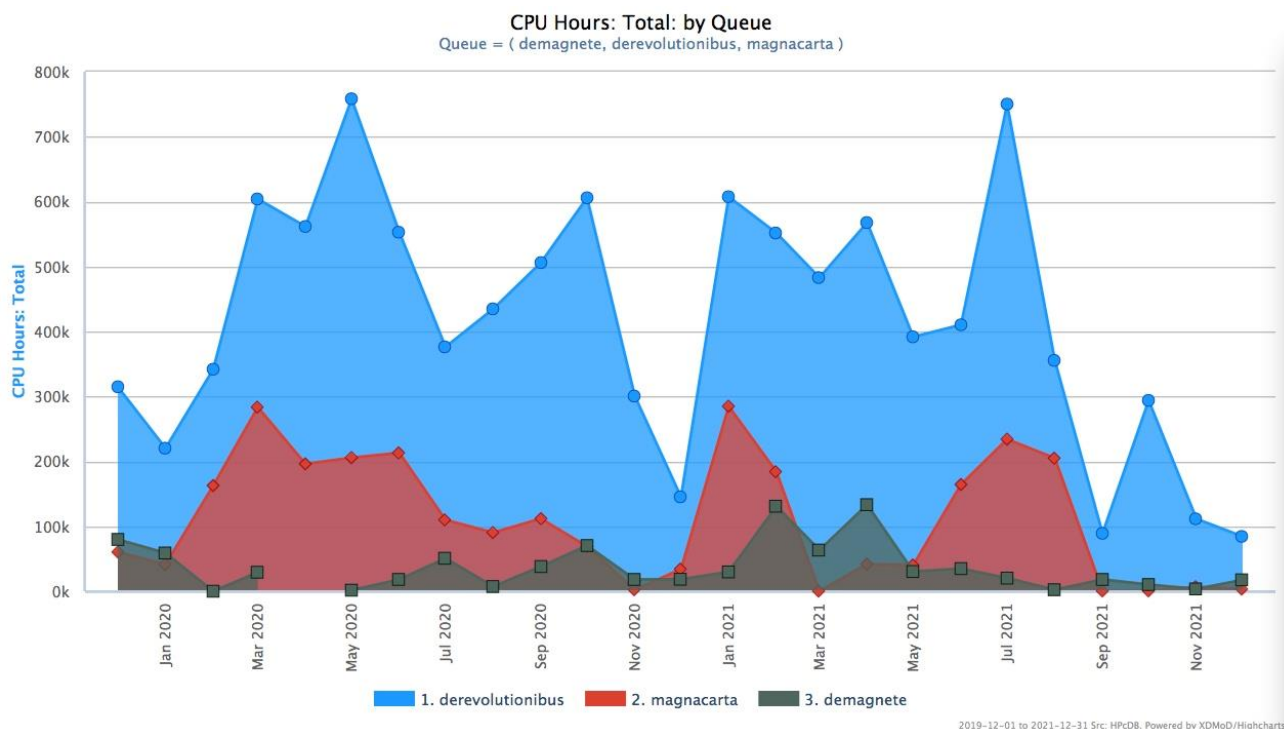
Figure 7: SCARF-MagnaCarta, DeRevolutionibus and Demagnate Usage

DeRevolutionibus continues to be used for higher priority MagnaCarta users and on demand to support CLF experiments. The SCARF-Lexicon-2 queue was retired in August.

SCARF-IBIS

SCARF-IBIS has a capacity of 240 CPU cores and are used for the *Intense Beams in Synchrotrons* collaboration.
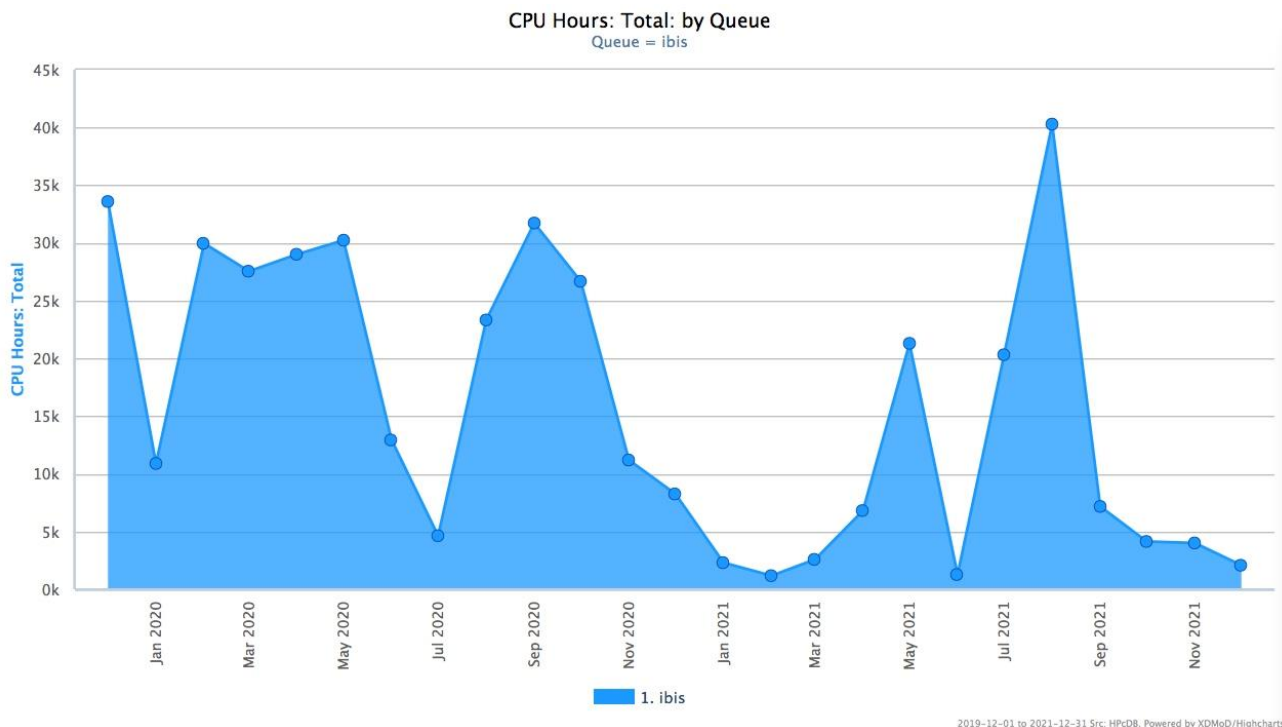
Figure 8: SCARF-IBIS Usage

SCARF Total Power draw

The approximate average power draw of the SCARF cluster for 2020/2021 was 700 amps or 170 kW, excluding the power needed to cool, pump and move cold air.

Filesystem Usage

The plot below outlines the use of the Panasas filespace on the SCARF service. The new storage system has significantly increased capacity.
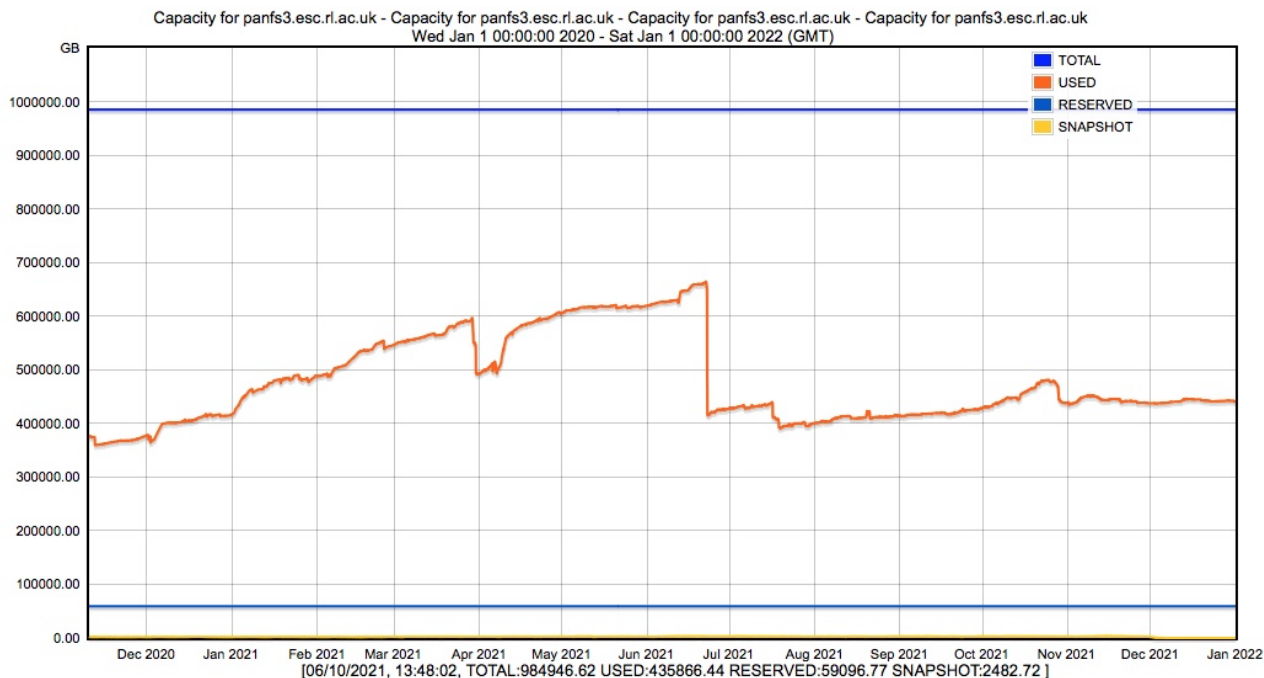
Figure 9: Filespace usage on the Panasas Storage

Networking

The diagram below shows the SCARF compute clusters embedded in the larger Research Infrastructure group's networking infrastructure. The only significant change this year was the removal of the old Panasas storage system (panfs2).

Figure 10: SCARF Network Topology

APPENDIX D: INDEX OF FIGURES